

**ENERGY LEVEL STRUCTURE OF FREE
EXCITONS IN 4H SIC FROM WAVELENGTH
MODULATED ABSORPTION SPECTROSCOPY
AND LOW TEMPERATURE
PHOTOLUMINESCENCE**

by

Walter Klahold

B. S. in Physics, Millersville University, 2011

M. S. in Physics, University of Pittsburgh, 2014

Submitted to the Graduate Faculty of
the Kenneth P. Dietrich School of Arts and Sciences in partial
fulfillment

of the requirements for the degree of

Doctor of Philosophy

University of Pittsburgh

2018

UNIVERSITY OF PITTSBURGH
KENNETH P. DIETRICH SCHOOL OF ARTS AND SCIENCES

This dissertation was presented

by

Walter Klahold

It was defended on

April 5th 2018

and approved by

Wolfgang Choyke, University of Pittsburgh

Robert Devaty, University of Pittsburgh

Vittorio Paolone, University of Pittsburgh

Roger Mong, University of Pittsburgh

Randall Feenstra, Carnegie Mellon University

Dissertation Advisors: Wolfgang Choyke, University of Pittsburgh,

Robert Devaty, University of Pittsburgh

ENERGY LEVEL STRUCTURE OF FREE EXCITONS IN 4H SiC FROM WAVELENGTH MODULATED ABSORPTION SPECTROSCOPY AND LOW TEMPERATURE PHOTOLUMINESCENCE

Walter Klahold, PhD

University of Pittsburgh, 2018

Silicon carbide is a semiconductor material that holds special interest for its use in electronics meant to withstand harsh environments and demanding operating conditions. Its technological importance has been recognized over the course of a relatively long history of research and development, but only recently have growth and production capabilities allowed this material to become a viable platform for industrial electronics. To take advantage of these recent advancements, use is made of high quality 4H SiC boule and epitaxial samples to study the material's photoluminescence and wavelength modulated absorption (WMA) spectra at 2 K or lower in temperature. The main results have been obtained in the WMA measurements, which have been performed in this work at higher resolution than in previous studies. In the wavelength region of interest here ($\sim 3500\text{--}4000 \text{ \AA}$), the dominant absorption and emission processes are characterized by excitation or recombination of free excitons whose electron and hole occupy the valence and conduction band extrema.

Four known features of the WMA spectrum have been found to reproducibly exhibit $0.7\pm 0.1 \text{ meV}$ splittings that have not been resolved previously. These have been observed for samples taken from two independently grown 4 cm diameter boules, and have the spectral profile characteristic of free exciton absorption. The multiplicity of these splittings for polarized illumination of the sample is consistent with a splitting of the free exciton ground state. Several other features which clearly do not have the shape expected for free exciton absorption will be shown to originate from an avoided crossing between the topmost va-

lence bands. A preliminary examination of the WMA spectrum in the range $\sim 3500\text{--}3660 \text{ \AA}$ ($\sim 3.4\text{--}3.6 \text{ eV}$) shows evidence of free exciton absorption processes due either to the exciton's hole occupying a lower-lying valence band (separated from the topmost by the crystal field splitting) or the exciton's electron occupying the second lowest conduction band minimum. The locations of these features in the absorption spectrum are consistent with the calculated positions of these band extrema in the electronic band structure, for which there still remains little experimental evidence even today.

TABLE OF CONTENTS

PREFACE	xii
1.0 LIST OF SYMBOLS AND SHORTHAND	1
2.0 INTRODUCTION	4
3.0 BACKGROUND: THEORY	9
3.1 Effective mass approximation for the exciton	11
3.2 Indirect absorption selection rules	19
3.3 Energy band nonparabolicity	33
3.4 Low temperature photoluminescence	35
4.0 BACKGROUND: EXPERIMENT	42
4.1 Wavelength modulated absorption	42
4.1.1 Basic operating principles	42
4.1.2 Overview of apparatus	45
4.1.3 Double beam configuration	49
4.2 Low temperature photoluminescence	52
4.3 Sample preparation	59
5.0 RESULTS AND DISCUSSION	64
5.1 Data analysis and fitting	64
5.2 Overview of WMA and LTPL measurements	68
5.3 Assignment of free exciton emission lines and absorption onsets	78
5.4 Fine structure splittings of the free exciton band minima	81
5.5 Spectral features due to energy band nonparabolicity	99

5.6 Absorption due to crystal field split-off valence band and second lowest conduction band	108
APPENDIX A. INDIRECT, HYDROGENIC EXCITON WAVEFUNCTION	122
APPENDIX B. VALENCE BAND DENSITY OF STATES	127
APPENDIX C. COUPLING LIGHT INTO A MONOCHROMATOR	135
C.1 Choosing the correct lens material	136
C.2 Optimizing lens dimensions and positioning	138
APPENDIX D. MONOCHROMATOR ALIGNMENT AND CALIBRATION	148
D.1 Considerations for wavelength range of interest	151
D.2 Grating installation and alignment	153
D.3 Calibration	161
BIBLIOGRAPHY	169

LIST OF TABLES

1	Measured and calculated effective masses in 4H SiC conduction and valence band extrema	14
2	Symmetry representations for electron-photon and electron-phonon operators and electronic wavefunctions discussed in the text	22
3	Valence and conduction band extrema occupied by the electron and hole for different classes of exciton	29
4	Exciton bandgap and principal phonon energies from WMA and LTPL measurements in 4H SiC	82
5	Identification of principal phonons measured in this work with calculated symmetries from Serrano <i>et al.</i>	95
6	Measured spin-orbit splittings from wavelength modulated absorption spectra compared with symmetries of associated phonons	96
7	Summary of selection rules for the four lowest lying excitons in 4H SiC	117
8	Assignments of absorption onsets to crystal field split-off exciton in 4H SiC	120
9	Assignments of absorption onsets to the exciton whose electron lies in the second lowest conduction band minimum in 4H SiC	120
10	k-p parameters for modeling top three valence bands in 4H SiC	128

LIST OF FIGURES

1	Hexagonal Brillouin zone with symmetry labels	10
2	Schematic view of the 4H SiC valence and conduction bands nearest to the fundamental gap	13
3	Indirect, hydrogenic exciton energy bands	17
4	Visualization of phonon-assisted electronic transitions to form an indirect exciton	21
5	Energy level splittings in electronic band structure and exciton ground state .	28
6	Energy bands of the four lowest-lying excitons in 4H SiC	30
7	Allowed indirect absorption processes into the fourfold split exciton ground state	32
8	Mirror symmetry of absorption and emission spectra from an indirect exciton	37
9	Simulated temperature dependence of low temperature photoluminescence from several low-lying exciton states	39
10	Experimental setup for wavelength modulated absorption measurements . . .	46
11	Sample holders used for absorption measurements	48
12	Double beam modification of wavelength modulated absorption setup	51
13	Using the double beam configuration to subtract features in a sample's wave- length modulated absorption spectrum that are due to wavelength variations of the incident light intensity	53
14	Experimental setup for low temperature photoluminescence measurements . .	55
15	Sample orientation for taking polarized low temperature photoluminescence measurements	57
16	Measured excitation power dependence of 76.1 meV phonon-assisted free exci- ton emission line	58

17	Induced slant in sample surfaces to reduce the effect of thin film interference .	61
18	Elimination of interference fringes in wavelength modulated absorption measurements by a polishing induced slope over the sample surface	62
19	Function used for fitting to wavelength modulated absorption data	65
20	Example of fit to low temperature wavelength modulated absorption data . .	69
21	Low temperature wavelength modulated absorption measurements in the range 3.30–3.38 eV for $\mathbf{E} \parallel \hat{c}$ in 4H SiC	71
22	Low temperature wavelength modulated absorption measurements of 4H SiC in the range 3.30–3.38 eV for $\mathbf{E} \perp \hat{c}$	72
23	Overview of reference LTPL spectrum of 4H SiC for $\mathbf{E} \parallel \hat{c}$	74
24	Overview of reference LTPL spectrum of 4H SiC for $\mathbf{E} \perp \hat{c}$	75
25	Close-up view of reference 4H SiC LTPL spectrum for $\mathbf{E} \parallel \hat{c}$	76
26	Close-up view of reference 4H SiC LTPL spectrum for $\mathbf{E} \perp \hat{c}$	77
27	Schematic view of the procedure for assigning absorption onsets to phonons and excitons for 4H SiC	80
28	Fine structure splittings in two 4H SiC absorption onsets due to emission of a 40.2 meV principal phonon	84
29	Fine structure splitting in 45.6 meV phonon-assisted absorption onset of spin-orbit split-off exciton in 4H SiC	86
30	Fine structure splitting of the 94.1 meV phonon-assisted absorption onset of the lowest-lying exciton in 4H SiC	87
31	4H SiC LTPL spectrum showing 94.1 and 95.7 phonon-assisted emission lines	88
32	4H SiC absorption onsets due to 40.6 and 41.2 meV principal phonons for both the lowest-lying exciton and the spin-orbit split-off exciton	90
33	4H SiC LTPL measurements of the 40.6 and 41.2 meV phonon-assisted emission lines at two different excitation intensities	91
34	Optically active sub-levels of the two lowest-lying excitons in 4H SiC and their relative separations	93
35	Histogram of spin-orbit splittings measured from wavelength modulated absorption measurements	94

36	Two possible orderings of the sub-levels for the two lowest-lying excitons based on the observed spin-orbit splittings in the absorption spectrum	98
37	Energy versus wavevector plots of the uppermost valence bands in 4H SiC . . .	102
38	Expanded view of Figure 37 showing an avoided crossing between the top two valence bands	103
39	Calculated 4H SiC valence band density of states $N_v(E)$ and its energy derivative dN_v/dE	105
40	Comparison between wavelength modulated absorption in 4H SiC with the energy derivative of the valence band density of states	106
41	Overview of wavelength modulated absorption measurements in 4H SiC covering the range 3.3–3.6 eV for $\mathbf{E} \parallel \hat{c}$	110
42	Overview of wavelength modulated absorption measurements in 4H SiC covering the range 3.3–3.6 eV for $\mathbf{E} \perp \hat{c}$	111
43	Overlapping arrangement of pairs of exciton energy bands which produces spectral broadening	113
44	Detailed view of the $\mathbf{E} \parallel \hat{c}$ polarized absorption spectrum in the range 3.38–3.5 eV	114
45	Detailed view of the $\mathbf{E} \perp \hat{c}$ polarized absorption spectrum in the range 3.38–3.5 eV	115
46	Assignments made to several features in the absorption spectrum associated with the crystal field splitting and second lowest conduction band minimum in 4H SiC	119
47	Contour plots of the Fourier coefficients of the hydrogenic exciton’s envelope function for 4H SiC	124
48	Division of a cubic volume of k-space into tetrahedra for the purpose of numerical integration	133
49	Optical setup for coupling light from a source into the entrance slit of a monochromator	137
50	Refractive index of borosilicate glass	138
51	Transmittance for a 10 mm thick plate of borosilicate glass	139

52	Refractive index of UV-grade fused silica	139
53	Relevant quantities for calculating the radiant flux emitted by a two-dimensional object	141
54	Light scattering inside a monochromator due to improper f-number matching	144
55	Radiant flux coupled into a monochromator versus the magnification of the auxiliary lens system	147
56	Overview of internal optical components of a SPEX 1401 double monochromator	150
57	Adjustment screw for translating the pair of concave mirrors in either half of the SPEX 1401	152
58	Mounting and locking mechanism for the diffraction gratings inside the SPEX 1401	154
59	Grating mounting plate marked with locking and adjustment screw positions	156
60	A blazed groove profile on a diffraction grating and its effect on the intensity of the various diffraction orders	157
61	Gearing system on the underside of the SPEX 1401 for rotating the diffraction gratings	159
62	Beam deflection about the exit slit during wavelength modulation for proper and improper intermediate slit settings	162
63	Overview of cosecant drive system for rotating the diffraction gratings in the SPEX 1401	164
64	Comparison of two different fits to wavelength calibration data for the SPEX 1401	167

PREFACE

Thank you Mom and Dad for instilling in me a sense of fascination and wonder for the world around me. It has helped me immeasurably through good times and bad, and I don't intend to ever let it go. Thanks to all of my family and friends, and to the Pitt staff and community for their genuine interest and support in my studies. Thank you Blue Sky. Thank you Watchdog for looking out for me during my long walks home under the dim, yellow sodium lamps. Thank you Dr. Devaty for your mentorship and insightful conversations. Your mind is a light, and I am indebted to you for sharing in its glow. Lastly, thank you Dr. Choyke for your guidance, your wit, and your limitless enthusiasm. There is surely a fire in you that cannot fade or be forgotten.

1.0 LIST OF SYMBOLS AND SHORTHAND

WMA	Wavelength modulated absorption
LTPL	Low temperature photoluminescence
VBM	Valence band maximum
CBM	Conduction band minimum
\mathbf{K}_v	Wavevector at the valence band maximum
\mathbf{K}_c	Wavevector at the conduction band minimum
Γ	Position in the Brillouin zone of the three highest valence band maxima in 4H SiC
Γ_i	Symmetry representation of the C_{6v} point group associated with the Γ point in the Brillouin zone ($i = 1 \dots 9$)
M	Position in the Brillouin zone of the two lowest conduction band minima in 4H SiC
M_i	Symmetry representation of the C_{2v} point group associated with the M point in the Brillouin zone ($i = 1 \dots 5$)
E_g	Energy separation between the topmost valence band maximum and the lowest conduction band minimum. Also called the fundamental bandgap.
Δ_{so}	Energy separation between the topmost valence band maximum and the second highest valence band maximum. Also called the spin-orbit splitting of the valence bands.

Δ_{cf}	Energy separation between the topmost valence band maximum and the third highest valence band maximum. Also called the crystal field splitting of the valence bands.
Δ_{12}	Energy separation between the lowest conduction band minimum and the second lowest conduction band minimum
EX ₁	Exciton whose electron occupies the lowest conduction band minimum and whose hole occupies the topmost valence band maximum
EX _{so}	Exciton whose electron occupies the lowest conduction band minimum and whose hole occupies the second highest valence band maximum
EX _{cf}	Exciton whose electron occupies the lowest conduction band minimum and whose hole occupies the third highest valence band maximum
EX ₂	Exciton whose electron occupies the second lowest conduction band minimum and whose hole occupies the topmost valence band maximum
I _x	Emission line due to free exciton recombination assisted by a phonon with energy x in meV
P _x	Emission line from P-series of nitrogen bound exciton recombination assisted by a phonon with energy x in meV
P _o	No-phonon line from P-series of nitrogen bound exciton recombination
$\hbar\omega^{(e)}$	Photon energy corresponding to a general free exciton emission line
$\hbar\omega^{(a)}$	Photon energy corresponding to a general free exciton absorption onset

K	Wavevector of the exciton center of mass
E_x	Binding energy of a free exciton
E_{Dx}	Binding energy of a bound exciton to a defect
E_{gx}	Exciton bandgap. Taken to mean the minimum energy available to an exciton.
$E_{gx}^{(i)}$	Same as directly above, but with the class of exciton $i = 1, so, cf, 2$ now specified
$E_{gx}^{(i,j)}$	Same as directly above, but with the particular exciton sub-band $j = 1, 2, 3, 4$ now specified
$\delta_{j,k}^{(i)}$	Energy separation between the exciton sub-band minima $E_{gx}^{(i,j)}$ and $E_{gx}^{(i,k)}$ for a single exciton of class $i = 1, so, cf, 2$
$\Delta_{so}^{\prime(j)}$	Energy separation between the j th sub-band minimum of exciton EX ₁ and the j th sub-band minimum of exciton EX _{so}
α	Absorption coefficient
x	Sample thickness parallel to transmitted light
E	Electric field of incident light
\hat{c}	Stacking axis of silicon-carbon bi-layers

2.0 INTRODUCTION

While silicon carbide is by no means a newcomer in the history of semiconductor technology (electroluminescence was first observed in silicon carbide in 1907 [1] and the first LED was made from silicon carbide in 1923 [2]), its development as a platform for electronic devices has been prolonged for decades by an array of technical challenges relating to crystal growth. Much of the early, foundational research on silicon carbide was performed on relatively small, irregularly shaped crystals produced by the Lely method of sublimation growth [3]. Although this was adequate at the time for research purposes, a great deal of progress has been made since then not only in terms of crystal growth but also in terms of the accuracy and sophistication of first principles calculations to which experiments may be compared.

This work began with the intent to take advantage of these advancements while revisiting some of the earlier measurements of the fundamental electronic properties of silicon carbide, with an emphasis placed on the 4H polytype. While 4H SiC is currently the most technologically important polytype, other common silicon carbide polytypes include cubic 3C SiC, rhombohedral 15R SiC, and hexagonal 6H SiC, and each of these differs from one another in their crystal structure and the number of Si–C bi-layers contained in their unit cells. These other polytypes will be mentioned only in passing in the text, whereas all of the measurements to be presented here are of 4H SiC. A particular emphasis is placed on its intrinsic optical properties at low temperature, i.e. those properties arising from the electronic energy band structure of the crystal when it is free of defects (namely: impurities, lattice imperfections, and surfaces). The wavelength regions under study in this work have been both expanded in size and measured at higher wavelength resolution than in previous attempts, revealing a number of reproducible features in the obtained spectra that have not been reported elsewhere. An attempt has been made to connect each of these features to

the underlying electronic properties of the material.

A standard technique in optical spectroscopy that is employed here and elsewhere in semiconductors is the measurement of low temperature photoluminescence (LTPL), where a pulsed or continuous light source is used to excite the crystal and the photoluminescence resulting from its various radiative relaxation processes is spectrally analyzed. In silicon carbide, LTPL is often dominated by the recombination radiation of the electron-hole pairs produced in the excitation and bound together by their Coulomb attraction to form excitons. However, it is also common that, before recombination, the exciton itself becomes bound to a defect, which in silicon carbide is most often nitrogen. The photoluminescence spectrum from these bound excitons strongly overlaps the spectrum due to free excitons. In Section 3 it will be shown that the indirect nature of the fundamental band gap in silicon carbide requires that both types of excitons recombine with an accompanying momentum transfer from a phonon or a defect, resulting in a sizable number of phonon “replicas” in the LTPL spectrum (along with a single “no-phonon” line in the case of the bound exciton). The relative spacings of these replicas for the free and bound excitons are similar, but differ from one another in subtle ways that will be shown later on. For this reason a sample of high enough purity (nitrogen concentration $\sim 10^{-13} \text{ cm}^{-3}$) was used in these measurements so that the bound exciton LTPL did not obscure the free exciton LTPL, which is the more central interest to this work.

A second approach taken here is the use of wavelength modulated absorption (WMA) spectroscopy, which constitutes the majority of this work. As will be described in the Section 4.1, the WMA measurement consists of measuring the intensity of the light transmitted through the sample as a function of the incident light’s wavelength, which is modulated sinusoidally over a small range in order to enhance the resulting spectral features. In some sense it is the inverse of the LTPL measurement: rather than analyze the light emitted in the process of relaxation, the light that is absorbed by the crystal in the process of excitation is analyzed. In fact the same phonons which produce the replicas in LTPL may be shown to participate in each of the absorption processes observed in the WMA spectrum, and so the two measurements can be used in tandem to assist in the identification of unknown spectral features.

Despite the apparent symmetry, the use of WMA spectroscopy does afford certain advantages over the measurement of LTPL. Perhaps the greatest of these is the possibility in WMA spectroscopy of observing optical transitions into excited states of the exciton. In LTPL the excitons have at least to some extent thermalized with the surrounding lattice before emitting photoluminescence, so that relaxation from the exciton ground state is energetically favored in the resulting spectrum and excited states higher than a few kT are virtually unobserved (in all of the experiments discussed in this work the samples are maintained at or below 2 K, so $kT < 0.2$ meV). Elevating the sample temperature will mainly serve to broaden the exciton emission spectrum, so that closely spaced features may become difficult to resolve. Since the bound exciton lies lower energetically compared to the free exciton, this may also explain the prominence of bound exciton emission in LTPL spectra despite the host atoms far outnumbering the impurities. It should be noted that although absorption processes associated with bound excitons are apparent in the WMA spectrum of fairly impure samples, all of the WMA measurements presented here on relatively pure silicon carbide are believed to be dominated by features due to the formation of free excitons, and thus are intrinsic to the bulk material.

Evidence for excited states of the free exciton has already been encountered in several previous WMA measurements in 4H SiC, among other polytypes [4, 5, 6, 7, 8, 9, 10]. The excited states discussed in these works are those in which the exciton's hole occupies a valence band that is split off from the topmost (due to spin-orbit interaction or uniaxial crystal field in non-cubic polytypes [11, 12, 13, 14, 15]), whereas in the ground state the hole occupies the topmost valence band (in other words, excitation of an electron from the topmost valence band requires the least amount of energy). Similarly, it is also possible in principle to form an exciton whose electron occupies a conduction band higher than the lowest. Some experimental evidence exists for this in the case of 4H SiC [16, 17, 18]. Evidence for all of these exciton excited states exists in the WMA measurements presented here, although some manifest themselves more convincingly than others. It is apparent that those features due to the higher excited states suffer a considerable amount of spectral broadening, which complicates their identification.

The two lowest lying states of the free exciton figure into the WMA spectrum as several

pairs of similarly-shaped features separated roughly by the spin-orbit splitting of the valence band. Both bear a strong resemblance to the asymmetric, inverse square root dependence on the incident photon energy as predicted in the seminal work by Elliott [19], but exhibiting a departure towards the high energy tail. It will be shown that this is likely due to an avoided crossing between the top two valence bands that appears in band structure calculations [13, 14, 20, 15] for 4H SiC. An additional avoided crossing appears between the second and third highest valence bands [13, 14, 20, 15], although its influence on the WMA spectrum is not nearly as apparent.

A further departure from the simple model given by Elliott is the appearance of several small 0.7 ± 0.1 meV splittings in several places in the WMA spectrum and only for light polarized perpendicular to the sample's bi-layer stacking axis (electric field $\mathbf{E} \perp \hat{c}$). Samples were sectioned from two independent, 4 cm diameter ingots, and it was found that these splittings reproduced in the spectra obtained from both sets of samples. In Section 3.2 this will be shown to be consistent with a group theory analysis which predicts a fourfold splitting for both the free exciton ground state and its spin-orbit split-off counterpart, with two of the four sub-levels being optically active for $\mathbf{E} \perp \hat{c}$ and only one for $\mathbf{E} \parallel \hat{c}$. Further support for this argument is found in the free exciton LTPL, for which *no* such splittings are observed. As discussed earlier, this is to be expected for a well-thermalized exciton, for which the higher of the two optically active ground state sub-levels would be suppressed by the Boltzmann factor.

The first of the following sections in this thesis covers the theoretical background needed to interpret the major features in both the WMA and LTPL spectra presented in this work. Emphasis will be placed on those energy bands nearest to the fundamental gap which are most relevant to the lowest energy excitation and emission processes by free excitons. A simplified introduction to the properties of free excitons will be given that follows closely with that given by Elliott [19] and Dresselhaus [21], although an attempt will be made to go beyond this model to account for some of the observations mentioned above, at least qualitatively. An overview of the structural and vibrational properties of 4H SiC will also be given in view of their importance to the optical spectra. Following this will be a section covering the experimental details of the WMA and LTPL measurements, including some of

the technical aspects of sample preparation and equipment modification used to expand the scope and sensitivity of this work. The results from these measurements will be presented in the closing section with comparison to the theory given here and to previous measurements by others.

3.0 BACKGROUND: THEORY

In an ideal solid at zero temperature the electrons distribute themselves among the lowest energy Bloch states $\psi_{n\mathbf{k}}$, with each of these corresponding to a particular energy band $E_n(\mathbf{k})$ and wavevector \mathbf{k} . By the usual convention, \mathbf{k} is limited by Born-von Karman boundary conditions to within the first Brillouin zone (the hexagonal Brillouin zone appropriate to 4H SiC is shown in Figure 1 along with several high symmetry points and axes). For a semiconductor such as silicon carbide, a gap E_g of forbidden energies separates a group of the lowest lying energy bands (valence bands) from the empty (conduction) bands which are higher in energy. In this situation the minimum energy electronic excitations are those for which an electron is promoted from the top of the valence bands to the bottom of the conduction bands, leaving a hole remaining in the valence band. Because of the Coulomb attraction between the electron and hole, the two must be treated as a kind of quasi-particle called an exciton. The exciton energy level structure, which is closely related to the underlying electronic band structure, will be shown to have a significant influence on the low temperature optical absorption and emission spectra discussed in this work. In the calculation that follows, this energy level structure is found after much simplification to closely resemble that of a hydrogen atom. While this model is adequate to explain many of the salient features in the optical spectra presented in this work, it will be necessary to undo some of these simplifications in order to account for some of the finer details.

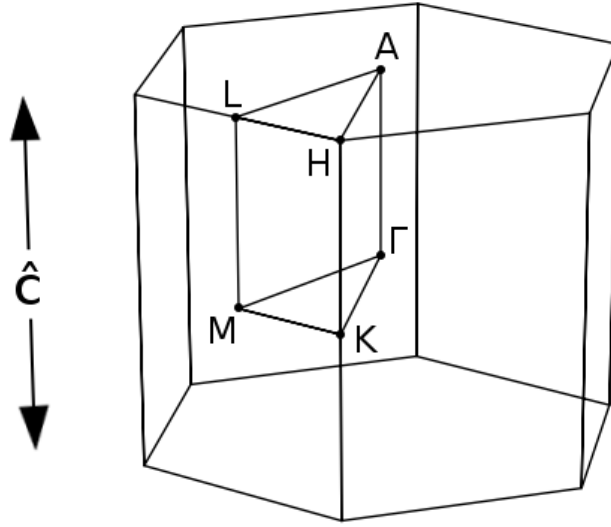


Figure 1: Hexagonal Brillouin zone within which the energy bands $E_n(\mathbf{k})$ of 4H SiC may be plotted versus wavevector \mathbf{k} . All labels refer to points of high symmetry with respect to the rotations and reflections which leave the crystal unchanged. In particular, the origin $\mathbf{k} = \mathbf{0}$ lies at the Γ point. In 4H SiC the top three valence band maxima are located at this point, whereas the two lowest conduction band minima are located at the point M. The high symmetry axis Γ -A is aligned with the Si-C bi-layer stacking axis \hat{c} .

3.1 EFFECTIVE MASS APPROXIMATION FOR THE EXCITON

The method of attack here will be the effective mass approximation (EMA), which was originally developed for studying weak perturbations to single electrons and holes in solids [22, 23, 24] but later extended to the case of excitons [25, 19, 21]. The usual criterion for the validity of the effective mass approximation is that the perturbing potential V varies slowly compared to the size of the unit cell in the solid, so that its Fourier components $V_{\mathbf{K}}$ are limited to a small range in the Brillouin zone. In the context of the exciton problem $V = -e^2/\epsilon r$, where e is the electron charge and r is the electron-hole separation. The screening of the electron-hole attraction is accounted for by the static dielectric constant ϵ , and so it is expected that the EMA should hold in those materials for which ϵ is large. Because 4H SiC has a uniaxial crystal structure, ϵ is anisotropic with respect to the stacking axis (\hat{c}) of Si-C bilayers. To date these values have not been reported for 4H SiC, but they are believed to be of similar magnitude to those of 6H SiC: $\epsilon_{\perp} = 9.66$, $\epsilon_{\parallel} = 10.03$ [26]. We will ignore this anisotropy for the time being, and later verify whether or not the screening is effective in this case.

Taking the EMA to be applicable in this case, we follow the treatment given by Elliott and Dresselhaus in searching for an exciton wavefunction of the form [19, 21]:

$$\Psi_{Ex}(\mathbf{r}_e, \mathbf{r}_h) = \sum_{\mathbf{k}_e, \mathbf{k}_h} C_{\mathbf{k}_e, \mathbf{k}_h} \psi_{c, \mathbf{k}_e}(\mathbf{r}_e) \psi_{v, \mathbf{k}_h}(\mathbf{r}_h), \quad (3.1)$$

where $\psi_{c, \mathbf{k}_e}(\mathbf{r}_e) = e^{i\mathbf{k}_e \cdot \mathbf{r}_e} u_{c, \mathbf{k}_e}(\mathbf{r}_e)$ and $\psi_{v, \mathbf{k}_h}(\mathbf{r}_h) = e^{i\mathbf{k}_h \cdot \mathbf{r}_h} u_{v, \mathbf{k}_h}(\mathbf{r}_h)$ are the Bloch functions for the electron and hole in the lowest conduction band and highest valence band, respectively. If the weak binding limit is valid, the sum should be composed mostly of electron states with \mathbf{k}_e at or near the wavevector of the conduction band minimum (CBM) \mathbf{K}_c and hole states with $-\mathbf{k}_h$ at or near the wavevector of the valence band maximum (VBM) \mathbf{K}_v (recall that a hole has a wavevector opposite that of a missing electron). In semiconductors like silicon carbide, the wavevectors \mathbf{K}_c and \mathbf{K}_v are not the same. For example, while the valence band maximum is believed to be at the point Γ ($\mathbf{k} = \mathbf{0}$) for all polytypes, the current consensus places the conduction band minimum at the M point for 4H SiC (see Figure 1 for the naming conventions for high symmetry points in the Brillouin zone) [6, 27, 28, 11, 12, 13, 14, 15]. The energy gap

in these cases is called *indirect*, and this property will be seen to have a significant effect on the absorption and emission spectrum. There are generally several different conduction and valence bands that make up the electronic band structure in 4H SiC, each with their own set of extrema (see Figure 2 for a schematic diagram of the band structure in 4H SiC). Excitons formed from Bloch functions associated with these other energy bands and extrema will be discussed later, but for now we focus on the *lowest* conduction band and the *highest* valence band.

The Schrödinger equation for the exciton can now be recast in terms of the Fourier transform $\Phi(\mathbf{r}_e, \mathbf{r}_h)$ of the coefficients $C_{\mathbf{k}_e, \mathbf{k}_h}$:

$$\left[E_g + \frac{1}{2} \Delta \mathbf{p}_e^\top \mathbf{D}_c \Delta \mathbf{p}_e + \frac{1}{2} \Delta \mathbf{p}_h^\top \mathbf{D}_v \Delta \mathbf{p}_h - \frac{e^2}{\epsilon r} - E \right] \Phi = 0, \quad (3.2)$$

where $\Delta \mathbf{p}_e = \mathbf{p}_e - \hbar \mathbf{K}_c$, $\Delta \mathbf{p}_h = \mathbf{p}_h + \hbar \mathbf{K}_v$, $\mathbf{r} = \mathbf{r}_e - \mathbf{r}_h$, and the matrices \mathbf{D}_c and \mathbf{D}_v are inverse effective mass tensors describing the curvature of the conduction and valence bands at their respective extrema:

$$D_{\alpha\beta} = \pm \frac{1}{\hbar^2} \frac{\partial^2 E(\mathbf{k})}{\partial k_\alpha \partial k_\beta} \Big|_{\mathbf{k}=\mathbf{k}_o} \quad (3.3)$$

To ensure that the electron and hole masses are both positive for all components, the upper sign here is used for the conduction band and the lower sign is used for the valence band. The form of \mathbf{D} is connected to the group of the wavevector at the given band extremum [29, 30, 31, 32, 33], which are those symmetry operations for the solid (namely, rotations and reflections) that leave the wavevector unchanged. For crystals of high enough symmetry, it could be the case that \mathbf{D} is diagonal with all entries equal to, say, $(1/m^*)$. The expansion of $E(\mathbf{k})$ about the extremum \mathbf{k}_o then contains the form $\hbar^2(\mathbf{k} - \mathbf{k}_o)^2/2m^*$, and the resulting constant energy surfaces are spheres centered at \mathbf{k}_o . In crystals of relatively low symmetry such as 4H SiC, the effective mass tensors corresponding to different band extrema will in general have off diagonal components and the resulting energy surfaces are ellipsoidal. In such a case \mathbf{D} may be diagonalized to give the components $1/m_1, 1/m_2, 1/m_3$ along the ellipsoid's principle axes. These components are to some extent known for the CBM and VBM in 4H SiC from cyclotron resonance experiments. They are shown in Table 1 along with their corresponding values determined from band structure calculations.

For the time being we will assume the electron and hole have isotropic effective masses

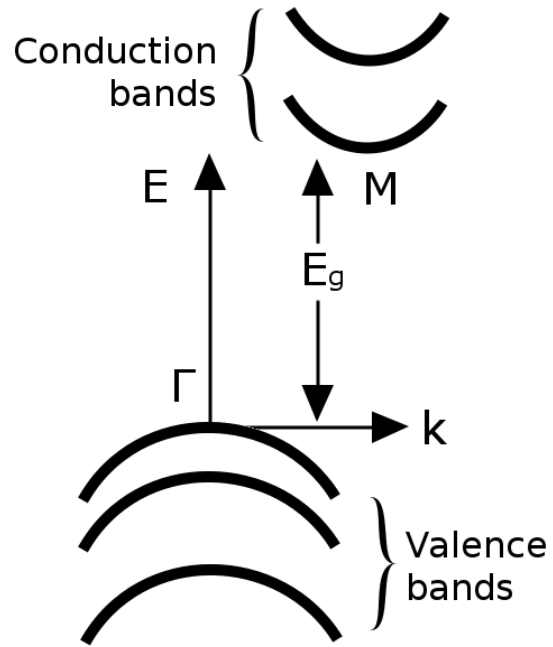


Figure 2: Schematic view of the 4H SiC valence and conduction bands nearest to the fundamental gap. The top three valence bands have their maximum at the Γ point in the Brillouin zone and the bottom two conduction bands have their minimum at the M point.

Table 1: Measured and calculated effective masses along specified axes at the valence band maximum (VBM) and conduction band minimum (CBM) for 4H SiC. All values are specified in units of free electron mass m_0 . For the CBM $m_{\perp} = \sqrt{m_{M\Gamma}m_{MK}}$ and for the VBM $m_{\perp} = \sqrt{m_{\Gamma M}m_{\Gamma K}}$. The two left-most values in either column of calculated values are from two separate calculation methods from reference [14] while the third value is taken from reference [12].

4H SiC		
	Experiment	Theory
CBM:		
m_{ML}	0.29, 0.33	0.31, 0.34, 0.31
$m_{M\Gamma}$	0.58	0.57, 0.59, 0.58
m_{MK}	0.31	0.28, 0.31, 0.28
m_{\perp}	0.42, 0.32	0.40, 0.43, 0.40
Refs.	[34, 35]	[14, 12]
VBM:		
$m_{\Gamma A}$	1.75	1.56, 1.60, 1.55
m_{\perp}	0.66	0.59, 0.59, 0.62
Refs.	[36]	[14, 12]

m_e and m_h but with the intension of adding the anisotropy back in later. At this point it is important to take stock of what other approximations have been made aside from this one. The two terms that are bilinear in the electron and hole momenta arise from expansions about the two band extrema to second order in the wavevector \mathbf{k} , followed by replacement with the corresponding momentum operators \mathbf{p}_e and \mathbf{p}_h . This implies the valence and conduction band extrema are parabolic, which is very clearly not so in the band structure calculations for 4H SiC (see Figures 37 and 38 in section 5.5). A second assumption that has been made is that the overall exciton wavefunction consists of Bloch functions from only one pair of bands, namely the highest valence band and the lowest conduction band (see (3.1)). It will be seen that excitons arising from different pairs of bands do indeed manifest in the WMA measurements presented here, but it assumed in all cases that each one is still only made up of Bloch functions from a single valence-conduction band pair.

With these various approximations in place, we have for (3.2):

$$\left[E_g + \frac{1}{2m_e} \left(\frac{m_e}{M} \hbar \mathbf{K} + \mathbf{p} - \hbar \mathbf{K}_c \right)^2 + \frac{1}{2m_h} \left(\frac{m_h}{M} \hbar \mathbf{K} - \mathbf{p} + \hbar \mathbf{K}_v \right)^2 - \frac{e^2}{\epsilon r} - E \right] \phi'(\mathbf{r}) = 0 \quad (3.4)$$

In the above we have used the separation of variables:

$$\Phi = e^{i\mathbf{K}\cdot\mathbf{R}} \phi'(\mathbf{r}), \quad (3.5)$$

with $\mathbf{R} = (m_e \mathbf{r}_e + m_h \mathbf{r}_h)/(m_e + m_h)$ being the exciton center of mass. We also have $M = m_e + m_h$ and $\mathbf{p} = (m_h \mathbf{p}_e - m_e \mathbf{p}_h)/M$, which is the momentum conjugate to the relative coordinate \mathbf{r} . Equation (3.4) can be further simplified with the substitution:

$$\phi'(\mathbf{r}) = e^{i(m_h \mathbf{K}_c + m_e \mathbf{K}_h)\cdot\mathbf{r}/M} \phi(\mathbf{r}) \quad (3.6)$$

(This reduces to Dresselhaus' equation (22) for $m_e = m_h$ [21]). We then have:

$$\left[E_g + \frac{\hbar^2(\mathbf{K} - \mathbf{K}_c + \mathbf{K}_v)^2}{2M} + \frac{\hbar^2 p^2}{2\mu} - \frac{e^2}{\epsilon r} - E \right] \phi(\mathbf{r}) = 0, \quad (3.7)$$

where $\mu = m_e m_h / M$ is the reduced mass of the exciton. Equation (3.7) is nearly identical to the Schrödinger equation for the hydrogen atom, and it has the solutions [19, 21]:

$$E_n(\mathbf{K}) = E_g + \frac{\hbar^2(\mathbf{K} - \mathbf{K}_c + \mathbf{K}_v)^2}{2M} - \frac{E_x}{n^2}. \quad (3.8)$$

The third term has the form of a Rydberg series with $n = 1, 2, 3 \dots$ and binding energy (in Gaussian units) [21]

$$E_x = \frac{\mu e^4}{2\hbar^2 \varepsilon^2}. \quad (3.9)$$

Making a rough guess for the reduced mass μ appearing in the binding energy, we can use $m_e = (m_{ML}m_{M\Gamma}m_{MK})^{1/3}$ and $m_h = (m_{\Gamma A}m_{\perp}^2)^{1/3}$. Taking some reasonable values from Table 1 gives $\mu = 0.3m_o$ (m_o is the free electron mass), and by combining this with $\varepsilon \approx 10$ we obtain $E_x \approx 40$ meV. The effective Bohr radius (also in Gaussian units) [19]

$$a_x = \frac{\hbar^2 \varepsilon}{\mu e^2} \quad (3.10)$$

is found to be 20 Å. By comparing this radius to the lattice parameters [37] $a = 3.079$ Å and $c = 10.254$ Å it would seem the electron-hole attraction falls in the regime of weak to intermediate strength. A more careful assessment of this question is given in Appendix A.

The second term in (3.8) gives the kinetic energy associated with the exciton center of mass, whose corresponding momentum is given by $\hbar\mathbf{K}$. To each hydrogenic state n thus corresponds a distinct band, each of which has a minimum at $\mathbf{K}_o = \mathbf{K}_c - \mathbf{K}_v$ and is both parabolic and isotropic about that minimum (see Figure 3). For 4H SiC we have $\mathbf{K}_v = \mathbf{0}$ and $\mathbf{K}_o = \mathbf{K}_c$, and so the exciton bands are centered about the same point in the Brillouin zone as the CBM (this will be assumed hereafter for simplicity). It is evident from (3.8) that the energy required to create an exciton in its ground state $E_1(\mathbf{K}_c)$ is not the energy gap E_g but $E_{gx} = E_g - E_x$ (the *exciton bandgap*). Furthermore, a certain amount of momentum (namely, $\hbar\mathbf{K}_c$) must also be transferred. Because a photon alone imparts negligible momentum, a second order process involving both a photon and a phonon is needed in order for transitions to be made (hence the term indirect gap).

At the low temperatures for which all measurements in this work were performed, virtually no phonons are present to transfer momentum, and so all indirect absorption and emission processes considered here will be those for which a phonon is created. In this case, the total energy imparted to the exciton is given by $\Delta E = \hbar\omega - \hbar\Omega$, where $\hbar\omega$ and $\hbar\Omega$ are the energies of the photon and phonon, respectively. For those photon energies for which $\Delta E < E_{gx}$, no excitation occurs and the crystal is transparent. As the photon energy is increased further it eventually reaches the threshold $\hbar\omega = E_{gx} + \hbar\Omega$, at which

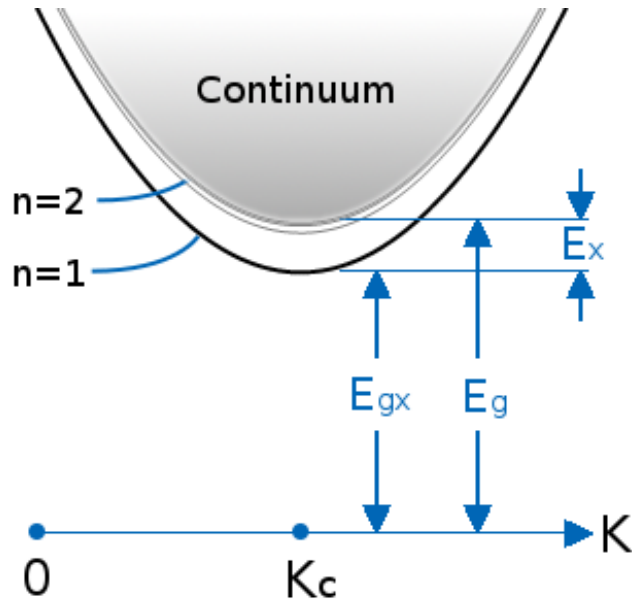


Figure 3: Energy bands of an indirect, hydrogenic exciton plotted versus the exciton center of mass wavevector \mathbf{K} . Each band $E_n(\mathbf{K})$ corresponds to a specific hydrogen-like orbital shell of the electron about the hole, which is indexed by n . All are parabolic and isotropic in the displacement $\mathbf{K} - \mathbf{K}_c$, where \mathbf{K}_c is the wavevector corresponding to the conduction band minimum (assuming the valence band maximum is at the Brillouin zone center). The minimum of each band lies at $\mathbf{K} = \mathbf{K}_c$ where the exciton energy is given by a Rydberg-like series $E_n(\mathbf{K}_c) = E_g - E_x/n^2$, where E_g is the fundamental band gap for the material in question and E_x is the exciton binding energy. This series of bands corresponds to bound states for the electron-hole system, and lying above them is a continuum of energy states corresponding to free electron-hole pairs. The *exciton bandgap* here is given by $E_{gx} = E_g - E_x$.

point an exciton is formed and the crystal begins to grow opaque. As $\hbar\omega$ is increased higher still, excitons with \mathbf{K} away from \mathbf{K}_c may similarly be created, so that a step-like onset in absorption is observed. The absorption is quantified by the absorption coefficient α , which describes the attenuation of a beam of light as it passes through the solid [38]:

$$I = \left[\frac{(1-R)^2}{1-R^2e^{-2\alpha x}} \right] I_o e^{-\alpha x} \approx (1-R)^2 I_o e^{-\alpha x}, \quad (3.11)$$

where I and I_o are the transmitted and incident light intensities, respectively, R is the reflectivity of the material, and x is the thickness of the material. Thin film interference has been neglected (although it will be seen to be significant for some cases in this work), and the approximation step neglects multiple reflections. The calculation of α for the simple hydrogenic model for the exciton has been performed by Elliott [19], with the result being:

$$\alpha \propto (2M/\hbar^2)^{3/2} \left| \frac{\partial\phi_n}{\partial r}(r=0) \right|^2 \sqrt{\hbar\omega - E_{gx}/n^2 - \hbar\Omega}. \quad (3.12)$$

ϕ_n here is just the hydrogenic orbital found as the solution to (3.7) ((3.12) corresponds to Elliott's expression (4.9)). This has the form of a series of absorption onsets—one for each shell n —occurring at the photon energies $\hbar\omega_n = E_{gx}/n^2 + \hbar\Omega$. The factor involving $|\partial\phi_n/\partial r|^2$ evaluated at $r=0$ suggests that only S-like hydrogenic states contribute to absorption (since all other hydrogenic envelopes have nodes at $r=0$). While this factor decreases rapidly as $1/n^3$ [19], excitons with $n > 1$ have been reported in the optical spectra of other indirect gap semiconductors [39, 40, 41, 42]. Using the rough approximation for the exciton binding energy $E_x \approx 40$ meV found earlier, an $n=2$ exciton absorption threshold should lie higher in energy than the $n=1$ threshold by $3E_x/4 \approx 30$ meV. However, since no strong evidence for these exist in the measurements to be shown here, we will confine attention to the $n=1$ excitons from here onward.

Above the Rydberg-like series of bound states exists an energy continuum corresponding to dissociated electron-hole pairs. As the photon energy is increased far enough beyond the initial threshold such that these states are excited, the dependence given in (3.12) transitions to [19]:

$$\alpha \propto (2\sqrt{m_e m_h}/\hbar^2)^3 (\hbar\omega - E_g - \hbar\Omega)^2. \quad (3.13)$$

(This is Elliott’s equation (4.15) in which he denotes the absorption coefficient by κ). The transition between the dependence given in (3.12) and that shown in (3.13) has been used to estimate the exciton binding energy in other materials (see [43], for example), but a determination such as this is particularly complicated for the case of 4H SiC, and so has not been attempted here.

One of the foremost of these complications has to do with the fact that there are a relatively large number of phonons that may participate in the indirect absorption onsets described by (3.12). By momentum conservation each one must have the momentum $\hbar\mathbf{q} = \hbar\mathbf{K}_c$ necessary to create an exciton in its ground state at $\mathbf{K} = \mathbf{K}_c$. Phonons which meet this condition are referred to as the *principal phonons* and in 4H SiC there are 24 of them. Each of these has a distinct energy $\hbar\Omega_i$ and therefore gives rise to a distinct absorption onset at $\hbar\omega_i^{(a)} = E_{gx} + \hbar\Omega_i$. In order to measure the exciton bandgap energy E_{gx} it is therefore necessary to know each of the principle phonon energies. By a similar argument as above, these same phonons produce peaks in the exciton’s low temperature *emission* spectrum at the photon energies $\hbar\omega_i^{(e)} = E_{gx} - \hbar\Omega_i$, and so one may use this symmetry about E_{gx} to cross-reference the absorption onsets with the emission peaks appearing in LTPL (discussed further in section 3.4).

3.2 INDIRECT ABSORPTION SELECTION RULES

Assigning phonons to each absorption onset may be further facilitated through the use of selection rules, which will be shown to reduce the number of allowed indirect transitions depending on the polarization of the incident light with respect to the Si–C bi-layer stacking axis \hat{c} . The derivation follows the group theory formalism and notation given in [44], and will depend on the locations of the VBM and CBM. In all cases to be considered here, the relevant valence bands have their maxima at Γ and the conduction bands have their minimum at M, and so may be handled on equal footing. The strategy will be to determine under what conditions the following probability amplitude vanishes based on its symmetry

properties alone [19]:

$$M_{0,\mathbf{K}_c} = \sum_i \frac{\langle \mathbf{K}_c | H_\Omega | i \rangle \langle i | H_\omega | 0 \rangle}{E(\mathbf{K}_c) - E_i}, \quad (3.14)$$

This is the probability amplitude given by Elliott for the second order creation of an indirect exciton in its $\mathbf{K} = \mathbf{K}_c$ ground state [19]. The sum is over a complete set of intermediate states $|i\rangle$, while H_ω and H_Ω denote the electron-photon and electron-phonon interactions, respectively.

Because the photon carries virtually no momentum, the intermediate exciton state $|i\rangle$ which it creates must also have very little momentum. This *direct exciton* can be represented in an approximate fashion by an electron in the conduction band with some wavevector \mathbf{k}_e and an empty state in the valence band with this same wavevector (this is approximate because the exciton is made up of electron and hole Bloch states with a range of wavevectors as shown in (3.1)). If the electron already lies at the CBM, the hole may be subsequently scattered by a phonon to the VBM, and the indirect exciton $|\mathbf{K}_c\rangle$ is created. On the other hand, if the hole lies at the VBM for the intermediate state, the electron is scattered to the CBM to form the indirect exciton $|\mathbf{K}_c\rangle$. Both of these processes contribute to the sum in (3.14) among a multitude of others. Because it was assumed earlier that the exciton is made up of electron and hole Bloch states at or very near the valence and conduction band extrema, the ones described will be dominant (these are both shown in Figure 4). It is possible to use band structure calculations to estimate the relative importance of various intermediate states through the size of the associated energy denominators in (3.14), as has been done in the case of diamond [45]. These considerations go beyond the group theory analysis to follow, for which we need only consider the symmetry representations of the individual factors appearing in the inner product in (3.14). For this we need to determine the ways in which each of these factors change under the various rotations, reflections, and translations for which the crystal is symmetric.

The initial state $|0\rangle$ in (3.14) represents the state of the crystal with no excitons present (i.e. the valence band is entirely full and the conduction band is entirely empty). It is assumed to have the full symmetry of the crystal, and so it must have the identity representation Γ_1 in the crystal's point group, C_{6v} . Since the overall symmetry of the expression (3.14) will be unaffected by the identity representation, it will be neglected in the following

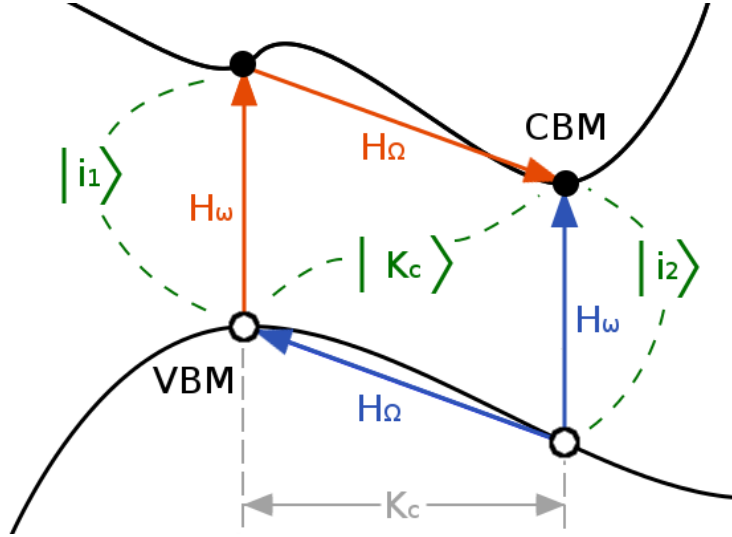


Figure 4: The second-order absorption process to create an indirect exciton with wavevector \mathbf{K}_c is represented approximately by two distinct indirect transitions of a single electron from the valence band to the conduction band (shown as orange or blue lines). Both contain intermediate, *direct* exciton states ($|i_1\rangle$ and $|i_2\rangle$) which are created when an electron is promoted from the valence band to the conduction band by a photon. Because the photon carries essentially no momentum, the transition appears vertical in the energy versus wavevector band diagram, and the electron lies in the conduction band at the same wavevector as the hole left behind in the valence band. For the intermediate state $|i_1\rangle$, the hole remains at the valence band maximum (VBM) and the electron is subsequently scattered by a phonon to the conduction band minimum (orange arrows). For $|i_2\rangle$ the electron already lies at the CBM and it is the hole that is scattered by a phonon to the VBM (blue arrows). Other processes also contribute in which the electron and hole end up displaced from the extrema (but remain separated by \mathbf{K}_c) or where the intermediate excitons are made up of more widely spaced pairs of bands. The two shown here make the largest contribution.

Table 2: Operators and wavefunctions discussed in the text categorized by their associated wavevector (derived from their translational symmetry). The symmetry point in the first Brillouin zone at which the wavevectors lie is shown along with its associated point group. The symmetry representations for the operators and wavefunctions given in the text will be labeled according to their associated point in the Brillouin zone.

Operators and wavefunctions	Wavevector	Brillouin zone point	Point group
$H_\omega, \psi_{v,\mathbf{0}}(\mathbf{r}_h), \phi(\mathbf{r})$	$\mathbf{0}$	Γ	C_{6v}
$H_\Omega, \psi_{c,\mathbf{K}_c}(\mathbf{r}_e), \Psi_{Ex}$	\mathbf{K}_c	M	C_{2v}

analysis. For a similar reason the analysis may be carried through without consideration for the symmetry of the intermediate states $|i\rangle$ (the outer product $|i\rangle\langle i|$ will always contain the identity representation). We have then for the overall symmetry of the probability amplitude:

$$\Gamma^{(\omega)} \otimes M^{(\Omega)} \otimes M^{(Ex)} \quad (3.15)$$

In the above the Γ and M representations are from among the irreducible representations of the C_{6v} and C_{2v} point groups, respectively. The point group associated with each operator and wavefunction is that of the group of its wavevector, where the wavevector is determined from its translational symmetry (in Table 2 is shown a summary of the various wavefunctions and operators to be discussed in relation to their associated point groups). Finding the overall product requires that we determine each of these in turn. In doing so, it is worthwhile to consider the explicit form for the exciton and the interactions H_ω and H_Ω to make their symmetry properties more apparent. For the case of the electron-photon interaction, we have [46]:

$$H_\omega = -\frac{eA}{m_0c} \boldsymbol{\xi} \cdot \sum_n \mathbf{p}_n \quad (3.16)$$

In the above A and $\boldsymbol{\xi}$ are the magnitude and unit vector of the vector potential in the Coulomb gauge ($\nabla \cdot \mathbf{A} = 0$), and \mathbf{p}_n are the momenta of all electrons in the solid. The wavelength of the radiation field has been assumed large enough that it is spatially uniform.

As such, H_ω must transform according to one or more of the C_{6v} irreducible representations appropriate to a wavevector at the Γ point $\mathbf{k} = \mathbf{0}$. In terms of the vector potential the electric field is given by $\mathbf{E} = (i\omega/c)\mathbf{A}$. Taking the crystal's \hat{c} axis to lie along the z -direction, we obtain from the basis functions given for the character table for C_{6v} [44] that E_z transforms as the one-dimensional representation Γ_1 and the pair (E_x, E_y) transform according to the two-dimensional representation Γ_5 .

We can express the electron-phonon interaction in the following way [47]:

$$H_\Omega = - \sum_{n,l,\alpha} \mathbf{u}_{l,\alpha} \cdot \nabla_{\mathbf{R}_{l,\alpha}} V_\alpha(\mathbf{r}_n - \mathbf{R}_{l,\alpha}) \Big|_{\mathbf{R}_{l,\alpha}^{(o)}} \quad (3.17)$$

If the ions in the solid lattice are displaced a distance $\mathbf{u}_{l,\alpha}$ about their equilibrium positions $\mathbf{R}_{l,\alpha}^{(o)}$, the above form can be regarded as the first order term in the series expansion of the unperturbed, one-electron Hamiltonian. With the primitive cells of the crystal being labeled by the index l , each ion in the cell with index α produces the potential $V_\alpha(\mathbf{r}_n - \mathbf{R}_{l,\alpha})$ acting on the n th electron. The displacement of each ion may be expressed in terms of phonon creation and annihilation operators $a_{\mathbf{q},j}^\dagger$ and $a_{\mathbf{q},j}$ [47, 48]:

$$\mathbf{u}_{l,\alpha} = \sum_{\mathbf{q},j} \sqrt{\frac{\hbar^2}{2NM_\alpha\Omega_{\mathbf{q},j}}} \boldsymbol{\epsilon}_{\mathbf{q},j} (a_{\mathbf{q},j} + a_{\mathbf{q},j}^\dagger) e^{i\mathbf{q}\cdot\mathbf{R}_{l,\alpha}}, \quad (3.18)$$

where N is the number of unit cells and M_α is the mass of the α th ion in a given unit cell. $\boldsymbol{\epsilon}_{\mathbf{q},j}$ is a unit vector containing the directions of the ion displacements for a single phonon mode from branch j and with wavevector \mathbf{q} and frequency $\Omega_{\mathbf{q},j}$. The translational symmetry of a given phonon mode is determined solely from the factor $e^{i\mathbf{q}\cdot\mathbf{R}_{l,\alpha}}$ appearing in $\mathbf{u}_{l,\alpha}$, since the potentials $V_\alpha(\mathbf{r}_n - \mathbf{R}_{l,\alpha})$ remain unchanged for any translation $\mathbf{r}_n \rightarrow \mathbf{r}_n - \boldsymbol{\tau}$, $\mathbf{R}_{l,\alpha} \rightarrow \mathbf{R}_{l,\alpha} - \boldsymbol{\tau}$. For the single principle phonon emitted in the low temperature absorption processes considered here, the associated wavevector for H_Ω is just \mathbf{K}_c , which from Table 2 corresponds to the point group C_{2v} .

The specific irreducible representation to which a given phonon belongs may be determined from its associated *displacement representation* $M^{(disp)}$. If there are m atoms per unit cell, this representation is made up of a set of $3m \times 3m$ matrices which describe the collective transformation of the displacements \mathbf{u}_α for a given phonon and a given symmetry operation.

This should account not only for the transformation of each individual atom's displacement but also the permutation of atoms within the unit cell. Using the character table for the C_{2v} point group [44], the resulting displacement representation may then be decomposed into the irreducible representations of the appropriate point group to give the individual phonon symmetries. In 4H SiC, with 8 atoms per unit cell, we have [49]:

$$M^{disp} = 8M_1 \oplus 4M_2 \oplus 4M_3 \oplus 8M_4. \quad (3.19)$$

The number multiplying each symmetry representation here shows the number of phonon modes which have that same symmetry. Thus, the principle phonons may have any one of the C_{2v} irreducible representations M_1 through M_4 .

In treating the symmetry of the exciton wavefunction we will relax the earlier assumption of isotropic valence and conduction bands in order to adhere to the C_{2v} symmetry appropriate to the exciton's wavevector \mathbf{K}_c . However, as is generally done, some of the salient features of the hydrogenic exciton will be carried through to the case with lower symmetry. For example, it may be shown (see Appendix A) that for an $n = 1$, $\mathbf{K} = \mathbf{K}_c$ hydrogenic exciton, its wavefunction may be expressed as:

$$\Psi_{Ex} = \phi_1(\mathbf{r})\psi_{c,\mathbf{K}_c}(\mathbf{r}_e)\psi_{v,\mathbf{0}}(\mathbf{r}_h) \quad (3.20)$$

The hydrogenic S orbital ϕ_1 here is called the *envelope function*, and it gives increased weight to the two Bloch functions for $|\mathbf{r}_e - \mathbf{r}_h| \approx 0$. For the case at hand, the symmetry of the exciton may therefore be expressed as the product of symmetry representations of the envelope function and the electron and hole Bloch functions [50, 51]:

$$M^{(Ex)} = \Gamma^{(\phi)} \otimes M^{(e)} \otimes \Gamma^{(h)} \quad (3.21)$$

By analogy with the hydrogenic case, the envelope function is assumed to have the full symmetry of the C_{6v} point group, and so is assumed to have the identity representation Γ_1 . We take the electron and hole Bloch functions to have the representations M_4 and Γ_5 determined from band structure calculations and given in Table III of reference [14], which are the symmetries of the highest valence band maximum and lowest conduction band minimum for 4H SiC. However, it needs to be emphasized that these are the *single group*

representations for the two band extrema, which do not account for the spin of the electron and hole. Spin will be introduced into the analysis later with the corresponding *double groups*, but for now we find:

$$M^{(Ex)} = \Gamma_1 \otimes M_4 \otimes \Gamma_5 = M_1 \otimes M_4 \otimes (M_2 \oplus M_4) = M_1 \oplus M_3, \quad (3.22)$$

using the compatibility relations $\Gamma_1 \rightarrow M_1$ and $\Gamma_5 \rightarrow M_2 \oplus M_4$ [44].

Allowed transitions will correspond to those combinations of $\Gamma^{(\omega)}$ and $M^{(\Omega)}$ which, when multiplied, give a symmetry representation containing either of the two above representations corresponding to the exciton state (3.22) [44]. For example, for a M_4 phonon and light polarized $\mathbf{E} \perp \hat{c}$ we find:

$$\Gamma^{(\omega)} \otimes M^{(\Omega)} = \Gamma_5 \otimes M_4 = (M_2 \oplus M_4) \otimes M_4 = M_1 \oplus M_3 \quad (3.23)$$

gives rise to an allowed transition. Repeating this for every possible combination gives the general result that M_1 and M_3 phonons contribute to allowed transitions for $\mathbf{E} \parallel \hat{c}$ and the others for $\mathbf{E} \perp \hat{c}$.

While it was not mentioned earlier, the fact that the exciton wavefunction may be reduced to two separate irreducible representations is physically meaningful (see (3.22)). It implies that there are two ways to combine a hole wavefunction with Γ_5 symmetry and an electron wavefunction with M_4 symmetry to form an exciton with a specified S-like envelope, and moreover these two excitons may have *distinct energies*. It originates from the fact that the Γ_5 VBM is twofold degenerate (since Γ_5 is a two-dimensional representation) and the electron wavefunction has lower point group symmetry than that of the hole (C_{2v} rather than C_{6v}). Consequently, combining the electron wavefunction with either of the two degenerate hole wavefunctions lifts the degeneracy.

The problem with this analysis is that the twofold degenerate VBM in 4H SiC is already split by the spin-orbit interaction (this didn't appear before because spin had been left out). Since the Coulomb attraction between the electron and hole acts as a perturbation on the one-electron band structure, it would seem more appropriate to include spin at the outset (i.e. before forming the product in (3.21) determining the exciton symmetry). For the Γ_5 VBM we can do so by multiplying the two degenerate *spatial* wavefunctions $\phi_1^{(5)}$ and $\phi_2^{(5)}$ by

the spinors $|\uparrow\rangle$ and $|\downarrow\rangle$. Within the C_{6v} point group the pair of spinors transform as the two-dimensional representation Γ_7 , a double group representation with the fermionic property of being odd under 360° rotations. The four spinor functions so obtained transform as the direct product:

$$\Gamma^{(h)} \rightarrow \Gamma_5 \otimes \Gamma_7 = \Gamma_7 \oplus \Gamma_9 \quad (3.24)$$

It is seen that the VBM separates into two separate bands of either Γ_7 or Γ_9 symmetry, both of which are twofold degenerate. Their energy separation is a result of the spin-orbit interaction [52]:

$$H_{so} = \frac{\hbar}{4m_0c^2}(\boldsymbol{\sigma} \cdot \nabla V) \times \mathbf{p}, \quad (3.25)$$

where $\boldsymbol{\sigma}$ are the Pauli matrices, V is the one-electron self-consistent potential without spin-orbit interaction, and \mathbf{p} is the electron momentum. Table III in reference [14] indicates that the higher of the two valence band maxima has symmetry Γ_9 , and the splitting is determined to be $\Delta_{so} = 8.6$ meV [13, 14]. To include the spin of the electron we multiply the electron's spatial wavefunction $\phi^{(4)}$ by the spinors $|\uparrow\rangle$ and $|\downarrow\rangle$. In the C_{2v} group the spinors transform as the two-dimensional double group representation M_5 . Similarly as with the holes, these two electron states transform as:

$$M^{(e)} \rightarrow M_4 \otimes M_5 = M_5 \quad (3.26)$$

Taking the hole to be localized to the upper Γ_9 VBM, we make the substitutions $M^{(e)} = M_5$ and $\Gamma^{(h)} = \Gamma_9$ in the expression (3.21) for the overall exciton symmetry:

$$M^{(Ex)} = \Gamma_1 \otimes M_5 \otimes \Gamma_9 = M_5 \otimes M_5 = M_1 \oplus M_2 \oplus M_3 \oplus M_4, \quad (3.27)$$

where we have used the compatibility relation $\Gamma_9 \rightarrow M_5$ [44]. The sum over the four one-dimensional representations indicates that the lowest lying exciton band $E_1(\mathbf{K})$ splits into *four* distinct sub-bands. Because the reduction in symmetry here still originates from the mass anisotropies of the electron and hole, this again may be viewed as a form of mass anisotropy splitting, only this time with a fourfold degeneracy being broken. Furthermore, now that the interacting electron and hole both have spin, it is expected that an exchange interaction would be at play in separating each of these sub-levels from one another in energy.

Calculations suggest its effect is small [53, 54], and in the case of silicon it has been argued from far-IR exciton absorption measurements that exchange splittings on the order of several tens of μeV have been observed [55]. A direct comparison of the present case to the one for silicon cannot be made because of its cubic symmetry, but it is expected that the overall exciton fourfold sub-level structure will be determined to a large extent by the effects of electron and hole mass anisotropy, with the exchange interaction introducing minor shifts to each of these levels. In Figure 5 an overview is given of the preceding development, starting with the spin-orbit splitting of the valence band maximum and ending with the fourfold splitting of the free exciton ground state.

Although this analysis was carried through for the exciton whose hole occupies the uppermost Γ_9 VBM (this will be called exciton EX_1 from now on), it may be shown that the same result is found for an exciton whose hole lies at *any* valence band maximum at Γ and whose electron lies at *any* conduction band minimum at M. Besides EX_1 , three other excitons which share this property will be considered here, which we designate EX_{so} , EX_{cf} , and EX_2 . EX_{so} consists of an electron in the lowest conduction band minimum and a hole in the second highest valence band maximum, split off from the topmost by the spin-orbit interaction. EX_{cf} also consists of an electron in the lowest conduction band minimum but has its hole occupying the third lowest valence band maximum whose separation from the topmost is referred to as the crystal field splitting (the splitting is a result of the uniaxial symmetry of the host crystal). The exciton EX_2 has its hole occupying the topmost valence band but its electron occupies the second lowest conduction band (see Table 3 for an overview of the valence and conduction bands that make up each of the preceding excitons). In the exciton's energy versus wavevector diagram, each of these should contribute an additional quadruplet of bands with minima lying at the point $\mathbf{K} = \mathbf{K}_c$, as shown in Figure 6. Each of these exciton band minima may therefore give rise to its own series of indirect absorption onsets in the same manner as described above. Other combinations of conduction band and valence band extrema may also be taken into account, but based on the band structure calculations for 4H SiC [12, 13, 14, 11, 15, 56] the energy separations of each of these pairs of extrema lie outside the range of energies studied here.

At this point we can return to the question of selection rules, performing the same

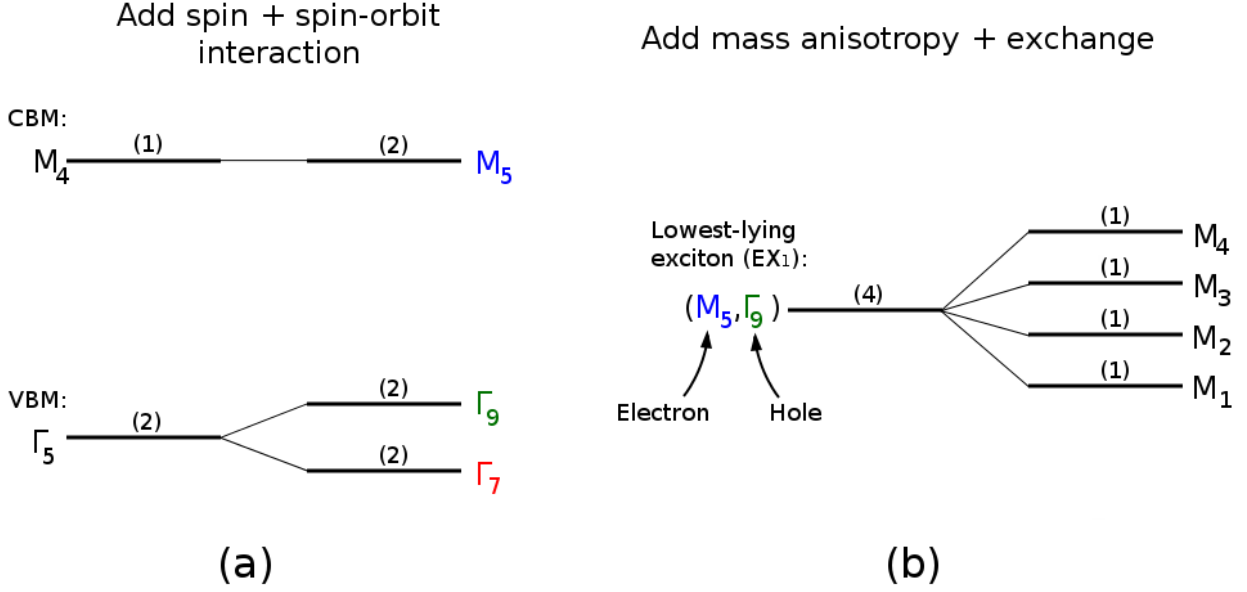


Figure 5: (a) Conduction band minimum (CBM) and valence band maximum (VBM) upon including electron spin and spin-orbit interaction. Due to spin-orbit interaction the Γ_5 VBM splits into two separate bands of Γ_7 and Γ_9 symmetry while the CBM changes from M_4 to M_5 symmetry. (b) When combining the electron in the M_5 symmetry conduction band minimum with the hole in the topmost valence band maximum (whose symmetry is Γ_9) an exciton is formed whose energy undergoes a fourfold splitting due to mass anisotropy and exchange interaction. All levels are shown with their degeneracy labeled in parentheses. This combination of electron and hole is referred to as EX_1 , and will give rise to the lowest energy states of the exciton. Another possibility not shown in this figure is that for which the electron in the conduction band minimum is combined with the hole in the second lowest valence band maximum, with symmetry Γ_7 .

Table 3: The four different classes of exciton described in this work (EX_1 , EX_{so} , EX_{cf} , EX_2) differ from one another in the valence and conduction band extrema occupied by their electron and hole. The positions of those extrema are shown for each case along with their corresponding symmetry [14]. The double group symmetry representations in parentheses accompany their associated single group representations.

Exciton	Electron		Hole	
	Conduction band	Symmetry	Valence band	Symmetry
EX_1	Lowest	$M_4(M_5)$	Highest	$\Gamma_5(\Gamma_9)$
EX_{so}	Lowest	$M_4(M_5)$	Second Highest	$\Gamma_5(\Gamma_7)$
EX_{cf}	Lowest	$M_4(M_5)$	Third Highest	$\Gamma_1(\Gamma_7)$
EX_2	Second Lowest	$M_1(M_5)$	Highest	$\Gamma_5(\Gamma_9)$

procedure as before but now with the form (3.27) for $M^{(Ex)}$. In doing so we look for the optically active sub-levels from the exciton quadruplet $M_1 \oplus M_2 \oplus M_3 \oplus M_4$, which are those representations contained in the product $\Gamma^{(\omega)} \otimes M^{(\Omega)}$. The result can be summarized as follows: for $\mathbf{E} \parallel \hat{c}$, the optically active exciton sub-level is that which has the same symmetry as the participating phonon. For $\mathbf{E} \perp \hat{c}$, the pair of sub-levels M_1 and M_3 will be *simultaneously* active for any given M_2 or M_4 phonon, and the pair M_2 and M_4 will be *simultaneously* active for any given M_1 or M_3 phonon. Since *two* sub-levels are always active for $\mathbf{E} \perp \hat{c}$, a twofold splitting may be observed at each absorption onset in this polarization.

In contrast to the analysis without spin, *all* phonons regardless of their symmetry may participate in allowed transitions for both $\mathbf{E} \parallel \hat{c}$ and $\mathbf{E} \perp \hat{c}$. In Section 5.2 it will be shown that this is very clearly not borne out in the measurements, which show that only a subset of the principle phonons contribute to observable absorption onsets in a given polarization, in agreement with the group theory prediction that neglected spin. This does not necessarily mean that the analysis that includes spin is incorrect, since it may still be true that those missing onsets are simply too weak to observe. Since the symmetry arguments given above do not distinguish weak electronic transitions from strong ones, the following scheme is

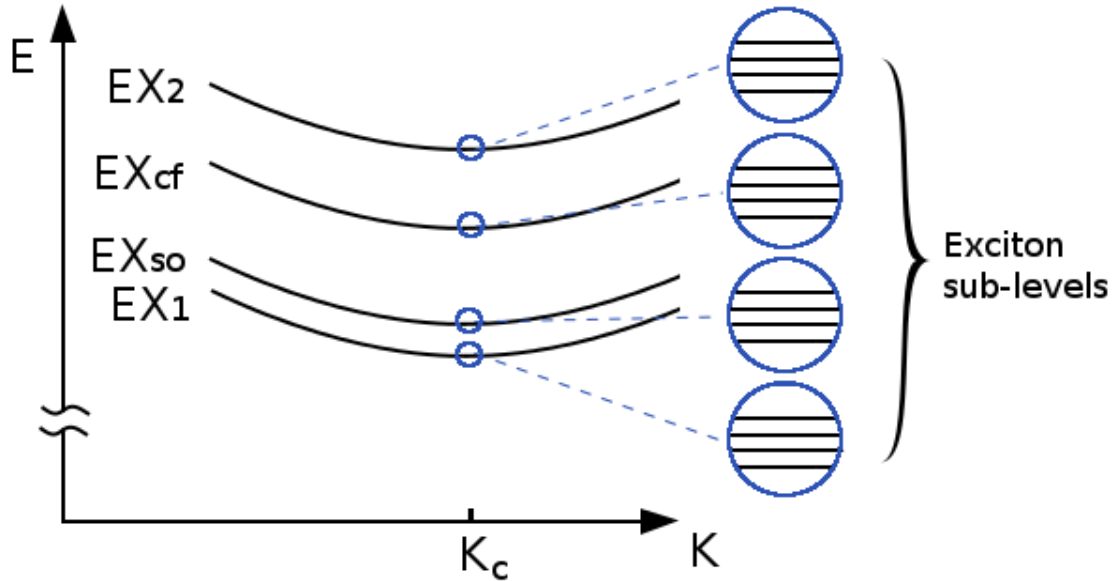


Figure 6: Four of the lowest-lying exciton bands in 4H SiC are shown with their minima all at the point $\mathbf{K} = \mathbf{K}_c$ in the Brillouin zone, which is the same point, M, as the conduction band minimum. Each of these bands breaks up into a series of four sub-bands due the mass anisotropy of the electron and hole and exchange interaction. The sub-level spacing is shown identical in all cases for simplicity, but this is likely not to be true. Each group of four sub-bands is associated with an exciton whose electron and hole occupy a distinct combination of valence and conduction band extrema as described in the text and summarized in Table 3.

proposed:

Firstly, the fourfold splitting of the exciton ground state is *rigorously true*, as are the selection rules showing which of the four sub-levels will be active for the various combinations of photon and phonon symmetries. Second, the selection rules derived for the case without spin are also true *to good approximation*. Namely, for the two lowest-lying excitons EX_1 EX_{so} whose hole occupies a state derived from Γ_5 symmetry, only M_1 and M_3 symmetry phonons will be active for $\mathbf{E} \parallel \hat{c}$, and only M_2 and M_4 symmetry phonons will be active for $\mathbf{E} \perp \hat{c}$. This idea is shown pictorially in Figure 7, which shows all of the allowed transitions derived for the case with spin while also distinguishing those transitions which would have been found to be forbidden in the case without spin. It is seen from the figure that among all transitions that were found to be allowed in both group theory treatments (i.e. the solid lines in the figure), only two of the four exciton sub-levels are ever active: M_1 and M_3 . Nevertheless, it may still be possible to observe these two simultaneously when the light is polarized $\mathbf{E} \perp \hat{c}$. A similar strategy can be devised for the higher energy excitons EX_{cf} and EX_2 , although this hasn't been necessary due to their considerable lifetime broadening, which will be seen in section 5.6 to obscure these very small splittings.

At issue here is the underlying hierarchy of the various interactions at work in the exciton system: the Coulomb interaction of the lattice with the electron and hole, the Coulomb interaction between the electron and hole (and associated exchange interaction), and spin-orbit coupling. The situation seems to bear some similarities with the Russell-Saunders limit in the study of atomic energy levels and spectra [57, 58]. In this limit, the spin-orbit coupling in the atom is regarded as small so that the total orbital angular momentum L and total spin S may be considered good quantum numbers for the electronic eigenstates. In other words, the spatial part of the system and its spin part may be handled independently of one another, as was done in the analysis given above in which spin was neglected. Assessing the validity of this assumption for the present case of the exciton system lies outside the scope of this work, and so for the time being we simply take the scheme proposed above as being true, operationally.

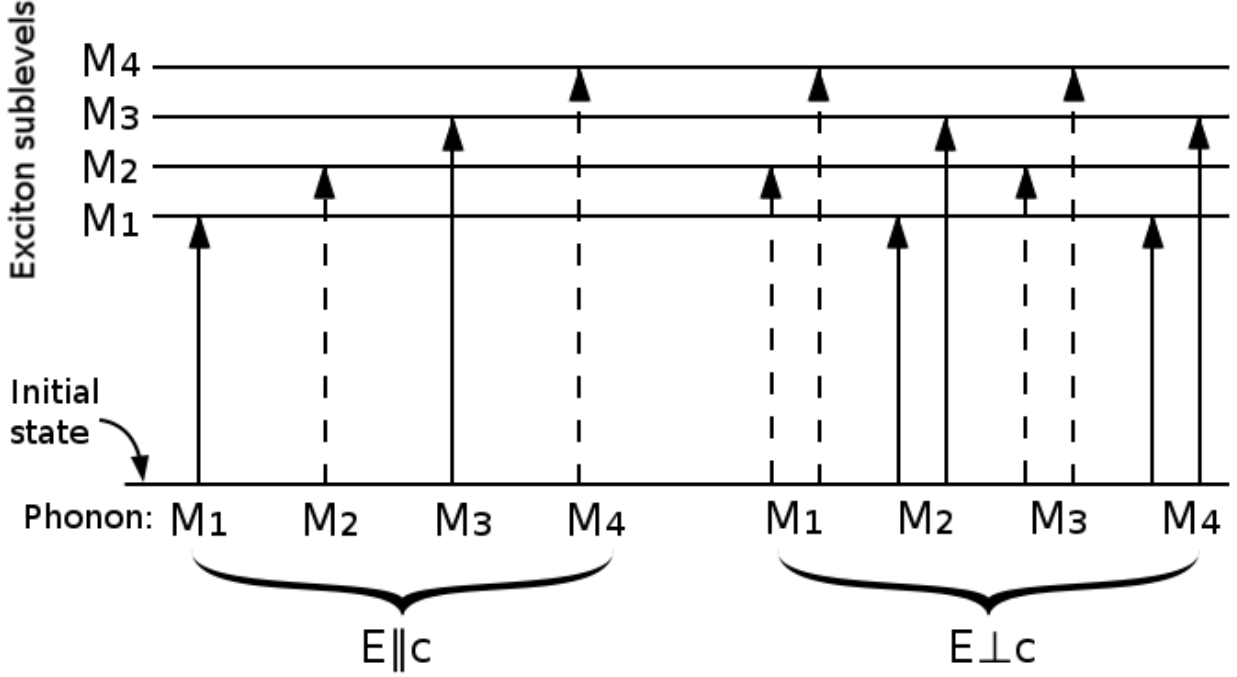


Figure 7: Overview of the derived selection rules for phonon-assisted optical absorption due to the indirect exciton in 4H SiC with inclusion of electron and hole spin. The upper levels representing the final states make up the indirect exciton ground state split by mass anisotropy and exchange interaction as described in the text. The allowed transitions to these sub-levels for light polarized $\mathbf{E} \parallel \hat{c}$ are shown by the group of vertical arrows on the left, with the symmetry of the participating phonon shown below the corresponding arrow (note that the arrows are shown vertical for convenience, and are not meant to indicate direct transitions). The allowed transitions for $\mathbf{E} \perp \hat{c}$ are shown by the group to the right. The fact that there are two arrows for each phonon symmetry implies that a single phonon will give rise to a *pair* of absorption onsets which are separated by the same energy spacing as the pair of active exciton sub-levels. For the two lowest energy excitons EX_1 and EX_{so} , the allowed transitions shown here as dotted lines indicate a combination of phonon symmetry and electric field polarization which was found to be forbidden in the group theory analysis neglecting spin. It is proposed that these are too weak to observe despite being allowed transitions according to the full group theory analysis with spin.

3.3 ENERGY BAND NONPARABOLICITY

A second problem with the simple hydrogenic model for the exciton which was alluded to earlier is the implicit assumption in the effective mass approximation that the electron and hole both occupy energy bands parabolic in wavevector \mathbf{k} . For the electron occupying the conduction band in 4H SiC, this seems to be a rather good assumption based on the calculated band structure (see Figure 9a in [15]). However, in 4H SiC the three uppermost valence bands at the point Γ undergo avoided crossings with each other along wavevectors \mathbf{k} in the Γ -M-K plane [12, 14, 20, 15]. In the regions of the avoided crossings, the energy bands are strongly nonparabolic as the curvatures of the two bands are interchanged on passing from one side of the crossing to the other. In particular, this occurs between the uppermost valence band and the spin-orbit split-off band in the near vicinity of their maxima as well as between the spin-orbit split-off band and the crystal-field split-off band (these may be seen in figures 37 and 38 of section 5.5).

Because the curvatures of the valence and conduction band extrema determine the effective masses of the electron and hole that make up the exciton, the energy levels (3.8) of the exciton are altered in two ways: One is through the reduced mass μ , which determines the exciton binding energy in the hydrogenic model. The other is through the total mass M , which is seen from (3.8) to describe the curvature of the hydrogenic exciton bands $E_n(\mathbf{K})$ through the center of mass kinetic energy term. Whereas μ determines the positions of the absorption thresholds, the M will determine their shape in the absorption spectrum as the photon energy is increased above those thresholds. The latter will be given consideration here, although one should note that in the more realistic case with anisotropic electron and hole effective masses, the roles μ and M play are not so easily separated.

Taking the hydrogenic model as a starting point, one might account for the nonparabolicity in the valence and conduction bands by allowing the exciton's total mass to become \mathbf{K} -dependent: $M(\mathbf{K} - \mathbf{K}_c) = m_e(\mathbf{K} - \mathbf{K}_c) + m_h(\mathbf{K} - \mathbf{K}_c)$, where now the electron and hole masses are no longer constants (as would be the case for constant-curvature, parabolic bands), but vary with the displacement $\delta\mathbf{k} = \mathbf{K} - \mathbf{K}_c$ away from the corresponding valence and conduction band extrema. This is complicated by the fact that both m_e and m_h will in

general have a tensor character (see (3.3)). However, if one of these—say, m_h —is much larger, it might be expected that the curvature of the exciton bands is dominated to a large extent by that of the valence band. This would suggest the following substitution:

$$\frac{\hbar^2 (\mathbf{K} - \mathbf{K}_c)^2}{2M} \rightarrow -E_v(\mathbf{K} - \mathbf{K}_c), \quad (3.28)$$

where $E_v(\mathbf{K} - \mathbf{K}_c)$ expresses the full anisotropy and nonparabolicity of the valence band for displacements $\mathbf{K} - \mathbf{K}_c$ about its maximum (the minus sign in the above expression is to account for the fact that the energy of the hole is the negative of the energy of the missing electron). With this substitution having been made we have from the Golden rule that the transition rate into the exciton state $|\mathbf{K}\rangle$ is proportional to:

$$\begin{aligned} \Gamma_{0 \rightarrow \mathbf{K}} &\propto |M_{0, \mathbf{K}}|^2 \delta(\hbar\omega - E(\mathbf{K}) - \hbar\Omega(\mathbf{K})) \\ \Gamma_{0 \rightarrow \mathbf{K}} &\propto |M_{0, \mathbf{K}}|^2 \delta(\hbar\omega - [E_{gx} - E_v(\mathbf{K} - \mathbf{K}_c)] - \hbar\Omega(\mathbf{K})) \end{aligned} \quad (3.29)$$

The probability amplitude $M_{0, \mathbf{K}}$ is the same as given in (3.14) only without restricting \mathbf{K} to the exciton band minimum \mathbf{K}_c . To compute the absorption coefficient from this we integrate over exciton wavevectors \mathbf{K} , and if we assume that both the probability amplitude and phonon energy $\hbar\Omega(\mathbf{K})$ do not vary considerably from their values at $\mathbf{K} = \mathbf{K}_c$, we have the result:

$$\begin{aligned} \alpha &\propto \int d^3K \Gamma_{0 \rightarrow \mathbf{K}} \approx |M_{0, \mathbf{K}_c}|^2 \int d^3K \delta(\hbar\omega - [E_{gx} - E_v(\mathbf{K} - \mathbf{K}_c)] - \hbar\Omega(\mathbf{K})) \\ &\approx 4\pi^3 |M_{0, \mathbf{K}_c}|^2 N_v(E_{gx} + \hbar\Omega(\mathbf{K}_c) - \hbar\omega), \end{aligned} \quad (3.30)$$

where $N_v(E)$ is the density of states for the valence band [59]:

$$N_v(E) = \frac{1}{4\pi^3} \int d^3K \delta(E - E_v(\mathbf{K})). \quad (3.31)$$

For a spherical, isotropic valence band with effective mass m we have:

$$\begin{aligned} N_v(E) &= \frac{1}{4\pi^3} \int d^3K \delta(E - (-\hbar^2 K^2/2m)) \\ &= \frac{1}{\pi^2} \int dK K^2 (m/\hbar^2 K) \delta\left(K - \sqrt{-2mE/\hbar^2}\right) = \frac{\sqrt{2m^3}}{\pi^2 \hbar^3} \sqrt{-E} \end{aligned} \quad (3.32)$$

The square root dependence on the energy here is the origin of the predicted square root dependence of the absorption coefficient on the photon energy (note that the top of the

valence band has been defined to be zero, so $-E$ is positive below the maximum). In this case the density of states is also proportional to $m^{3/2}$, and so the interchange of band curvatures at an avoided crossing should be observable in $N_v(E)$ and, by extension, the absorption coefficient α . By comparing to band structure calculations, it will be shown in Section 5.5 that an avoided crossing between the top two valence bands clearly manifests in several locations in the WMA absorption spectrum of 4H SiC.

3.4 LOW TEMPERATURE PHOTOLUMINESCENCE

The assignment of specific features in the absorption spectrum is complicated by the fact that multiple exciton energy bands—each with a distinct excitonic band gap $E_{gx}^{(i)}$ —may give rise to an observed absorption onset. Furthermore, these excitonic bandgaps are measurable only up to a particular principal phonon energy $\hbar\Omega_j$, since the measured onset energies are given by $\hbar\omega_{ij} = E_{gx}^{(i)} + \hbar\Omega_j$. This ambiguity can be alleviated to some extent if one has measured the low temperature photoluminescence spectrum. As with the low temperature absorption spectrum, the LTPL spectrum should consist of indirect processes with emission of a principal, momentum-conserving phonon. In this case, however, the energy given up by the exciton is $\Delta E = \hbar\omega_{ij} + \hbar\Omega_j$, and if the exciton lied at a particular exciton band minimum, $E = E_{gx}^{(i)}$, $\mathbf{K} = \mathbf{K}_c$, the emitted photon energy observed is given by:

$$\hbar\omega_{ij}^{(e)} = E_{gx}^{(i)} - \hbar\Omega_j = \hbar\omega_{ij}^{(a)} - 2\hbar\Omega_j, \quad (3.33)$$

where $\hbar\omega_{ij}^{(a)} = E_{gx}^{(i)} + \hbar\Omega_j$ is the *absorption* threshold corresponding to the same exciton state and phonon. The combined absorption and emission spectrum will therefore have a mirror symmetry about the exciton bandgap $E_{gx}^{(i)}$ so that the pairs $(\hbar\omega_{ij}^{(e)}, \hbar\omega_{ij}^{(a)})$ may be identified (see Figure 8). Using these one can then compute both the principal phonon energy and the exciton ground state energy:

$$E_{gx}^{(i)} = (\hbar\omega_{ij}^{(a)} + \hbar\omega_{ij}^{(e)})/2 \quad (3.34)$$

$$\hbar\Omega_j = (\hbar\omega_{ij}^{(a)} - \hbar\omega_{ij}^{(e)})/2 \quad (3.35)$$

This is also facilitated by the fact that excitons occupying only the lowest available energy states contribute to the overall LTPL spectrum. In contrast, by measuring the low temperature absorption spectrum, the experimenter has specified the amount of energy imparted to the exciton (up to a principle phonon energy) in the choice of the incident light's wavelength, and so the exciton's final state has to some extent been pre-determined by the energy and momentum conservation conditions discussed previously. Once the exciton has been created, however, it is free to equilibrate with the surrounding thermal bath (through scattering with phonons, say) such that its state before recombination reflects the bath temperature T . If we enumerate the bands by $E^{(i)}(\mathbf{K})$ and take the lowest-lying of these bands to have a minimum energy $E_{gx}^{(1)}$, the transition rate $\Gamma_{i,\mathbf{K}\rightarrow 0}$ for recombination of an exciton from each of these bands must be weighted by the Boltzmann factor $e^{-(E^{(i)}(\mathbf{K})-E_{gx}^{(1)})/kT}$. To compute the intensity of the emitted light for a specified momentum-conserving phonon, we perform a similar integration as in (3.30) but with the Boltzmann factor included:

$$\begin{aligned} I(\hbar\omega) &\propto \sum_i \int d^3K e^{-(E^{(i)}(\mathbf{K})-E_{gx}^{(1)})/kT} \Gamma_{i,\mathbf{K}\rightarrow 0} \\ &\propto \sum_i |M_{i,\mathbf{K}_c;0}|^2 \int d^3K e^{-(E^{(i)}(\mathbf{K})-E_{gx}^{(1)})/kT} \delta(\hbar\omega - E^{(i)}(\mathbf{K}) + \hbar\Omega(\mathbf{K})) \\ &\propto \sum_i |M_{i,\mathbf{K}_c;0}|^2 e^{-(\hbar\omega + \hbar\Omega(\mathbf{K}_c) - E_{gx}^{(1)})/kT} N_i(\hbar\omega + \hbar\Omega(\mathbf{K}_c)), \end{aligned} \quad (3.36)$$

where $N_i(E)$ is the density of states [59] for the exciton band $E^{(i)}(\mathbf{K})$. Note that it has again been assumed that the probability amplitude $M_{i,\mathbf{K};0}$ and phonon energy $\hbar\Omega(\mathbf{K})$ do not vary from their values at $\mathbf{K} = \mathbf{K}_c$. Also, the required normalizing factor

$$\left[\int d^3K e^{-(E^{(i)}(\mathbf{K})-E_{gx}^{(1)})/kT} \right]^{-1} \quad (3.37)$$

has been left out for simplicity (this should be proportional to $T^{-3/2}$ for a parabolic exciton band). Expression (3.36) is most often given for a single parabolic exciton band for which $N(E) \propto \sqrt{E - E_{gx}}$ [60, 61]:

$$I(\hbar\omega) = A e^{-(\hbar\omega + \hbar\Omega(\mathbf{K}_c) - E_{gx})/kT} \sqrt{\hbar\omega + \hbar\Omega(\mathbf{K}_c) - E_{gx}}, \quad (3.38)$$

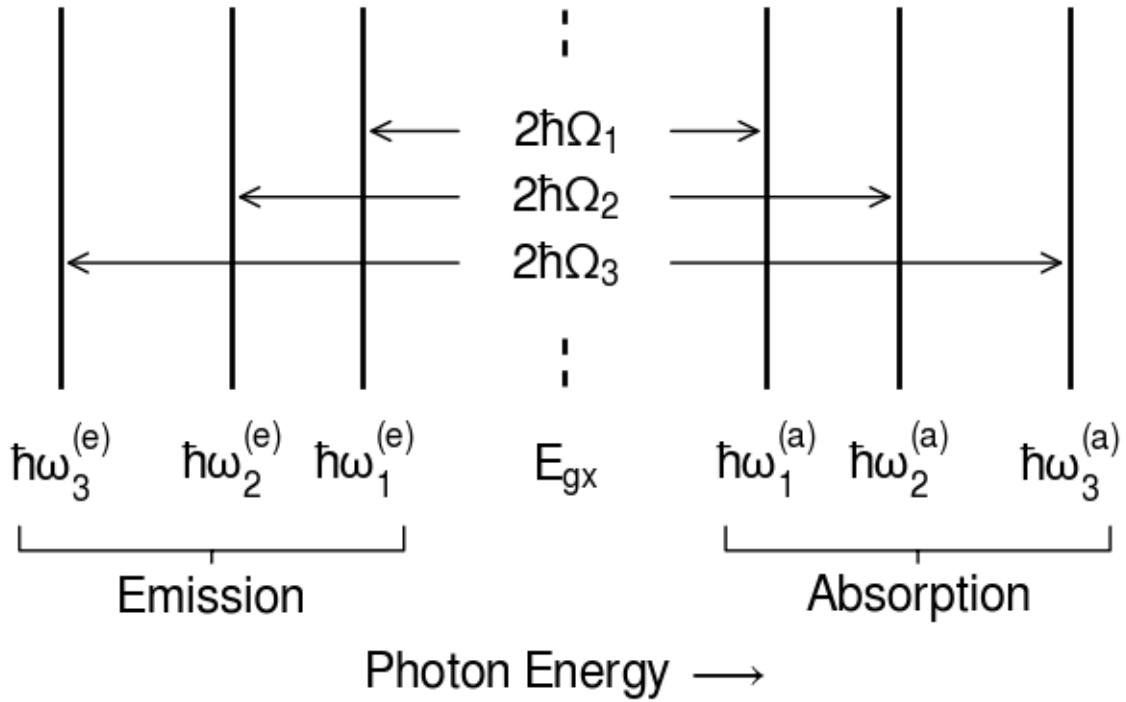


Figure 8: A single exciton ground state with energy E_{gx} will give rise to a series of phonon-assisted emission lines at the photon energies $\hbar\omega_{i,e} = E_{gx} - \hbar\Omega_i$ and a series of absorption onsets at the photon energies $\hbar\omega_{i,a} = E_{gx} + \hbar\Omega_i$. The mirror symmetry about the exciton ground state energy can be used to determine E_{gx} and the principal phonon energies $\hbar\Omega_i$ if one has measured both the absorption and emission spectrum.

where A is a scaling constant. Like the absorption coefficient, this too contains a square root onset, although here it is strongly suppressed by the Boltzmann factor for photon energies higher than a few kT beyond the threshold. This produces an asymmetric peak in the LTPL spectrum whose maximum lies at $\hbar\omega = E_{gx} - \hbar\Omega(\mathbf{K}_c) + kT/2$. For the more complicated expression (3.36) involving multiple exciton bands, the Boltzmann factor may almost entirely suppress photoluminescence from exciton bands higher than a few kT from the minimum of the lowest band. A demonstration of this fact can be seen in Figure 9, which shows the photoluminescence spectrum due to a single principal phonon and three exciton bands with minima $E_{gx}^{(1)} < E_{gx}^{(2)} < E_{gx}^{(3)}$. Assuming the transitions are allowed, each of these may give rise to a peak in the photoluminescence spectrum of the form (3.38), but it is seen that at the lowest temperature T_1 , all but the lowest of these is observable. The corresponding absorption onsets are also shown in the figure, each positioned symmetrically about the associated band minima $E_{gx}^{(i)}$ as described earlier. They are plotted as they would appear even at absolute zero, and so it is seen that even for very low temperatures each exciton band may discernibly contribute to the absorption spectrum (not counting selection rules). In this respect the measurement of LTPL is simpler to analyze at low temperatures, while the measurement of the absorption spectrum has greater capability to probe higher energy states of the exciton.

In silicon carbide the LTPL spectrum is complicated by the prominence of radiative recombination processes other than those described above, particularly those due to *bound excitons*. All of the preceding discussion up to this point has dealt with what are called *free excitons*, which are bound electron-hole pairs that are free to move about the solid *as a whole* with a well-defined momentum $\hbar\mathbf{K}$. Bound excitons on the other hand are bound electron-hole pairs which are themselves bound to a defect. In silicon carbide the defect in question is most often a nitrogen atom substituting for a carbon atom [62, 27, 63]. For the same reasons as just discussed, LTPL from these excitons will begin to outweigh that from the higher energy free excitons even for nitrogen concentrations on the order of 10^{15} cm^{-3} (on the other hand, this is also why absorption due to bound excitons is typically negligible compared to free exciton absorption).

To get around this, samples have been chosen with high enough purity that this inter-

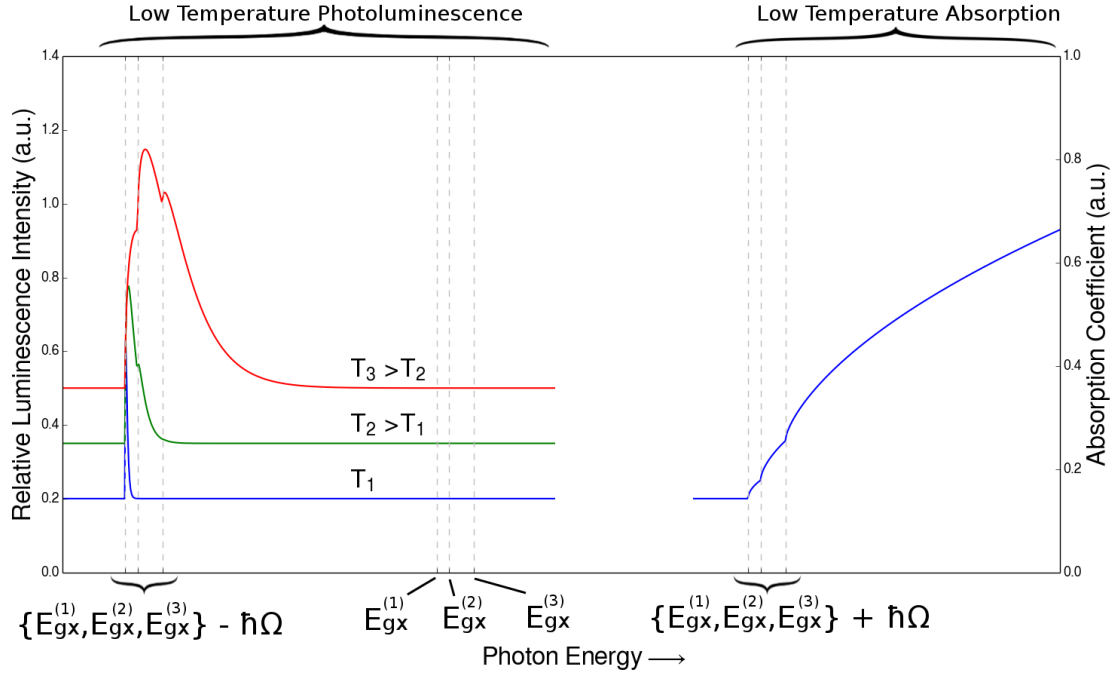


Figure 9: The three curves on the left simulate low temperature photoluminescence (LTPL) due to indirect exciton recombination radiation at three different temperatures, $T_1 < T_2 < T_3$. Each contain contributions from excitons occupying one of three bands whose minima lie at the marked positions $E_{gx}^{(1)}$, $E_{gx}^{(2)}$, and $E_{gx}^{(3)}$. The phonon-assisted recombination radiation may appear as a peak shifted down in energy from each of these minima by an amount equal to the particular principal phonon energy involved: $\hbar\Omega$. Because the exciton has thermalized with its surrounding environment before recombination, the peaks develop a high energy tail due to the exciton's kinetic energy. In addition, only those exciton bands lying within a few kT of the lowest exciton band minimum will give rise to observable LTPL. Raising the temperature may allow the contribution of these higher bands to become visible (for clarity the peak amplitudes have not been properly normalized according to (3.37)). The analogous onsets of indirect absorption appear towards higher photon energies, with each being shifted up from the corresponding exciton band minima by the same energy $\hbar\Omega$. In the absorption spectrum all exciton bands may be observed as long as the energy and momentum conservation conditions are fulfilled, even at absolute zero temperature.

ference can be to some extent avoided and the intrinsic properties of the free excitons may be studied with greater clarity. However, historically the optical spectra of silicon carbide have been measured with relatively impure samples, and so for the sake of comparison it is important to understand the differences between the emission spectra for free and bound excitons. For bound excitons in indirect semiconductors the emission spectrum consists of a single “no-phonon” peak and a series of phonon “replicas.” The no-phonon line is interpreted to be the result of bound exciton recombination for which the exciton’s momentum is transferred to the defect instead of a phonon. It is presumed that negligible energy is transferred to the defect [64], and so this line occurs at $\hbar\omega = E_{gx}^{(1)} - E_{Dx}$, where $E_{gx}^{(1)}$ is the absolute minimum of the free exciton bands and E_{Dx} is the binding energy of the bound exciton to the defect. For the nitrogen-bound exciton, the binding energy E_{Dx} will depend on the specific carbon site in the unit cell at which the nitrogen atom is substituted, and each of these sub-species of bound exciton will give rise to its own set of emission lines. In 4H SiC there are two such sites, and the resulting emission lines are typically denoted either P or Q. The phonon replicas are offset from the no-phonon line to lower energies, and the amounts by which they are offset are nearly identical with the offsets of the free exciton emission lines from $E_{gx}^{(1)}$. For this reason the phonon replicas are interpreted as being due to bound exciton recombination with emission of the same principal phonons that are involved in free exciton recombination.

In silicon carbide, the energies of these principal phonons have often been determined from measurements of the positions of the bound exciton phonon replicas relative to that of the corresponding no-phonon line [27, 63]. It is important to note, however, that the principal phonon energies as determined from bound exciton photoluminescence do show small discrepancies compared to the same phonon energies determined from free exciton photoluminescence. This has been reported in [65], but it will also be demonstrated in the LTPL measurements presented here. The origin of these discrepancies is not currently understood, although it may have something to do with the fact that the momentum of the bound exciton is not well-defined (due to its localization). In this case recombination can occur with emission of phonons with a range of wavevectors—not just \mathbf{K}_c —and therefore a range of phonon energies. This has been discussed in relation to the *broadening* of the bound exciton

phonon replicas in silicon [66], although no specific mention is made of energy shifts. Since it is important in this work to determine the exact principal phonon energies, it is extremely advantageous that LTPL measurements be performed on high purity samples such that only free exciton recombination is observed.

4.0 BACKGROUND: EXPERIMENT

In this section the experimental details for measuring both wavelength modulated absorption and low temperature photoluminescence in 4H SiC will be discussed. Attention will be given in particular to the use and optimization of the apparatus for taking wavelength modulated absorption (WMA) measurements, to which most of the technical innovations in this work have been directed, although some discussion will also be devoted to taking low temperature photoluminescence (LTPL) measurements. At the end of this section the procedures for sample preparation will be given.

4.1 WAVELENGTH MODULATED ABSORPTION

4.1.1 Basic operating principles

For this work it is not so important to determine the form of the absorption coefficient itself as it is to determine the precise energy positions of the absorption onsets. The wavelength modulated absorption technique is particularly advantageous in this respect, since the quantity obtained in this case is proportional to the wavelength derivative of the absorption coefficient. From the form given in (3.12) we have for the wavelength derivative:

$$\begin{aligned}\frac{d\alpha}{d\lambda} &\propto \frac{d}{d\lambda} \sqrt{\hbar\omega - E_{gx} - \hbar\Omega} \\ &\propto \frac{d(\hbar\omega)}{d\lambda} (\hbar\omega - E_{gx} - \hbar\Omega)^{-1/2} \\ &\propto -\frac{hc}{\lambda^2} (\hbar\omega - E_{gx} - \hbar\Omega)^{-1/2} \\ &\propto -\frac{(\hbar\omega)^2}{hc} (\hbar\omega - E_{gx} - \hbar\Omega)^{-1/2},\end{aligned}\tag{4.1}$$

The most significant part of the dependence on $\hbar\omega$ comes from the inverse-square-root, and so for the present purposes we will ignore the factors coming from $d(\hbar\omega)/d\lambda$. In contrast with the rounded, step-like onset in α , its derivative produces a sharp rise at the onset energy $\hbar\omega = E_{gx} + \hbar\Omega$ and a high energy tail. The singularity at the onset is broadened in a manner to be discussed in Section 5.1. In most cases this broadening is due in large part to the instrumental resolution, but in a few others it may be inherent to the sample.

The measurement of $d\alpha/d\lambda$ is made possible by modulating the wavelength of the light incident on the sample about some fixed wavelength λ_o . To see how, we may expand the transmitted intensity (3.11) about λ_o :

$$\begin{aligned} I(\lambda) &\approx I(\lambda_o) + \left. \frac{dI}{d\lambda} \right|_{\lambda_o} (\lambda - \lambda_o) \\ &\approx I(\lambda_o) + \left[\frac{dI_o}{d\lambda} (1-R)^2 e^{-\alpha x} - 2I_o(1-R) \frac{dR}{d\lambda} - I_o(1-R)^2 x \frac{d\alpha}{d\lambda} e^{-\alpha x} \right]_{\lambda_o} (\lambda - \lambda_o) \end{aligned} \quad (4.2)$$

While the third term in the brackets contains the desired quantity, it is necessary to ensure that the the other two terms are either small by comparison or, more importantly, do not contribute any structure to the spectrum that could be misconstrued as that due to the sample. In the spectral range of interest, the second term is likely to be small [38], and the more serious concern is the one involving the wavelength derivative of the incident light intensity. For the time being it will be assumed to be negligible as well, although it will be shown that under certain conditions extra precautions need to be made to counteract its influence on the measurement. In these cases one may also need to account for the wavelength dependence of the detector responsivity, which was not included in the above expression.

If the wavelength is now modulated sinusoidally about λ_o with a small amplitude $\Delta\lambda$, the resulting transmitted intensity is in turn modulated about $I(\lambda_o)$ with the amplitude:

$$\Delta I = -I_o(1-R)^2 x \frac{d\alpha}{d\lambda} e^{-\alpha x} \Delta\lambda = -I(\lambda_o) x \left. \frac{d\alpha}{d\lambda} \right|_{\lambda_o} \Delta\lambda \quad (4.3)$$

With a detector put in place to measure the light intensity, a lock-in amplifier (L1) referenced to the wavelength modulation frequency f_λ may then extract the modulation from the overall signal from the detector. The factor $I(\lambda_o)$ may be eliminated by dividing ΔI by the DC

component in (4.2). However, measuring it directly is particularly prone to interference from ambient lighting and various 1/f noise sources. The beam is instead chopped at a frequency of several hundred Hz to shift this signal component away from these competing noise sources. A second lock-in amplifier (L2) connected to the detector output in parallel with the first can then extract this signal using the chopper's reference output. Assuming the detector output is linear in a range of light intensity encompassing both signal components, the ratio of the output from L1 to that from L2 is given by:

$$\Delta I/I(\lambda_o) = \left[-I_o(1-R)^2 x \frac{d\alpha}{d\lambda} e^{-\alpha x} \Delta\lambda \right] [I_o(1-R)^2 e^{-\alpha x}]^{-1} = -x \frac{d\alpha}{d\lambda} \Delta\lambda \quad (4.4)$$

In principle one may divide out the sample thickness x and modulation amplitude $\Delta\lambda$ to obtain $d\alpha/d\lambda$, but for the present purposes it is unnecessary. However, from the standpoint of signal-to-noise ratio these two factors play a significant role. Both enter into the ratio, through the intensity modulation ΔI , which is in general the smaller modulation amplitude and the most susceptible to noise.

Judging by its form given by (4.3), it would seem desirable to increase $\Delta\lambda$ as much as possible to increase the signal-to-noise ratio, but in the present implementation of this scheme it is limited by two things: One is the capability of the opto-mechanical system used to achieve wavelength modulation, which will be discussed in greater detail shortly. The other is the need to limit the size of correction terms of order $\Delta\lambda^3$ and greater in (4.3) which contain higher order wavelength derivatives left out in the truncation in (4.2) [67]. These will become important near the absorption onsets, but may be comparable in size to similar corrections arising from having a finite spectral width $\delta\lambda$ [68, 67]. By keeping $\Delta\lambda \approx \delta\lambda$ it may therefore be possible to mitigate these effects through partial cancellations [67].

The sample thickness comes into play in (4.3) through the factor $x e^{-\alpha x}$, which at the fixed wavelength λ_o is maximum for $x = \alpha^{-1}(\lambda_o)$ (α^{-1} is referred to as the *penetration depth*). α has been measured over a wide range ($\sim 400\text{--}600$ Å interval) near the absorption edges of 4H SiC at room temperature and also tabulated for several common laser wavelengths [16]. Estimates have also been given for the corresponding values at 2 K that take into account the increase in the bandgap from room temperature to 2 K [16]. These may then be used as a rough guide for selecting the sample thickness necessary to maximize the intensity

modulation ΔI . Near the first onset of absorption the general trend is for the absorption coefficient α to increase with decreasing wavelength (increasing energy), and so it becomes necessary to use exceedingly thin samples for measuring the WMA spectrum at photon energies well in excess of the bandgap. Because there are added difficulties in using samples thinner than $\sim 50 \mu\text{m}$, the wavelength region under study in this work has been confined to the first $\sim 300 \text{ meV}$ of the initial onset of absorption ($\hbar\omega = 3.3\text{--}3.6 \text{ eV}$).

4.1.2 Overview of apparatus

The apparatus used for WMA measurements is based on the design given by Shaklee and Rowe [68]. A top-down view of the present system is shown in Figure 10. Wavelength modulation is achieved in the following way: First, light from a 1000 W xenon lamp is focused on the entrance slit of a SPEX 1401 double monochromator (the internal optical components of which are described in detail in Appendix D). Immediately after passing through the entrance slit, the beam is transmitted through a quartz plate that vibrates about an axis normal to the plane of the figure. As a result, the beam is deflected back and forth in the plane of dispersion with a transverse deflection of [69, 67]:

$$w = d \left(1 - \frac{\cos \theta}{\sqrt{n^2 - \sin^2 \theta}} \right) \sin \theta, \quad (4.5)$$

where d is the plate's thickness, n is its refractive index, and θ is its angle of swing relative to when it is normal to the beam (note that this differs from equation (6) in [68]). As the dispersed beam is deflected back and forth by this amount across the exit slit, the wavelength of the light appearing at the monochromator output is modulated by the amount $\lambda - \lambda_0 = Dw$, where D is the linear dispersion of the monochromator. In the present implementation of this mechanism (Electro-Optical Products Corp. SC-25 beam deflector with AGC-110 driver) the plate is driven such that $\theta(t) = \theta_m \sin(2\pi f_\lambda t)$, with the angular amplitude θ_m

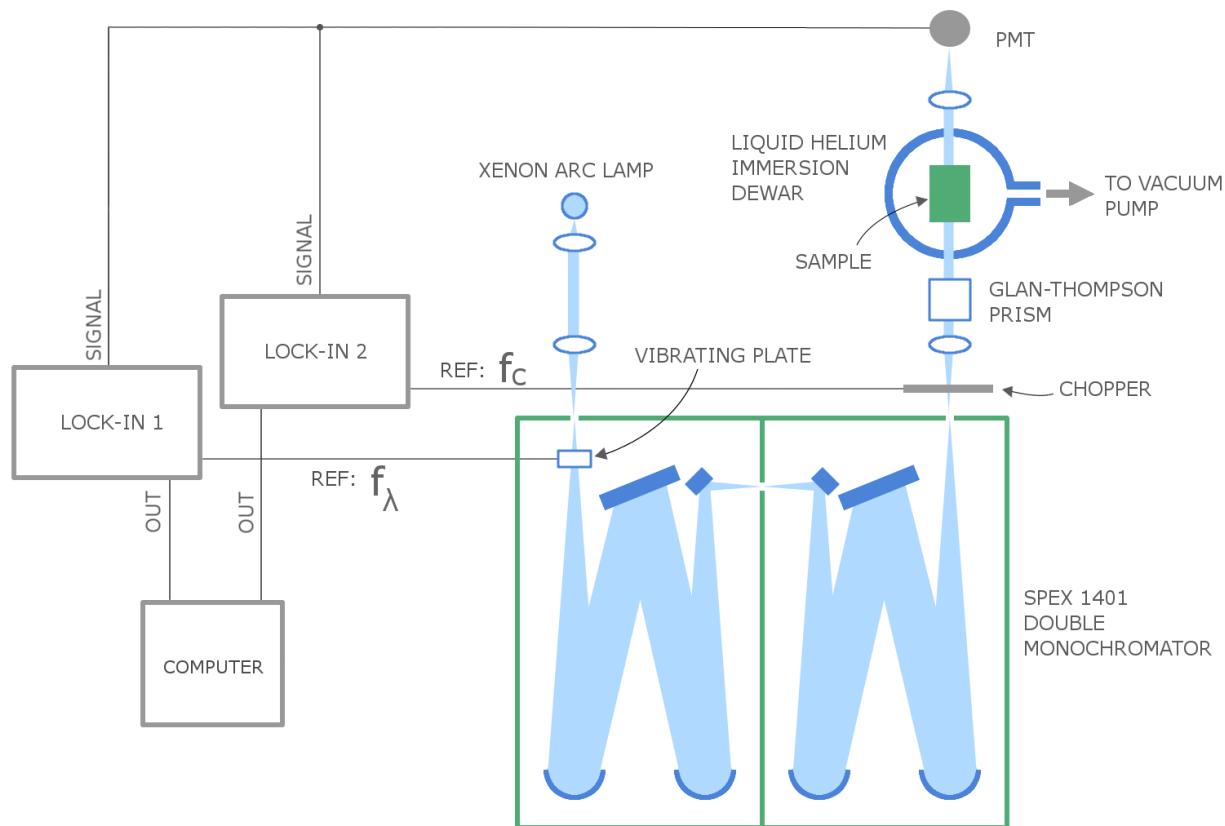


Figure 10: Top-down overview of the experimental apparatus for taking wavelength modulated absorption measurements. Light from a xenon lamp is dispersed by a double monochromator, and the resulting monochromatic beam is directed through a sample inside a pumped liquid helium immersion dewar. The beam is optically chopped at frequency f_c and the wavelength is simultaneously modulated at frequency f_λ by means of a vibrating quartz plate inside the monochromator exit slit. A photomultiplier tube (PMT) detects the transmitted light, and transmits the signal to a pair of lock-in amplifiers for signal averaging. A computer records and processes the demodulated signals from the lock-in amplifiers.

being adjustable between 1 and 15°. Substituting this into (4.5) and multiplying by the dispersion D gives the wavelength λ appearing at the exit slit as a function of time t :

$$\begin{aligned} \lambda(t) - \lambda_o &= Dd \left[\left(1 - \frac{1}{n}\right) \theta + \left(-\frac{1}{6} + \frac{2}{3n} - \frac{1}{2n^3}\right) \theta^3 + \mathcal{O}(\theta^5) \right] \\ &= Dd \left\{ \left[\left(1 - \frac{1}{n}\right) \theta_m + \left(-\frac{1}{8} + \frac{1}{2n} - \frac{3}{8n^3}\right) \theta_m^3 \right] \sin(2\pi f_\lambda t) \right. \\ &\quad \left. + \left(\frac{1}{24} - \frac{1}{6n} + \frac{1}{8n^3}\right) \theta_m^3 \sin(6\pi f_\lambda t) + \mathcal{O}(\theta_m^5) \right\} \end{aligned} \quad (4.6)$$

In the above $\mathcal{O}(\theta_m^n)$ are terms proportional to θ_m^n which are presumed to be negligible. The fact that $\lambda(t)$ contains odd harmonics of the fundamental wavelength modulation frequency f_λ does not pose a significant problem to the measurement since these will likely fall outside the bandwidth of the lock-in referenced to f_λ . However, one must choose a chopping frequency f_c such that it does not overlap with these harmonics.

After emerging through the exit slit, the beam is subsequently chopped and then collimated. Before reaching the sample, the beam passes through a Glan-Thompson prism, where it is linearly polarized with respect to the sample \hat{c} axis. While the sample lies in the path of the beam it is also being suspended inside a liquid helium immersion dewar. The pressure of the liquid helium is reduced using a vacuum pump connected to the dewar's inner reservoir. In its current configuration the pumping system is able to reduce the helium vapor pressure to about 2.0 Torr, corresponding to a temperature of 1.4 K in the reservoir [70]. The dewar has been custom-designed to accommodate the thickest of the samples under study, which is 40 mm long. Because the samples come in a wide array of dimensions, several sample holders have been built specific to one or a few samples. In all cases the samples are held in such a way as to minimize their induced strain as well as to block all light which does not pass through the sample. A selection of a few of these sample holders are shown in Figure 11.

After passing through the sample and the dewar, the beam is finally focused onto a Hamamatsu R955 photomultiplier tube (PMT), which was selected for its high response in the wavelength region of interest. The signal generated by the PMT is then sent to a pair of digital lock-in amplifiers to extract the desired modulation amplitudes. A computer performs the ratio (4.4) numerically from the digital readout of the two lock-in amplifiers and

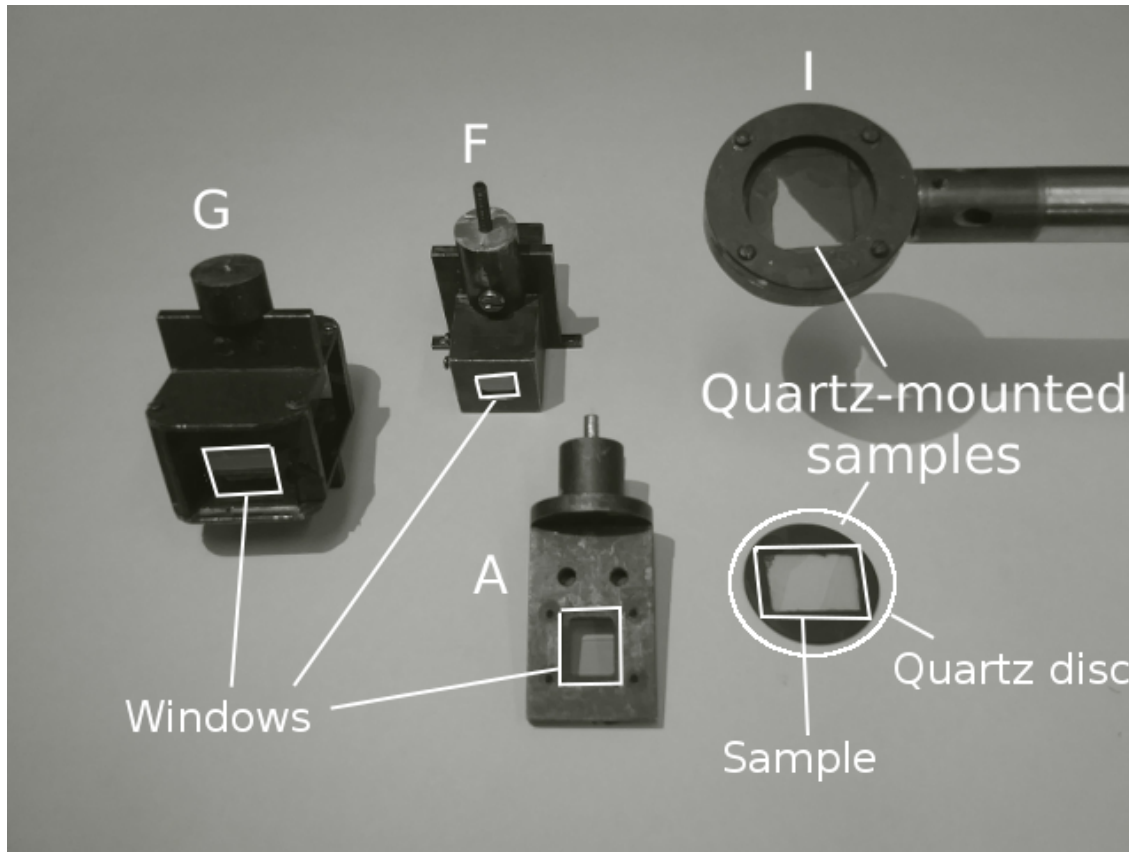


Figure 11: Selection of several different sample holders (denoted A, I, F, and G) used for taking absorption measurements. Sample holders F and G may accommodate samples up to 40 mm in length and $20 \times 20 \text{ mm}^2$ in cross-section. For these two holders, samples are secured in place by nylon set screws along the sides of the sample holders, with felt or blotter paper inserted between the screw tips and sample to minimize strain. Sample holders A and I are used to mount thinner samples ($< 1 \text{ mm}$ thick). A, F, and G each has a single window used to block all portions of the beam passing through the dewar that do not pass through the sample (A has additional holes for fastening parts to the holder, but these may be blocked). Samples are secured to A at one point by Pliobond glue. Sample holder I is used specifically for thin samples mounted to 1 inch diameter quartz discs (described in section 4.3), one of which is shown outside the holder and the other is shown inside the holder. Portions of the quartz discs not covered by the samples are coated with Aquadag. All surfaces of these sample holders are coated with Aquadag to mitigate reflections. Each sample holder may be connected to a stainless steel rod suspended inside the dewar, shown attached to sample holder I.

records the result. The WMA spectrum is built up by successively incrementing the central wavelength λ_o with the rotation of the diffraction gratings and repeating the measurements at each wavelength.

Although in general the system in this work is similar to that used in previous studies [6, 5, 7, 10], a much greater amount of detail has been found in the WMA measurements presented here. This is owed in part to the higher quality samples used, but it is also a result of having performed these measurements at higher spectral resolution. The largest step in this direction came about from the careful re-alignment and focusing procedures described in Appendix D, but also from having installed two 4320 lines/mm holographic gratings in the monochromator, which reduced the spectral width $\delta\lambda$ by nearly a factor of 4 to 0.1 Å (in the original implementation two 1180 lines/mm ruled gratings were installed). This required a number of different measures to be taken in order to compensate for the loss in light throughput, including replacing the originally installed 150 W xenon lamp with a 1000 W xenon lamp and making fine adjustments to the optics both internal and external to the monochromator (see Appendices C and D for discussions of these adjustments).

4.1.3 Double beam configuration

For most of the wavelength region under study (i.e. $\lambda \sim 3000\text{--}4000$ Å), a high power xenon lamp such as the one used in this work is the best suited among other alternatives as a source of spectrally flat white light (see Figure 3 in reference [68]). As stated earlier, in wavelength regions where this is not true, the incident light I_o itself contains spectral features which compete with those due to the sample. In reference to (4.2), this occurs when the percent change in the incident intensity I_o per unit wavelength is approximately:

$$\left| \frac{1}{I_o} \frac{dI_o}{d\lambda} \right| \approx \left| x \frac{d\alpha}{d\lambda} \right|. \quad (4.7)$$

This condition is readily attained for the thinner samples used in this work. In a typical case, we might have $x = 100 \mu\text{m}$, and $d\alpha/d\lambda = 1 \text{ cm}^{-1} \text{Å}^{-1}$ so that $x(d\alpha/d\lambda) = (100 \mu\text{m}) \cdot (1 \text{ cm}^{-1} \text{Å}^{-1}) = .01 \text{ Å}^{-1}$. In this case a mere 1% change in I_o over a 1 Å interval may make

a substantial contribution to the resulting measurement. If we now include this effect in the intensity modulation ΔI , we have from (4.4):

$$\begin{aligned}\Delta I/I &= \left[\frac{dI_o}{d\lambda} (1-R)^2 e^{-\alpha x} - I_o (1-R)^2 x \frac{d\alpha}{d\lambda} e^{-\alpha x} \right] \Delta\lambda [I_o (1-R)^2 e^{-\alpha x}]^{-1} \\ &= \left(\frac{1}{I_o} \frac{dI_o}{d\lambda} - x \frac{d\alpha}{d\lambda} \right) \Delta\lambda\end{aligned}\quad (4.8)$$

In principle one may measure the wavelength dependence of $I_o^{-1}(dI_o/d\lambda)$ and subtract it from all succeeding measurements. However, various experimental errors (instability in the spectral profile of the lamp, instability in the wavelength modulation, and wavelength calibration errors) make it preferable to measure the quantity $I_o^{-1}(dI_o/d\lambda)$ simultaneously with the one given in (4.8). Double beam systems have been proposed [68, 71] in which part of the incident light is picked off by a beam splitter before reaching the sample, and from there it is directed to a secondary detector for measuring $I_o^{-1}(dI_o/d\lambda)$. A schematically simpler method has been tried for this work and will be outlined here. The basic configuration is shown in Figure 12. The method used here also relies on the separation of the beam into two parts, which in this case occurs between the entry window of the sample dewar and any other optical components lying along the beam's path leading up to the dewar. For this a quartz beam splitter is used at 45° incidence, directing a portion of the beam to a second photomultiplier (PMT 2) of the same type (Hamamatsu R955) as the one beyond the sample (PMT 1). In the same manner as before, the signal from PMT 2 is fed into a second pair of lock-in amplifiers (L3 and L4) which are referenced to either the wavelength modulation frequency f_λ or chopping frequency f_c . The ratio is similarly taken of the demodulated signal from L3 to that from L4, which gives:

$$\Delta I_2/I_2(\lambda_o) = \frac{d}{d\lambda} (\gamma_2 R_{BS} I_o) \Delta\lambda (\gamma_2 R_{BS} I_o)^{-1} = \left(\frac{1}{\gamma_2} \frac{d\gamma_2}{d\lambda} + \frac{1}{R_{BS}} \frac{dR_{BS}}{d\lambda} + \frac{1}{I_o} \frac{dI_o}{d\lambda} \right) \Delta\lambda, \quad (4.9)$$

where γ_2 is the responsivity of PMT 2 and R_{BS} is the reflectivity of the beam splitter at 45° incidence. An additional term proportional to $T_{BS}^{-1}(dT_{BS}/d\lambda)$ will also be incorporated into the signal from PMT 1, where T_{BS} is the beam splitter's transmittance at 45° incidence. At this point it might also be appropriate to restore those contributions due to the sample reflectivity R and responsivity γ_1 of PMT 1 that were neglected earlier. However, if each of

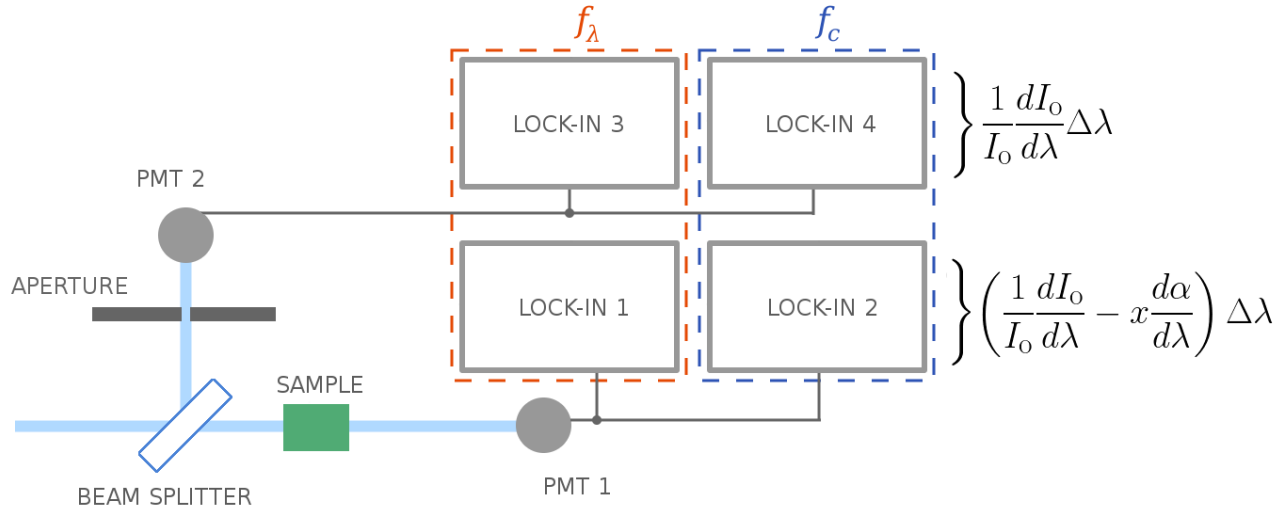


Figure 12: Double beam configuration for extracting the wavelength variation of the incident light I_o from the WMA spectrum of the sample. A beam splitter is used to pick off part of the beam and direct it to a secondary photomultiplier, PMT 2. Lock-in amplifiers 3 and 4 extract the signal modulations from PMT 2 at frequencies f_λ and f_c in the same manner as lock-in amplifiers 1 and 2 do for the signal from PMT 1. The quantity $I_o^{-1}(dI_o/d\lambda)$ obtained from lock-in amplifiers 3 and 4 may then be numerically subtracted from that obtained by lock-in amplifiers 1 and 2 to give the remaining component containing $d\alpha/d\lambda$ which is due to the sample. The aperture is put in place to prevent saturation of PMT 2.

these terms can be neglected then the ratio of the demodulated signals from L3 and L4 is just the quantity $I_o^{-1}(dI_o/d\lambda)\Delta\lambda$ that also appears as a background in the ratio obtained from L1 and L2 (see (4.8)). The two ratios and the subtraction of the background are performed numerically using the digital readouts of the lock-in amplifiers. The aperture in Figure 12 is used to limit the light reaching PMT 2 to a level at which the detector is linear, which is necessary to properly take the prescribed ratio (it is presumed the sample attenuates the beam adequately to prevent saturation of PMT 1). An example of this being done for the measured WMA spectrum of a 50 μm 4H SiC boule is shown in Figure 13.

In the example shown the two large features seen in the WMA measurements of the sample are almost entirely due to the wavelength variation of the incident light, and it is seen that they both may be almost entirely eliminated in taking the difference of the derivative spectra recorded from the two beams. As the quantity $x(d\alpha/d\lambda)$ grows smaller with decreasing sample thickness, it is expected that the terms neglected earlier (i.e. R , R_{BS} , γ_1 , γ_2 , etc.) become important and the method is no longer adequate. A systematic study of these effects has not been conducted at this time, and so for the time being these measurements have been limited to samples thicker than $\sim 50 \mu\text{m}$. As mentioned earlier, this sets a lower bound on the wavelength region over which these measurements may be performed.

4.2 LOW TEMPERATURE PHOTOLUMINESCENCE

Compared to the WMA measurement, the LTPL measurements used here are a relatively straightforward method for directly recording the emission spectrum from a given sample. A top-down overview of the apparatus is shown in Figure 14. In this case excitation is provided to the sample by means of a laser, which is usually focused to a < 1 mm diameter spot on the sample surface. Here the sample is also suspended in a liquid helium immersion dewar, and the pumping system is sufficient to maintain the helium bath temperature at 2 K. The photoluminescence is collected from the sample and thereafter focused onto the entrance slit of a Fast-Fastie type, asymmetric Czerny-Turner spectrometer. In most cases

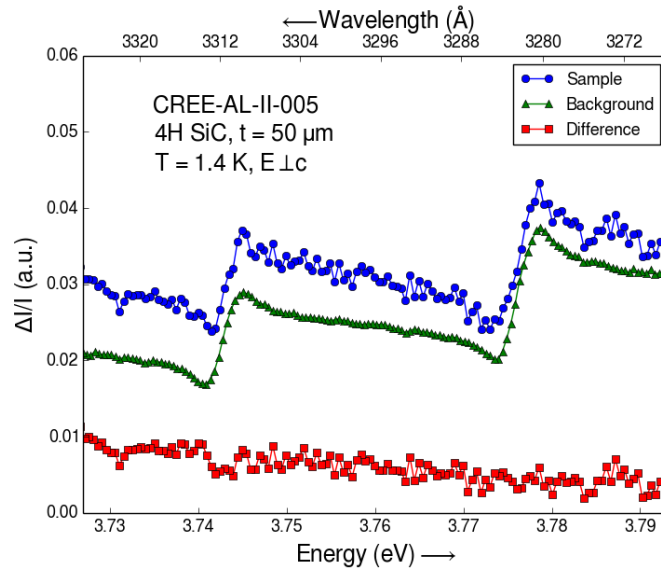


Figure 13: Double beam method applied to the wavelength modulated absorption spectrum of a 50 μm thick 4H SiC boule slice (blue circles). The derivative spectrum of the incident light (green triangles) is directly subtracted from the sample spectrum in which it appears as a background, eliminating the strong features due to the wavelength variation of the incident light (difference shown as red squares).

an entrance slit width of 100 μm was used. The diffraction grating installed in all cases was a 1800 lines/mm ruled grating blazed for operation at $\sim 4000 \text{ \AA}$. For the given slit width, the wavelength resolution of the instrument is $\sim 0.7 \text{ \AA}$. A liquid nitrogen-cooled CCD array placed at the focal plane of the spectrometer records the photoluminescence spectrum over a wavelength range about 100 \AA wide. In order to examine the polarization dependence of the photoluminescence, a Glan-Taylor prism is placed in the collimated part of the beam leaving the sample dewar.

Because the LTPL spectra are recorded with respect to *emission* wavelength, the wavelength λ_{ex} of the exciting radiation is of secondary concern. However, there still remain two important criteria for the selection of the laser to be used. Since the interest here is in free exciton recombination radiation, it is necessary for the photons incident on the sample to have enough energy to create those excitons in the first place. The minimum threshold for this to occur is just the lowest energy indirect absorption onset $\hbar\omega = E_{gx} + \hbar\Omega_o$, where $\hbar\Omega_o$ is the lowest of the principal phonon energies. In contrast to the WMA measurements, there is no need in this case to have the light penetrate through the sample, and so it is desirable also to choose the excitation wavelength such that the penetration depth $\alpha^{-1}(\lambda_{ex})$ is a few times smaller than the sample thickness. This becomes even more critical for those samples consisting of a high purity epitaxial layer grown on a heavily doped substrate, where it is necessary to avoid photoluminescence from nitrogen-bound excitons, which overlaps with the free exciton photoluminescence in the LTPL spectrum. Most epi-layer samples were thick enough that an excitation wavelength $\lambda_{ex} = 3550 \text{ \AA}$ was used (Coherent model Genesis CX 355), for which the corresponding penetration depth is $\alpha^{-1} = 64 \mu\text{m}$ [16].

Two different sample configurations are used here to measure the LTPL spectrum for both polarizations conveniently ($\mathbf{E} \parallel \hat{c}$ and $\mathbf{E} \perp \hat{c}$), depending on how the \hat{c} axis is oriented relative to the illuminated surface. These will be referred to as the *glancing angle* and *right angle* geometries, which are pictured in Figure 15. In both cases pictured the laser beam propagates along the $-x$ direction and the LTPL propagates along the $+y$ direction. In the glancing angle geometry the sample's surface normal lies in between the $+x$ and $+y$ directions, and so the LTPL may be collected from the same face as that which the laser illuminates. Despite the laser beam's low angle to the sample surface, it may still refract

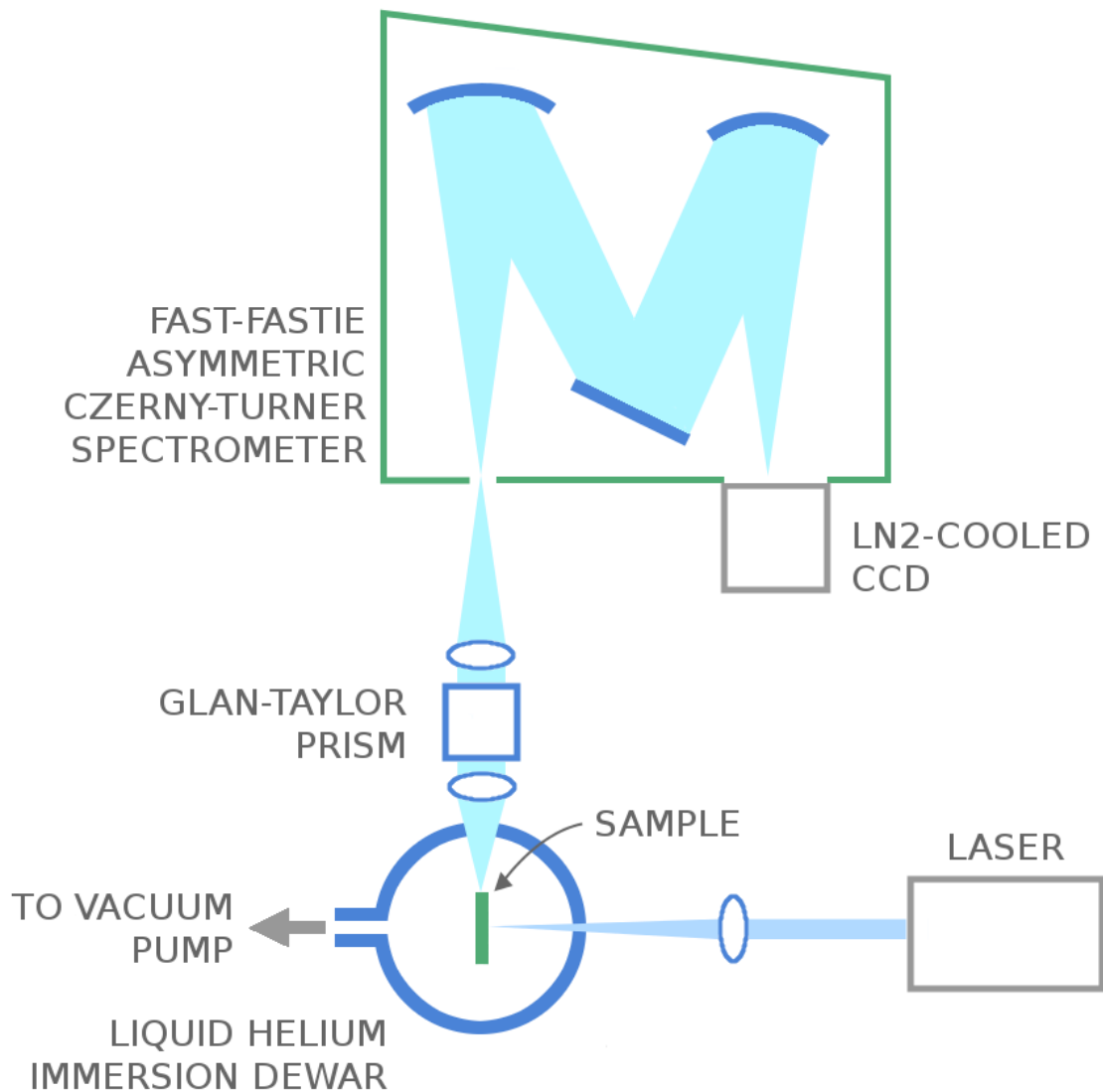


Figure 14: Overview of apparatus for low temperature photoluminescence measurements. A laser is used to excite a sample inside a pumped, liquid helium immersion dewar, and the emerging photoluminescence is focused onto the entrance slit of an Fast-Fastie type, asymmetric Czerny-Turner spectrometer. If necessary the photoluminescence is also polarized using a Glan-Taylor prism. A liquid nitrogen cooled CCD array detects the photoluminescence spectrum at the focal plane of the spectrometer.

into the sample nearly along the surface normal due to the sample's high refractive index (~ 3) [72]. In the right angle geometry the surface normal points in the $+x$ direction, and so the LTPL must be collected from the edge facing towards $+y$.

Since the LTPL propagating along $+y$ may be polarized either along x or z , the sample must be mounted such that its \hat{c} axis aligns closely with either of these two axes. In this work the samples used for LTPL measurements came in two varieties: boule material or epitaxially grown films (epi-layers). The boule material was cut from larger slabs such that their \hat{c} axes lied within the plane of their cross-sections (this is necessary for performing WMA measurements for both $\mathbf{E} \parallel \hat{c}$ and $\mathbf{E} \perp \hat{c}$), and the epi-layers all had their \hat{c} axes normal to their cross-sections (off-axis angles of a few degrees or less between the \hat{c} axis and the surface normal were assumed to be negligible). The boule samples could therefore be oriented in either of the two geometries as long as their \hat{c} axes pointed along the z direction. However, to study both polarizations, the epi-layers could only be oriented according to the right angle geometry, with their \hat{c} axis (and surface normal) pointed along the x direction and toward the laser.

One last consideration is the adjustment of the excitation intensity. Aside from increasing the overall LTPL intensity, it has been observed in this work and by others [60, 61] to have a marked effect on the linewidth of the free exciton recombination radiation. In order to facilitate the identification of all peaks in the LTPL spectrum, it is therefore necessary to lower the excitation intensity as much as practically possible in order to reduce the overlap between one or more closely spaced features. Figure 16 shows the normalized 76.1 meV phonon-assisted free exciton emission line for a 120 μm thick free-standing (substrate removed) 4H SiC epi-layer at various power settings of the laser ($\lambda_{ex} = 3550 \text{ \AA}$). Intentionally elevating the sample temperature by increasing the excitation power may also serve to promote recombination from various excited states of the exciton. This has not been attempted in any systematic way here, although a few cursory results will be touched upon later. Additional factors which may likely influence the linewidth are the sample's thermal conductivity, the size of the excitation volume, and the amount of energy imparted by each photon in excess of the lowest absorption threshold, but these have not been explored here.

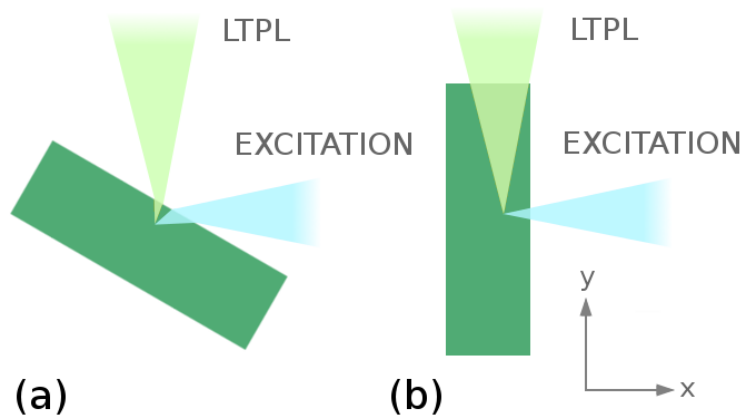


Figure 15: Two different geometries used for conducting low temperature photoluminescence (LTPL) measurements. (a) In the glancing angle geometry the excitation is directed towards the sample at a low angle to the sample surface, and the LTPL is collected from the same surface. Note that the beam labeled LTPL *does not* represent the specular reflection from the surface, which is not shown in this figure. (b) In the right angle geometry the excitation is incident on the larger sample face and the LTPL is collected through the sample's edge at a right angle to the exciting beam.

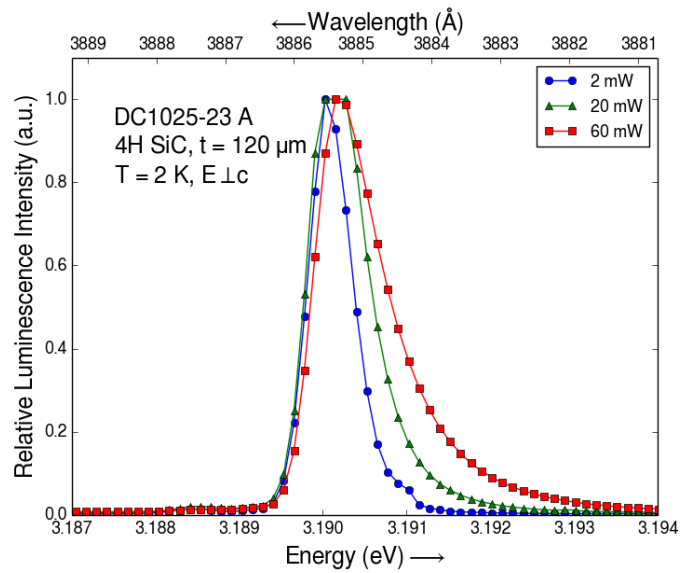


Figure 16: Normalized 76.1 meV phonon-assisted free exciton emission line at three different power settings of the laser used for excitation ($\lambda_{ex} = 3550 \text{ \AA}$). With increasing power the effective temperature of the free exciton gas increases as well, resulting in an elongated high energy tail.

4.3 SAMPLE PREPARATION

For the WMA measurements it is important to have a variety of sample thicknesses in order to effectively cover a wide range of the spectrum as discussed above. To this end the primary samples used here for WMA measurements were sectioned from two 4 cm diameter boules using a diamond saw blade. Each section so obtained would be left with two faces at least $1 \times 1 \text{ cm}^2$ in cross-section to be polished to an optical grade finish. These would then serve as the windows through which the light would pass during the measurement. In order for the light to be polarized either $\mathbf{E} \parallel \hat{c}$ or $\mathbf{E} \perp \hat{c}$ it is necessary to ensure that the sample's \hat{c} axis lies in the plane of these faces. For this reason the first small slab that is removed from the boule is taken for transmission Laue measurements [73] to determine its crystallographic orientation. By comparing the resulting diffraction pattern to reference Laue patterns for 4H SiC [74], the orientation of the \hat{c} axis and the crystallographic planes in the boule are determined. As a standard, all following saw cuts are made such that the resulting sample windows correspond to the $\{11\bar{2}0\}$ planes and the \hat{c} axis lies parallel with one of the edges for convenient alignment of the sample.

Once the samples have been cut out, their window faces are ground down to the desired thickness using a lapping wheel and diamond grit paste. This occurs in stages of successively smaller grit sizes, with the final finish being obtained using $0.25 \mu\text{m}$ diamond grit. The final optical finish is checked for scratches and surface roughness using an interferometer (Zygo NewView 600). This is done primarily to reduce scattering of the light at the sample surfaces. To prevent cracking the thinnest samples ($\sim 50 \mu\text{m}$) during or after the polishing procedure, these are glued to a $\sim 1 \text{ mm}$ thick plate of fused silica before becoming thin enough to easily crack ($\sim 100 \mu\text{m}$). The glue that is used withstands liquid helium temperatures and is also highly transmissive down to about 3000 \AA (Norland Products NOA 88). Once the glue has cured, the exposed side of the sample may then be ground down to the desired thickness. The induced stress of the glue on the sample at low temperature is not currently known, although so far there is no evidence to suggest that it alters the sample's absorption spectrum in any way compared to samples that aren't glued down.

Samples this thin and slightly thicker may exhibit thin film interference. This manifests

itself in the WMA spectrum as a near-sinusoidal oscillation of period $\delta\lambda \approx \lambda^2/nx$ which results from the phase $2nx/\lambda$ acquired by the beam undergoing two internal reflections, where x is the sample thickness and n is the refractive index in the measured wavelength interval. As the wavelength λ changes from one part of the spectrum to the other, the transmission through the sample is modulated by the accompanying change in this phase. The oscillations may be easily identified if the refractive index and sample thickness are known to reasonable accuracy, but it may in some cases totally obscure those features related to small changes in the absorption coefficient. An attempt has been made to mitigate this effect by inducing an intentional slope in one sample face relative to the other, as in Figure 17. This is done through uneven application of the wax that is used to attach the sample to the polishing assembly (if the sample is mounted to a fused silica plate, the wax is applied to the back surface of the plate). Now the relative phase between the beam passing straight through the sample with the one that undergoes two internal reflections varies over the surface and along the gradient of the slope. The result is a series of dark and bright bands across the illuminated portion of the sample, and if enough of these are present it is presumed their effect will be reduced in the average intensity seen by the detector:

$$I = \frac{1}{S} \int dS I_o T. \quad (4.10)$$

Here S is the illuminated area of the sample and T is the transmittance of the sample with account made for thin film interference. It has been found empirically that a 20 μm thickness variation over a $1 \times 1 \text{ cm}^2$ cross-section is sufficient to eliminate fringes in samples nominally 100 μm thick. In Figure 18 is shown a comparison of the WMA spectra obtained from two samples from the same 130 μm epi-layer: one with a 2 μm slope and the other with a 20 μm slope. The oscillations are seen to be entirely eliminated from the WMA spectrum of the latter, and the remaining structure may be attributed predominantly to the wavelength dependence of the absorption coefficient.

While this has ostensibly cured the problem of interference effects, this method brings additional difficulties along with it. Given that the sample no longer has a well-defined thickness, the ratio taken in expression (4.4) will no longer reduce simply to the desired term $-x(d\alpha/d\lambda)\Delta\lambda$. Furthermore, any variation in I_o over the sample's cross-section gets

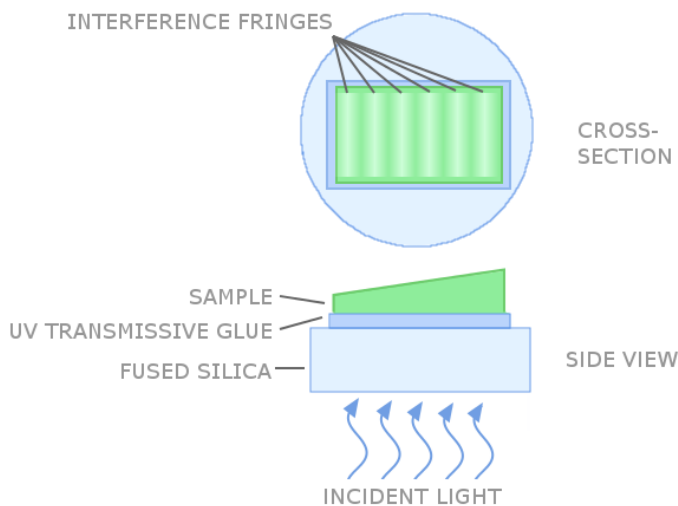


Figure 17: An intentional slant is introduced in one face of a thin sample relative to the other in order to reduce the importance of thin film interference in the absorption spectrum. The sample is shown mounted to a fused silica plate with UV transmissive glue, and exhibits a graded thickness profile induced during the polishing process. When a monochromatic beam passes through its cross-section, a series of interference fringes is observed aligned perpendicular to the gradient of the sloped surface. If the sample faces were perfectly parallel, the intensity profile over the sample cross-section would vary uniformly between constructive and destructive interference as the wavelength of the incident beam is varied over the absorption spectrum, resulting in unwanted oscillations in the spectrum. With a sloped surface, the detector sees the average transmitted intensity over several interference fringes at once, which may to some extent reduce the amplitude of the oscillations due to thin film interference.

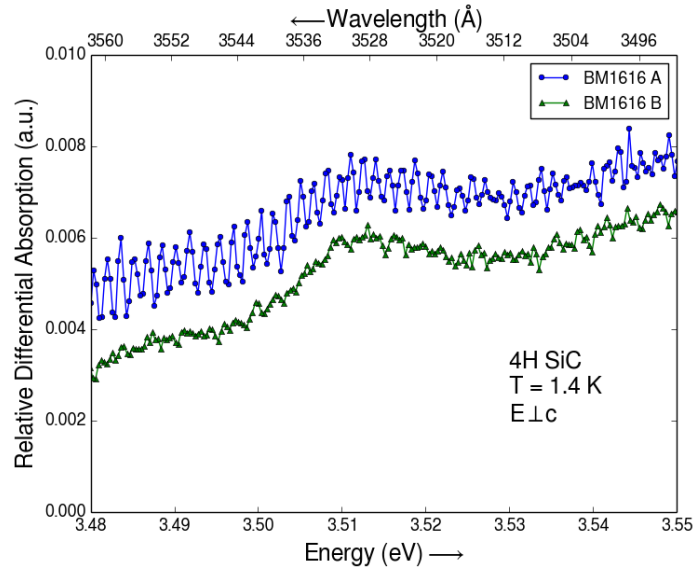


Figure 18: WMA spectra for two samples from the same 130 μm epi-layer. Sample BM1616 A has been polished with a 2 μm slope over its $1 \times 1 \text{ cm}^2$ cross-section and BM1616 B has been polished with a 20 μm slope over the same cross-sectional area. The greater slope for sample BM1616 B is seen to totally eliminate the interference fringes seen in the spectrum of its partner sample.

mixed with the thickness variation in the average (4.10) in such a way that it cannot be canceled out by taking the above ratio. Note that for a perfectly uniform sample thickness, the transmittance T may be taken out of the integral over the sample cross-section, and by taking the ratio as in (4.4) the intensity of the incident light is canceled out whether it is uniform or not (assuming its wavelength derivative may be neglected):

$$\begin{aligned}
\frac{1}{I} \frac{dI}{d\lambda} &= \left(\frac{1}{S} \int dS I_o T \right)^{-1} \frac{d}{d\lambda} \left(\frac{1}{S} \int dS I_o T \right) \\
&= \left(\frac{T}{S} \int dS I_o \right)^{-1} \frac{d}{d\lambda} \left(\frac{T}{S} \int dS I_o \right) \\
&= \left(\frac{1}{S} \int dS I_o \right)^{-1} \left(\frac{1}{S} \int dS I_o \right) \frac{1}{T} \frac{dT}{d\lambda} \\
&= \frac{1}{T} \frac{dT}{d\lambda}.
\end{aligned} \tag{4.11}$$

Otherwise, beam non-uniformity is very likely to be a problem since the xenon lamp used as the source in the WMA measurements is known to exhibit significant spatial and temporal intensity variations. An alternative might be to retain the parallelism of the sample's faces but use transparent coatings to reduce the large mismatch in refractive index between the sample and the liquid helium, thereby reducing the proportion of internally reflected light. At present this has not been explored.

For the epi-layer samples used in this work, the individual samples were usually cleaved from a larger wafer. While their surfaces were generally polished to begin with, their heavily doped substrates needed to be ground off before performing absorption measurements. Unlike the boule material, the resulting window surfaces were all normal to the \hat{c} axis, and so absorption measurements could only be done for $\mathbf{E} \perp \hat{c}$. In any case, the epi-layers were selected primarily for use in LTPL measurements, for which both polarizations could be obtained with the right angle configuration described above. For the LTPL measurements it was unnecessary to remove the substrates if the excitation could be confined to the epi-layer only, although in some cases this was done to verify that this was so.

5.0 RESULTS AND DISCUSSION

5.1 DATA ANALYSIS AND FITTING

In the wavelength modulated absorption (WMA) and low temperature photoluminescence (LTPL) spectra the emission lines at the photon energies $\hbar\omega^{(e)}$ and absorption onsets at $\hbar\omega^{(a)}$ are to be measured and compared with each other. In order to do this precisely and accurately, these quantities are used as fitting parameters in the functions to be described presently. For the absorption onsets in the WMA spectrum, the data are fitted to functions of the following form [38, 67, 68]:

$$F(w) = \frac{\sqrt{\sqrt{w^2 + 1} + w}}{\sqrt{w^2 + 1}}, \quad (5.1)$$

with $w = (\hbar\omega - \hbar\omega^{(a)})/\eta$. This has the form of the expected inverse-square-root onset at $\hbar\omega = \hbar\omega^{(a)}$ but with an additional parameter η included to account for broadening (see Figure 19). It is seen that in addition to broadening the feature, increasing η will shift the position of the function's maximum away from $\hbar\omega^{(a)}$ and to higher energies (by an amount $\eta/\sqrt{3}$).

Strictly speaking, the parameter η has been introduced to account phenomenologically for the finite lifetime and accompanying energy uncertainty of the state to which the transition is occurring [38, 75]. For the absorption onsets shown in figures 21 and 22 the obtained value of η is generally found to be limited by the energy resolution of the monochromator, which was usually set to 0.1–0.3 meV. As such, the function $F(w)$ should also be convolved

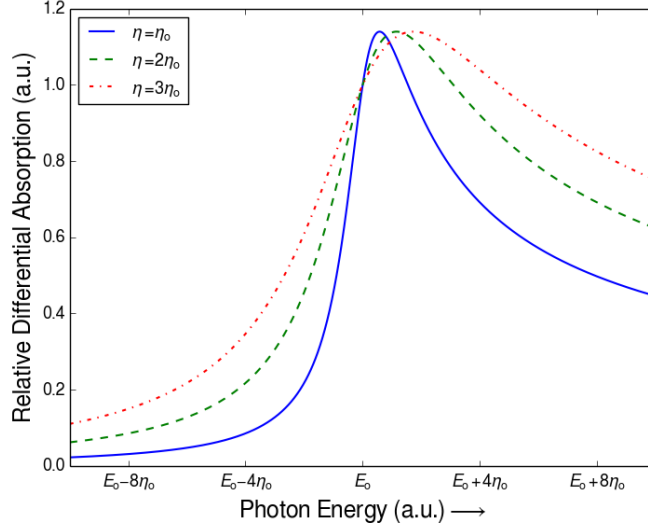


Figure 19: Function $F(w) = (w^2 + 1)^{-1/2} \sqrt{\sqrt{w^2 + 1} + w}$ used to fit to absorption onsets in wavelength modulated absorption measurements, where $w = (\hbar\omega - \hbar\omega^{(a)})/\eta$, $\hbar\omega$ is the photon energy at each point in the measured data series, and $\hbar\omega^{(a)}$ and η are fitting parameters. For a given indirect transition, $\hbar\omega^{(a)}$ corresponds to the photon energy precisely at the absorption onset $\hbar\omega = E_{gx} + \hbar\Omega$, where E_{gx} is the exciton ground state in question and $\hbar\Omega$ is the energy of the phonon participating in the indirect transition. The parameter η accounts for broadening of the expected inverse-square-root-shaped onsets of the form (4.1) (note that the factor $(\hbar\omega)^2$ in (4.1) is assumed to be constant in the near-vicinity of the onset). This latter parameter is adjusted between the three curves shown.

with the transfer function of the monochromator [68]:

$$H(\lambda) = \begin{cases} 1/\delta\lambda - |\lambda - \lambda_o|/\delta\lambda^2 & |\lambda - \lambda_o| < \delta\lambda \\ 0 & |\lambda - \lambda_o| \geq \delta\lambda \end{cases} \quad (5.2)$$

$\delta\lambda$ and λ_o here are, respectively, the wavelength resolution of the monochromator and the central wavelength of the light emerging from the exit slit. In several other cases, however, the absorption onsets exhibited broadening greatly exceeding that of the instrument resolution ($\eta > 1$ meV). In order to reduce the complexity of the fitting procedure, the function $F(w)$ was therefore left as is and the broadening was accounted for by the parameter η alone. Fits were in general applied to smaller intervals within a given data set which contained one or more reasonably isolated absorption onsets, with the overall function having the form:

$$f_a(\hbar\omega) = \sum_i A_i F((\hbar\omega - \hbar\omega_i^{(a)})/\eta_i) + B\hbar\omega + C, \quad (5.3)$$

where the parameters A_i are simply multiplicative scaling factors, and the terms $B\hbar\omega + C$ allow for the possibility that the onsets overlap with a slowly varying background.

For the LTPL spectrum the functional form used for fitting was one of two, depending on whether or not the emission line was due to a free or bound exciton. It was assumed that the temperature was low enough that the free exciton emission lines originated from an exciton lying very near to the lowest exciton band minimum (assumed to be parabolic in this region). For this case the emission line should have the shape described by (3.38) and realized experimentally in Figure 16. It was found necessary to also convolve this function with the monochromator transfer function (5.2) since for the LTPL measurements the resolution $\delta\lambda$ was generally 0.7 \AA ($\delta E = 0.5\text{--}0.6$ meV) or more. Furthermore, the line broadening due to the Boltzmann factor could not effectively model the instrumental broadening at the low energy side of the emission lines, which is near to the location of $\hbar\omega^{(e)}$. To reduce computation

time, the energy resolution δE was calculated from the slit setting of the spectrometer and treated as a fixed parameter. The resulting function has the form:

$$\begin{aligned}
I_{fe}(\hbar\omega, A, \hbar\omega^{(e)}, kT) &= \frac{A}{\varepsilon} \left\{ \frac{1}{\varepsilon} [2g_1(x) - g_1(x - \varepsilon) - g_1(x + \varepsilon)] \right. \\
&\quad \left. + [g_2(x + \varepsilon) - g_2(x - \varepsilon)] + \frac{x}{\varepsilon} [g_2(x + \varepsilon) + g_2(x - \varepsilon) - 2g_2(x)] \right\} \\
g_1(x) &= \sqrt{2e} \left[-e^{-x} \sqrt{x} \left(\frac{3}{2} + x \right) + \frac{3}{4} \sqrt{\pi} \operatorname{erf}(\sqrt{x}) \right] \\
g_2(x) &= \sqrt{2e} \left(-e^{-x} \sqrt{x} + \frac{1}{2} \sqrt{\pi} \operatorname{erf}(\sqrt{x}) \right) \\
\operatorname{erf}(x) &= \frac{2}{\sqrt{\pi}} \int_0^x dt e^{-t^2} \\
x &= \frac{\hbar\omega - \hbar\omega^{(e)}}{kT} \\
\varepsilon &= \frac{kT}{\delta E}
\end{aligned} \tag{5.4}$$

The free parameters here are A , $\hbar\omega^{(e)}$, and kT ; and \sqrt{x} is taken to be zero for $x < 0$.

Fitting to the nitrogen-bound exciton emission lines, while not of primary interest, was needed in cases where these overlapped strongly with free exciton emission lines. Slight asymmetries in bound exciton phonon replicas have been discussed in reference [66] for example, but for the present case they were assumed to have the form of a Gaussian convolved with the triangular transfer function:

$$\begin{aligned}
I_{be}(\hbar\omega, B, \hbar\omega^{(e)}, \sigma) &= \frac{B}{2\zeta^2} \left\{ \left[-2e^{-x^2} + e^{-(x-\zeta)^2} + e^{-(x+\zeta)^2} \right] \right. \\
&\quad \left. - \sqrt{\pi} x [2 \operatorname{erf}(x) + \operatorname{erf}(\zeta - x) - \operatorname{erf}(x + \zeta)] \right. \\
&\quad \left. + \sqrt{\pi} \zeta [\operatorname{erf}(\zeta - x) + \operatorname{erf}(x + \zeta)] \right\} \\
x &= \frac{\hbar\omega - \hbar\omega^{(e)}}{\sqrt{2}\sigma} \\
\zeta &= \frac{\delta E}{\sqrt{2}\sigma},
\end{aligned} \tag{5.5}$$

where B and σ are proportional to the height and width of the peak, which is centered at $\hbar\omega^{(e)}$. As with the fits to the absorption data, a general fit was applied to smaller segments of the data which contained isolated clusters of one or more peaks:

$$f_e(\hbar\omega) = \sum_i I_{fe}(\hbar\omega, A_i, \hbar\omega_i^{(e)}, kT_i) + \sum_j I_{be}(\hbar\omega, B_j, \hbar\omega_j^{(e)}, \sigma_j) + C, \tag{5.6}$$

where the sum i runs over all peaks identified as due to free excitons and the sum j runs over all peaks due to bound excitons. C is an additional parameter meant to account for any constant offset in the data. The fitting method is a nonlinear least-squares algorithm with bounded parameters. It is implemented using the `curve_fit` function from the SciPy Python module [76], which is based on the algorithm described in [77]. As an example, the function $f_a(\hbar\omega)$ (5.3) fit to a cluster of three absorption onsets is shown in Figure 20. The numbers displayed above each onset are the onset energies $\hbar\omega^{(a)}$ for each peak, and it is seen that each is offset by a small amount on the low-energy side of the maximum of the corresponding peak, as described earlier. In most cases this results in an offset of 0.1–0.2 meV. Once the values for the parameters have been obtained from the fitting algorithm, the confidence interval on each of these values can be obtained by various Monte Carlo methods [78]. This was generally performed by adding to the fitted function randomly generated (and normally distributed) noise at a level comparable to that present in the original data and repeating the fitting algorithm for this simulated data set 100 times. The confidence intervals on the energy positions of the absorption onsets and emission lines were nearly always smaller than 0.1 meV in width. This is comparable to or less than the precision and accuracy of the wavelength calibration for either the LTPL measurements or the WMA measurements, although for some of the broader absorption onsets ($\eta > 1$ meV) the error estimates in the fitted energies could exceed this somewhat.

5.2 OVERVIEW OF WMA AND LTPL MEASUREMENTS

An overview of the wavelength modulated absorption measurements within the first ~ 80 meV of the fundamental absorption edge in 4H SiC is shown in Figures 21 and 22 for $\mathbf{E} \parallel \hat{c}$ and $\mathbf{E} \perp \hat{c}$, respectively. Both spectra are composites of several measurements over smaller wavelength intervals, with the measured sample in each interval chosen such that its thickness closely matched the penetration depth α^{-1} in that interval. For the wavelength range shown in the two figures, the samples were usually sectioned from either of two 4 cm diameter boules (with nitrogen concentration $\approx 10^{15} \text{ cm}^{-3}$), with thicknesses ranging between about 1

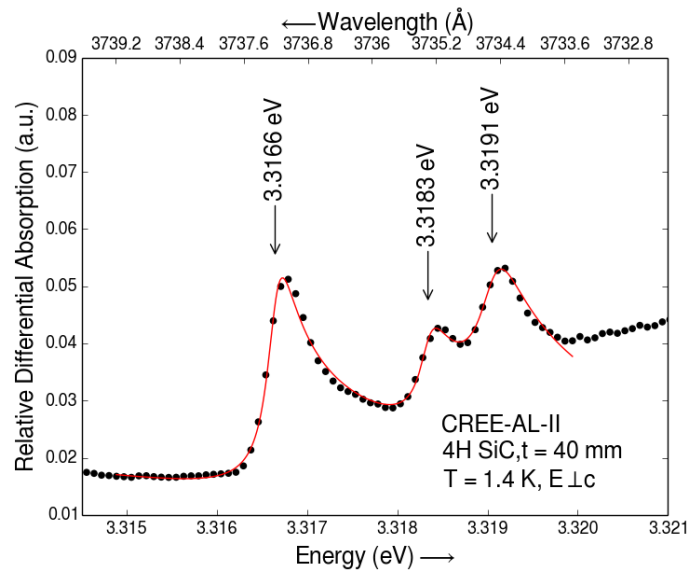


Figure 20: Example of fit (red line) to low temperature wavelength modulated absorption data (filled circles). The numbers labeling each peak are the energies of the onsets as obtained from the fitting procedure. Note that each one is slightly offset towards the low energy side of the maximum of each peak.

mm to 4 cm. Because the measurements are proportional to both the wavelength derivative of the absorption coefficient $d\alpha/d\lambda$ and the sample thickness x , the data in each interval have been uniformly scaled so as to obtain an unbroken curve. The data are plotted versus the photon energy of the incident light so that the left sides of the figures correspond to that part of the spectrum where the sample is (ideally) totally transparent. As the photon energy is increased to the right, a series of abrupt absorption onsets of the form (4.1) is observed.

These onsets most often occur in pairs, with the two peaks in a given pair separated by roughly 7 meV. This separation is in good agreement with the calculated spin-orbit splitting $\Delta_{so} = 8.6$ meV between the top two valence band maxima [13, 14], and so each pair is associated with an indirect transition involving a particular momentum-conserving principal phonon to either the lowest-lying exciton, EX_1 or the spin-orbit split-off exciton, EX_{so} (the measured separation should actually be different than Δ_{so} to account for the excitonic effects discussed later in section 5.4). In the figures, the pairs are marked by brackets and the energies of the assigned phonons in meV. The lower energy onset of a given pair is associated with EX_1 and the higher energy onset is associated with EX_{so} (in some cases one of these overlaps with a stronger onset, and is not observed).

Note that there is a clear difference between the absorption spectrum for light polarized $\mathbf{E} \parallel \hat{c}$ and that for light polarized $\mathbf{E} \perp \hat{c}$. In particular, each principal phonon participates in only one polarization. This stands in good agreement with the earlier given group theory analysis without spin, assuming the phonons that participate for $\mathbf{E} \parallel \hat{c}$ have symmetry M_1 and M_3 and those with symmetry M_2 and M_4 participate for $\mathbf{E} \perp \hat{c}$. Serrano *et al.* have calculated the principal phonon energies along with their corresponding symmetry representations [79], and by comparing these with the phonon energies measured here it does appear that these selection rules hold true (see Table 5 in section 5.4). However, it is worth mentioning that while there is general agreement in the literature with regard to the energies of the principal phonons, there are often discrepancies between them for the higher energy phonons. Most calculations of phonon dispersion relations (which relate phonon energy to wavevector) show a distinct energy gap between the lower, “acoustic” phonon branches and the upper “optic” branches [79, 80, 81, 49, 82] (the lower branches originate through zone folding of the acoustic branches in 3C SiC, and the upper branches originate from the optic

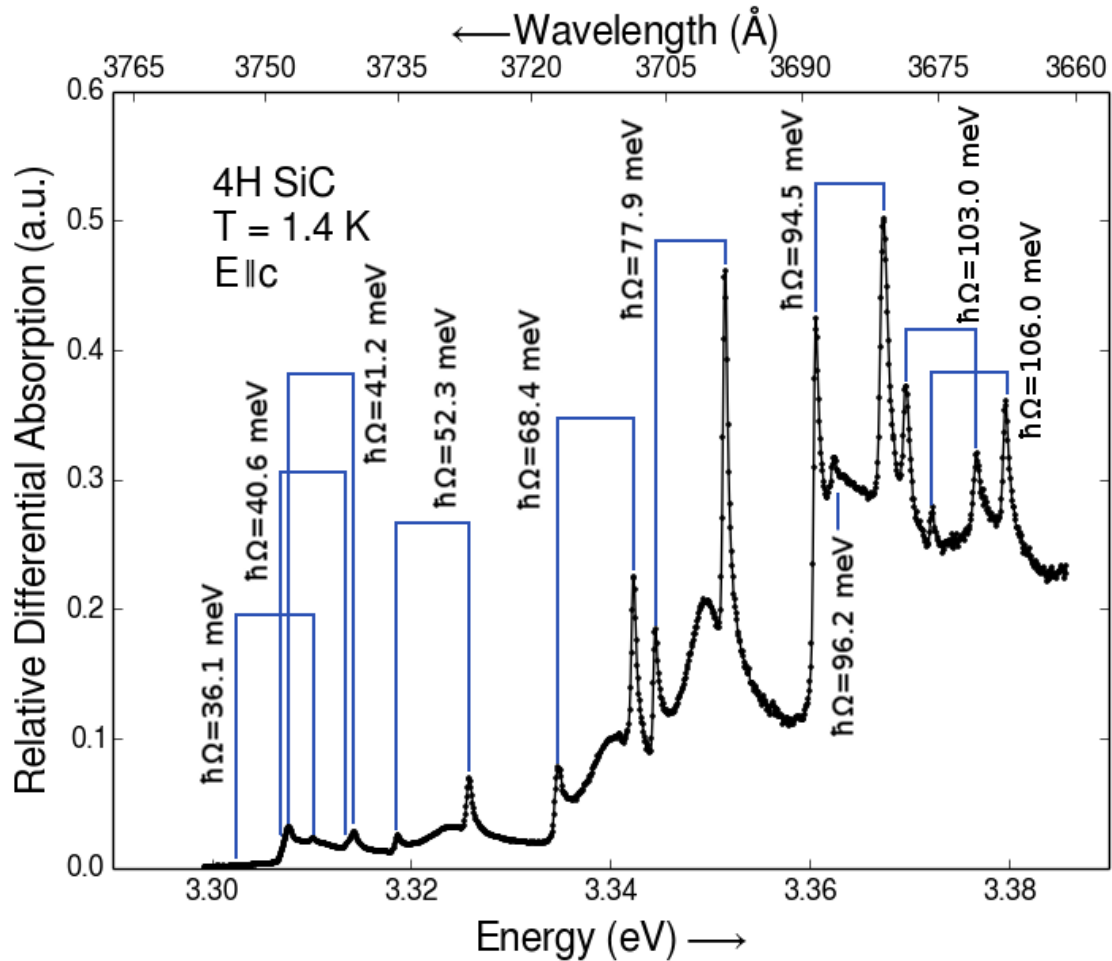


Figure 21: Low temperature wavelength modulated absorption measurements of the first ~ 80 meV of the fundamental absorption edge in 4H SiC for $\mathbf{E} \parallel \hat{c}$. All peaks are associated with the phonon-assisted creation of a free exciton whose electron occupies the lowest conduction band minimum and whose hole occupies either of the two uppermost valence band maxima. For each pair of peaks marked by a bracket, the separation between the two peaks roughly corresponds with the separation of the two uppermost valence band maxima, which is due to the spin-orbit splitting. Both peaks within a given pair are due to onsets in absorption with emission of the same phonon, whose energy in meV is shown above each bracket. The 96.2 meV phonon-assisted onset is not visible for the spin-orbit split-off exciton.

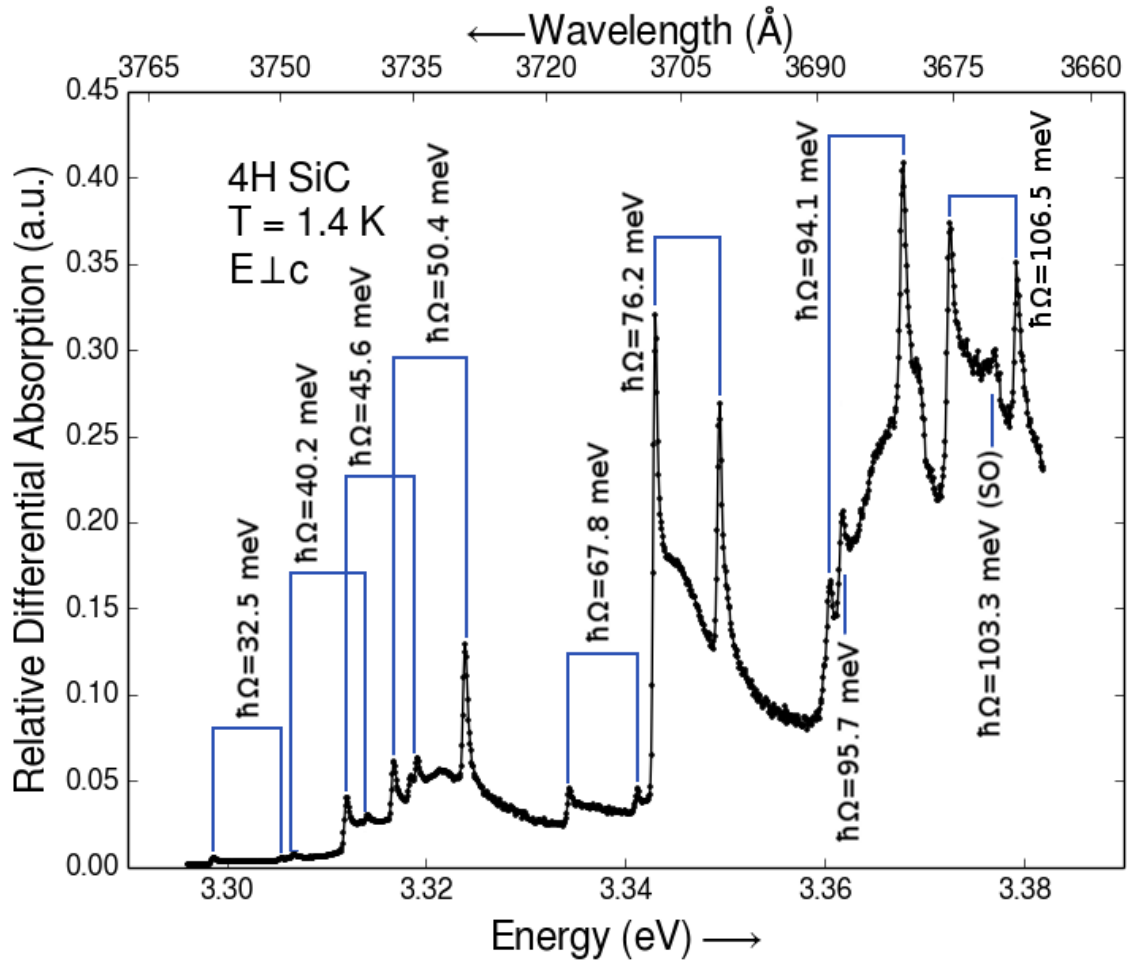


Figure 22: Similarly as with Figure 21 but with the incident light polarized $\mathbf{E} \perp \hat{c}$. The 103.3 meV phonon-assisted absorption onset is visible only for the spin-orbit split-off exciton, and so is labeled “SO.”

modes). Twelve of the 24 principal phonons in 4H SiC are spread out over a roughly 40 meV interval below this gap, whereas the remaining 12 above the gap often appear confined to a 10–20 meV interval. In particular for the calculated phonon energies listed by Serrano *et al.* there are 8 principal phonons in the interval $\hbar\Omega = 93.0\text{--}97.5$ meV. In this work 20 of the 24 possible principal phonons have been identified in either the WMA or LTPL measurements, and it is believed that the ones that are missing result from an inability to resolve this particular cluster of phonons.

The LTPL measurements used for comparison were taken from a number of different samples—both epitaxial layers and boule material—and the sample which yielded the spectrum most free of bound exciton photoluminescence was chosen as a reference. This reference sample, DC1025-23 A, was a high purity (nitrogen concentration $\approx 3 \times 10^{13}$ cm⁻³) 120 μm thick epi-layer cleaved into a 1×1 cm² piece from a larger wafer. To prevent it from contributing to the LTPL spectrum, the heavily doped substrate was totally removed by diamond polishing. This sample’s \hat{c} axis was normal to its cross-section, and so all polarized LTPL measurements were performed in the right angle geometry described in Section 4.2, with the LTPL being collected from one of its cleaved edges.

The sample was excited with a laser whose wavelength $\lambda_{ex} = 3550$ Å and whose power P_{ex} was adjusted between 60 μW and 60 mW to examine the changing shape of the free exciton emission lines. An overview of the polarized LTPL for $P_{ex} = 2$ mW is shown in Figures 23 and 24, and detailed close-ups of the weaker emission lines are shown in Figures 25 and 26. The labels I_x denote free exciton recombination with emission of a phonon of energy x in meV, and the labels P_x denote the P series of nitrogen-bound exciton phonon replicas. In the latter case, the phonon energies x were determined by measuring the phonon replica’s position relative to the no-phonon line P_o . The phonon energies assigned to the spectral features due to the free exciton have been determined from a joint consideration of the LTPL and WMA measurements, as discussed in the following section.

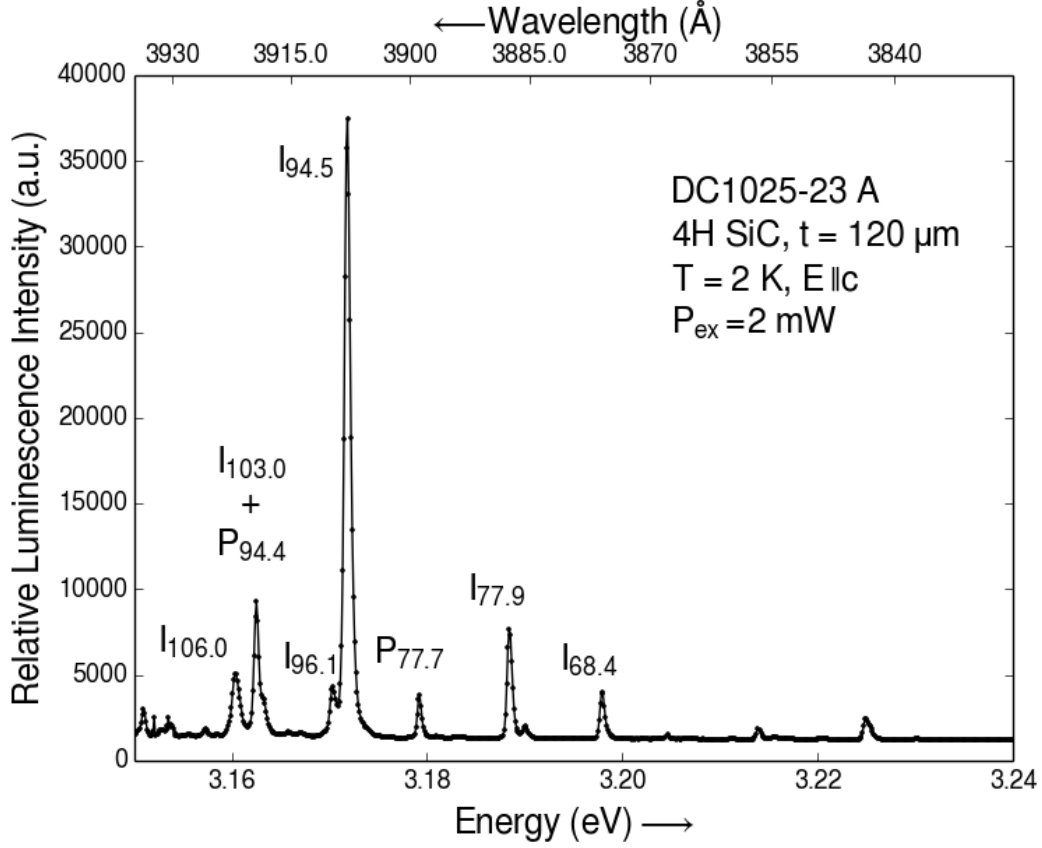


Figure 23: Overview of $E \parallel \hat{c}$ low temperature photoluminescence spectrum used for reference. Labels I_x denote indirect, free exciton recombination with emission of a phonon with energy x in meV. These energies were obtained by joint comparison with the low temperature wavelength modulated absorption spectrum, as described in the text. The lines denoted P_x are nitrogen-bound exciton emission lines assisted by a phonon of energy x in meV. This energy was determined from the line's offset from the no-phonon line P_0 (not shown).

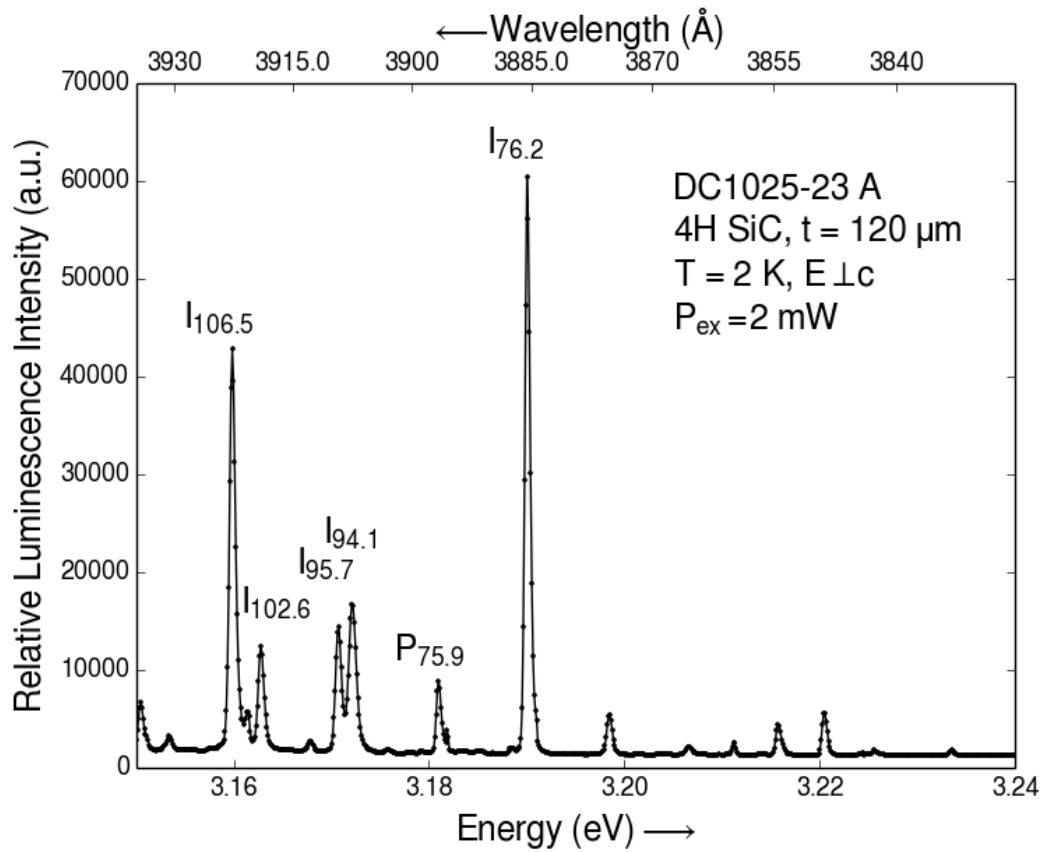


Figure 24: Overview of $\mathbf{E} \perp \hat{c}$ low temperature photoluminescence spectrum used for reference. The notation is the same as for Figure 23

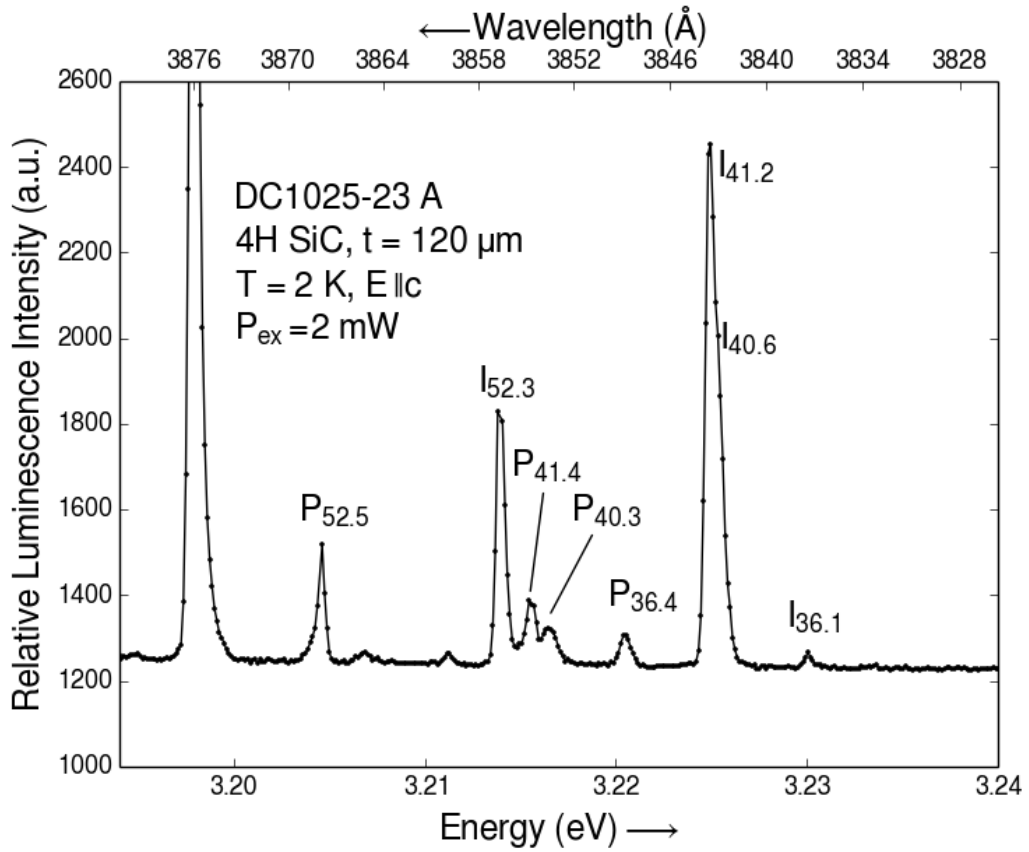


Figure 25: Close-up view of the weaker emission lines appearing in Figure 23

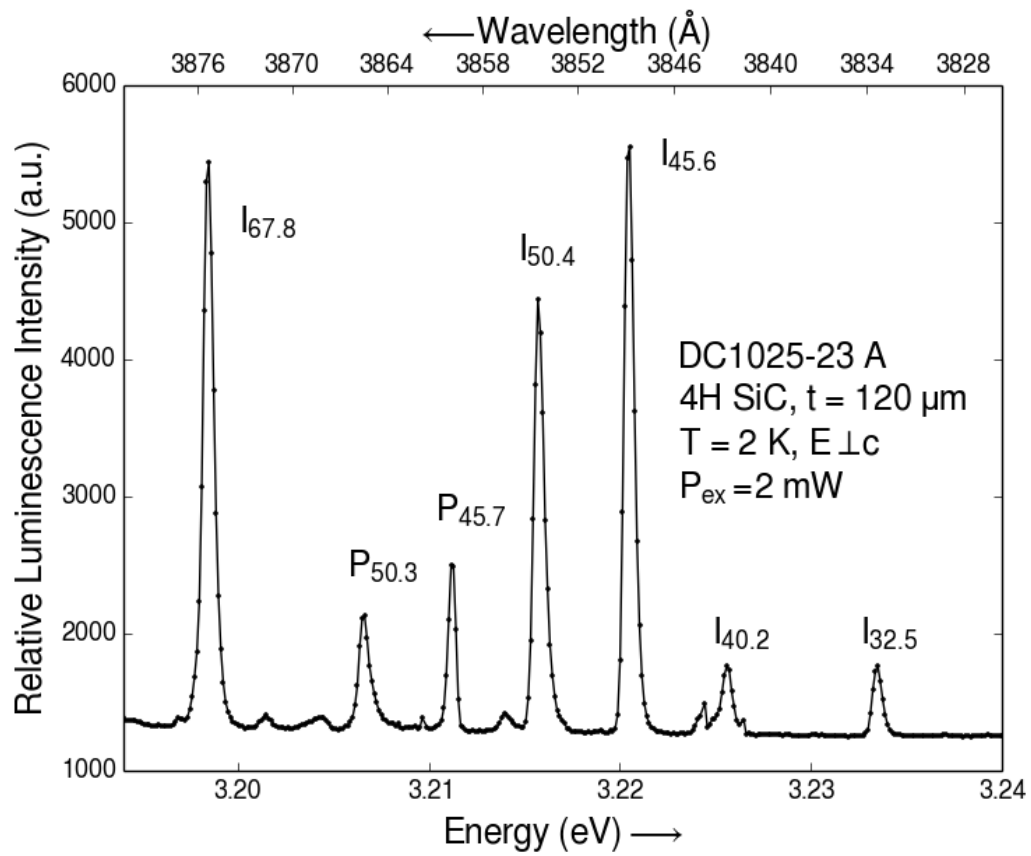


Figure 26: Close-up view of the weaker emission lines appearing in Figure 24

5.3 ASSIGNMENT OF FREE EXCITON EMISSION LINES AND ABSORPTION ONSETS

The assignment of specific phonons to the various absorption onsets and emission lines shown above is greatly facilitated by their mirrored positioning about the exciton bandgap, as shown schematically by Figure 8. Once one has identified the set of emission line–absorption onset pairs $(\hbar\omega^{(e)}, \hbar\omega^{(a)})$ that exhibit this symmetry collectively, one may then use equations (3.34) and (3.35) to compute the exciton bandgap and the energy of the phonon involved at each transition, as described in Section 3.4. Whereas that discussion allowed for the possibility that many different exciton states could contribute observable features to the spectra, several assumptions were made in order to reduce the complexity of the assignments. It was assumed firstly that all emission lines in the LTPL spectra originated from the lowest-lying exciton, EX_1 , and that any photoluminescence due to its spin-orbit split-off counterpart was thermally suppressed. Secondly, it was assumed that the selection rules derived in Section 3.2 for the case without spin could be followed, so that a given emission line appearing for one polarization would be looked for in the absorption spectrum of that same polarization. The third and final assumption was that at this stage no consideration needed to be made for the fourfold splitting of the exciton bands described earlier (which was assumed to be small), and that each emission line would therefore be mirrored about a common point $E_{gx}^{(1)}$ onto its corresponding absorption onset (see Figure 9 for a hypothetical example where this is not the case). It will be seen that each of these are reasonable assumptions to make, although the this last one can carry the analysis only so far before it becomes necessary to consider the more complete framework detailed earlier.

One complication which immediately arises is the set of absorption onsets due to the spin-orbit split-off exciton EX_{so} seen prominently in figures 21 and 22. To handle these it was assumed that, as with EX_1 , EX_{so} could be characterized by a single excitonic bandgap $E_{gx}^{(so)} = E_{gx}^{(1)} + \Delta'_{so}$, where Δ'_{so} is equivalent to the spin-orbit splitting of the valence bands Δ_{so} when the binding energies of EX_1 and EX_{so} are equal. Furthermore, since the selection rules for the case without spin are equivalent for both of these excitons (recall that both would have their electron in an M_4 CBM and their hole in the Γ_5 VBM), the spectrum due

to EX_{so} should be characterized by the same principal phonons as that for EX_1 for a given polarization. As a result the component of the absorption spectrum due to EX_{so} should appear alongside that of EX_1 as a nearly identical counterpart which is offset to higher energy by an amount Δ'_{so} . Two copies of the emission spectrum—both reflected onto the absorption spectrum about $E_{gx}^{(1)}$ ($\hbar\omega \rightarrow 2E_{gx}^{(1)} - \hbar\omega$) and one shifted up relative to the first ($\hbar\omega \rightarrow \hbar\omega + \Delta'_{so}$)—may therefore be used to simultaneously identify the absorption onsets due to either EX_1 or EX_{so} once the peaks in the reflected emission spectra come into alignment with the absorption onsets. The end result of this procedure as applied to the measurements above is shown in Figure 27.

The two free parameters in this procedure— $E_{gx}^{(1)}$ and Δ'_{so} —are readily constrained to small ranges by visual inspection, and for most of the absorption onsets this was enough to assign them to a particular principal phonon and one of the two excitons EX_1 and EX_{so} . In those cases where two or more emission lines could be assigned to a given absorption onset, the line of greatest intensity in the LTPL spectrum was chosen (with the intensity being determined from the fit to the LTPL data (5.6)). For the spectra polarized $\mathbf{E} \perp \hat{c}$ there were several instances for which a given emission line could be assigned to either of two closely-lying absorption onsets. It will be argued that these result from the splitting of the M_1 and M_3 exciton sub-levels, both of which are active for this polarization. In these cases the emission line is assigned to the lower of the two onsets, since the upper sub-level of the exciton will be suppressed in the LTPL spectrum. With this, every one of the absorption onsets has been accounted for in the wavelength range shown in Figures 21 and 22.

With the pairs $(\hbar\omega^{(e)}, \hbar\omega^{(a)})$ having been determined in the above procedure, the corresponding exciton bandgap and principal phonon energies were obtained from (3.34) and (3.35). These are compiled in Table 4 along with principal phonon energies measured by LTPL in references [49] and [28]. As mentioned earlier, the correspondence in the principal phonon energies is fairly good for the 12 lowest energy phonons, but is somewhat less so for the others. One should note that for the two principal phonons listed by reference [49] not appearing in these measurements the associated photoluminescence is quite weak (see Figure 8 in that reference), and may possibly be defect-related. There also exists some ambiguity in the data from reference [28], since all possible emission lines were overlaid in

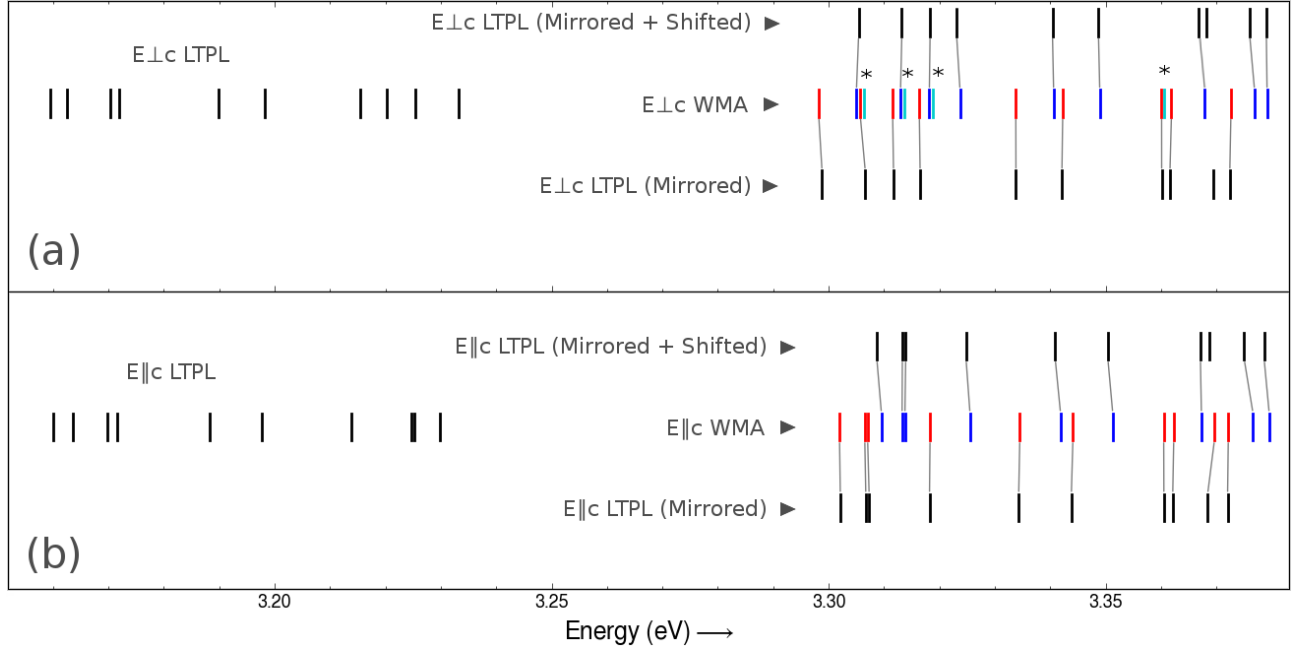


Figure 27: The emission lines in the low temperature photoluminescence (LTPL) of 4H SiC are shown on the left at lower energy and represented by vertical dashes. The wavelength modulated absorption (WMA) onsets are similarly represented at higher energies. The absorption and emission spectra represented here are polarized $\mathbf{E} \perp \hat{c}$ in (a) and $\mathbf{E} \parallel \hat{c}$ in (b). In order to assign each onset to a specific principal phonon and exciton, the LTPL is reflected about a specified point along the energy axis (here it is 3.266 eV) and aligned to the peaks in the absorption spectrum (“Mirrored” spectra). These may also be uniformly shifted to higher energy to align with those onsets due to the spin-orbit split-off exciton. Once an emission line $\hbar\omega^{(e)}$ has been paired with an absorption onset $\hbar\omega^{(a)}$, the associated exciton’s bandgap and the energy of the phonon involved in both transitions may be computed from (3.34) and (3.35). Those absorption onsets marked by asterisks are due to the splitting of the M_1 and M_3 sub-levels of the exciton band minimum.

a single, unpolarized spectrum. In any case, for the present purposes the absolute values of the phonon energies are not so important as the necessity to account for all 24, which would greatly facilitate the identification of unknown features in the WMA spectrum. If the calculated phonon branches are any indication, the remaining few may be very difficult to resolve adequately.

Finally, it is apparent from Table 4 that the exciton bandgap for the lowest energy exciton is $E_{gx}^{(1)} = 3.2660$ eV as found from an average over all rows. The spread in the listed values in the table for $E_{gx}^{(1)}$ is ± 0.2 meV, although there is also a significant uncertainty in the values for $\hbar\omega^{(e)}$ and $\hbar\omega^{(a)}$ from which the exciton bandgaps were obtained (0.3 and 0.5 meV, respectively). A more accurate estimate of the uncertainty in $E_{gx}^{(1)}$ is about ± 1 meV. The few outliers such as $E_{gx} = 3.2666$ eV may be due to overlap of an emission line with a nitrogen bound exciton emission line or overlap of an absorption onset with the spin-orbit split-off onset due to a different, nearby phonon. It should be pointed out that a sub-level is not specified in the above exciton bandgap, although it is possible that the values for $E_{gx}^{(1)}$ given in the table are distributed about two distinct values, $E_{gx}^{(1,1)}$ and $E_{gx}^{(1,3)}$, corresponding to the M_1 and M_3 sub-levels. However, because of the large experimental uncertainty involved, an analysis of this sort is not attempted.

5.4 FINE STRUCTURE SPLITTINGS OF THE FREE EXCITON BAND MINIMA

It is apparent from Figure 27 that no matter how one proceeds with the assignment procedure given above, one will always be left with at least a few unidentified absorption onsets. It is claimed here that these are due to the fourfold splitting of the free exciton band minima, but before continuing on to look at these splittings in more detail, it is helpful to highlight the reasons already stated or alluded to which support this position. Firstly, for all those measurements for which the instrumental resolution was adequate to resolve these splittings, not once have they failed to reproduce in repeated trials or in either of the two boules used for samples. Secondly, while these might be associated with the phonons not yet observed

Table 4: Positions $\hbar\omega^{(e)}$ of emission lines in the measured low temperature photoluminescence and corresponding absorption onsets at $\hbar\omega^{(a)}$ in the measured wavelength modulated absorption spectrum. For each row the lowest exciton bandgap $E_{gx}^{(1)}$ and principal phonon with energy $\hbar\Omega$ are computed from $\hbar\omega^{(e)}$ and $\hbar\omega^{(a)}$ using equations (3.34) and (3.35) in the text. (*Due to overlap with another onset, the bandgap in this row was computed from the average of the others in the same polarization, and the phonon energy alongside it was computed from this by subtracting $\hbar\omega^{(e)} = 3.1626$ eV). The phonon energies are compared with those obtained in the LTPL measurements of references [49] and [28]. The uncertainties in $\hbar\omega^{(e)}$ are ≈ 0.3 meV whereas the uncertainties in $\hbar\omega^{(a)}$ are ≈ 0.5 meV.

	$\hbar\omega^{(e)}$ (eV)	$\hbar\omega^{(a)}$ (eV)	$E_{gx}^{(1)}$ (eV)	$\hbar\Omega$ (meV)	Ref [49]: $\hbar\Omega$ (meV)	Ref. [28]: $\hbar\Omega$ (meV)
E \parallel \hat{c}						
	3.2299	3.3020	3.2659	36.1	36.6	36.5
	3.2253	3.3065	3.2659	40.6	40.6	40.6
	3.2247	3.3070	3.2659	41.2	41.9	41.7
	3.2138	3.3183	3.2660	52.3	52.7	52.7
	3.1977	3.3345	3.2661	68.4	68.8	68.7
	3.1882	3.3441	3.2661	77.9	78.0	78.5
	3.1715	3.3605	3.2660	94.5	94.7	96.1
	3.1699	3.3623	3.2661	96.2	96.5	97.8
	3.1636	3.3696	3.2666	103.0	103.5	105.6
	3.1600	3.3721	3.2661	106.0	106.3	108.2
	-	-	-	-	109.5	-
E \perp \hat{c}						
	3.2332	3.2982	3.2657	32.5	33.2	33.0
	3.2254	3.3057	3.2655	40.2	41.1	41.0
	3.2203	3.3116	3.2659	45.6	46.3	46.1
	3.2155	3.3164	3.2659	50.4	50.9	50.8
	3.1982	3.3338	3.2660	67.8	68.1	67.8
	3.1899	3.3422	3.2661	76.2	76.3	76.6
	3.1719	3.3601	3.2660	94.1	94.5	-
	3.1704	3.3619	3.2661	95.7	96	97.3
	-	-	-	-	98.9	100.3
	3.1626	-	3.2659*	103.3*	103.9	106.3
	3.1596	3.3726	3.2661	106.5	106.8	108.7

in the LTPL (20 of 24 have been identified in Table 4), the positions of most of the extra absorption onsets are low enough in energy that the missing phonons' energies would need to lie somewhere below the phonon energy gap with the acoustic phonons, which are already completely accounted for. Finally, there is the fact that all four of the additional onsets appear in the spectrum polarized $\mathbf{E} \perp \hat{c}$, as would be expected from the group theory analysis given in Section 3.2. Further consistency with this prediction will be demonstrated in the data to follow, which show that the additional peaks are not isolated but seem to be paired with another nearby as small 0.7 ± 0.1 meV splittings.

The clearest examples of these splittings are the three lying at lower energies in the absorption spectrum. These are shown in figures 28, 29, and 30. In the first of these figures appears a set of four peaks, all of which are assigned to the same phonon (with energy 40.2 meV). The two that are lower in energy are associated with the lowest-lying exciton EX_1 and the other two are associated with the spin-orbit split-off exciton EX_{so} . If the above interpretation is correct, this would mean that each pair is due to transitions into the M_1 and M_3 sub-levels of either exciton EX_1 or exciton EX_{so} . As in Figure 6, each of these should lie at the minima of a separate exciton sub-band. If we label each of the corresponding bandgaps by $E_{gx}^{(1,1)}$, $E_{gx}^{(1,3)}$, $E_{gx}^{(so,1)}$, $E_{gx}^{(so,3)}$ (the right index indicates the symmetry, M_1 or M_3), then the observed separations between the onsets in each pair are given by $\delta_{1,3}^{(1)} = |E_{gx}^{(1,3)} - E_{gx}^{(1,1)}| = 0.6$ meV and $\delta_{1,3}^{(so)} = |E_{gx}^{(so,3)} - E_{gx}^{(so,1)}| = 0.8$ meV (the energetic ordering of the sub-levels is not known, so the absolute value is taken). It should be noted that these two values are only marginally different, as the experimental precision for small energy separations such as these is approximately 0.1 meV.

In Figure 29 are shown *three* onsets all due to emission of the 45.6 meV principal phonon. In this case it is only the onset due to EX_{so} which exhibits a splitting. Its magnitude $\delta_{1,3}^{(so)} = 0.7$ meV agrees to within experimental error with that obtained in Figure 28. It should be emphasized that even though the lower energy onset shows no splitting, this is not inconsistent with the proposed group theory argument. As stated before, this is because the group theory analysis cannot distinguish whether or not a given transition is too weak to be observable. Also, it is not required that the transition rate to each of these exciton sub-levels relative to each other be repeated throughout the entire absorption spectrum, since

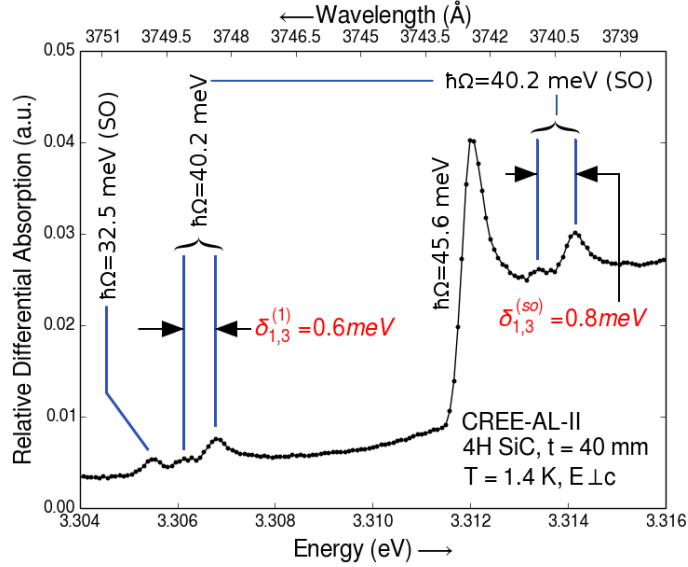


Figure 28: Detailed view of the wavelength modulated absorption spectrum for $\mathbf{E} \perp \hat{c}$ showing several absorption onsets labeled by the energy $\hbar\Omega$ in meV of the participating phonon. The label $\hbar\Omega$ is associated with the lowest-lying exciton (EX_1) whereas the label $\hbar\Omega(\text{SO})$ is associated with the spin-orbit split-off exciton (EX_{so}). Fine structure splittings appear in the the absorption onset due to emission of a 40.2 meV principal phonon for both excitons and are due to the splitting between their M_1 and M_3 sub-levels.

the probability amplitude (3.14) to which it is proportional would vary among the principal phonons through the electron-phonon interaction. What *would* successfully refute the group theory argument would be an observed splitting of multiplicity greater than two, but so far these have not been observed.

The last such splitting that is attributed to the exciton sub-level structure is shown in Figure 30 as a 0.6 meV splitting in the onset due to EX₁ with emission of the 94.1 meV principal phonon. The splitting agrees well with that found for $\delta_{1,3}^{(1)}$ in Figure 28, although in this case the onsets are partially obscured in the noise level. This is in part due to the absorption coefficient being larger in this wavelength interval, which required the use of a thinner sample (1 mm as opposed to 40 mm). Three separate trials are shown which attempt to reproduce the splitting, with the third trial being conducted at finer wavelength steps (0.02 Å rather than 0.1 Å). The assignment is also made somewhat more tenuous than the others by the fact that most phonon calculations show a large number of principal phonons near in energy to this 94.1 meV phonon, and these are likely to be among the ones not yet identified. In principle such a phonon should be observable as a high energy shoulder on the corresponding emission line in the LTPL spectrum. In Figure 31 is shown the LTPL due to the same two phonons as featured in Figure 30. It is seen that the 94.1 meV emission line, which appears on the right of the figure, exhibits no discernible shoulder and the two peaks are adequately fit by two free exciton emission curves. In the LTPL data the excitation power has been set very low (0.06 mW) to reduce the thermal broadening of the lines as much as practically possible. While this seems to support the above conclusion, a more careful analysis of the shape of this emission line is needed. This might be accomplished, for instance, by using a more finely grooved diffraction grating than the one currently installed for the LTPL apparatus (groove density: 1800 lines/mm), since this would allow data collection at higher resolution and finer wavelength increments.

An additional set of features which have not been resolved in previous absorption measurements is shown in Figure 32. The splittings have a similar size (0.6 meV) to those observed in the previous cases, but since the spectrum is polarized $\mathbf{E} \parallel \hat{c}$, these cannot be due to the splittings of the exciton sub-levels (since only one would be active in this case). However in this instance the four onsets are due to two closely lying principal phonons—one

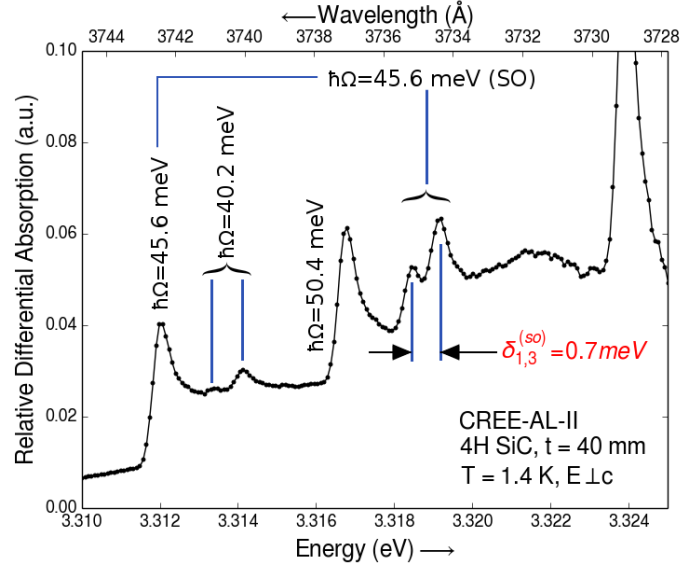


Figure 29: Detailed view of the same wavelength modulated absorption spectrum as in Figure 28 but at higher photon energy. An additional fine structure splitting is observed in the 45.6 meV phonon-assisted absorption onset of the spin-orbit split-off exciton (the splitting in the 40.2 meV phonon-assisted onset is from Figure 28). The value is consistent to within experimental error with the 0.8 meV splitting shown in Figure 28 for the spin-orbit split-off absorption onset associated with the 40.2 meV phonon.

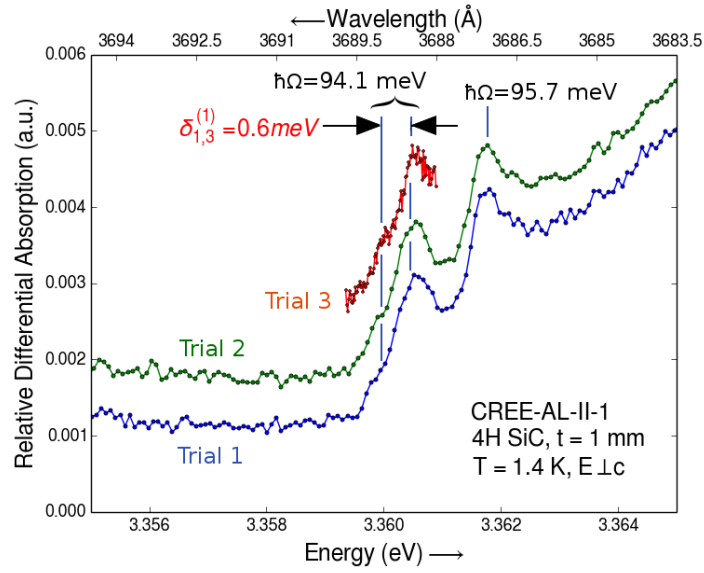


Figure 30: Three repeated measurements of the 94.1 meV phonon-assisted absorption onset due to the lowest-lying exciton (the third was recorded at finer wavelength steps). Each show a fine structure splitting which is consistent with the ones observed in Figures 28 and 29.

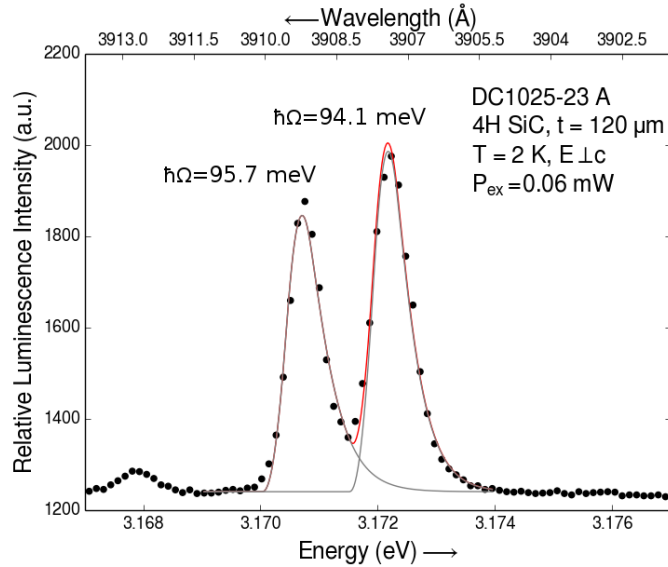


Figure 31: The 94.1 and 95.7 meV phonon-assisted emission lines are seen to be adequately fit to two free-exciton emission curves. This supports the conclusion that the fine-structure splitting seen in the 94.1 meV phonon-assisted absorption onset in Figure 29 is due to the splitting of the exciton sub-levels rather than one of the yet-unidentified principal phonons in 4H SiC. If the latter assignment were made, the unidentified phonon should give rise to a high energy shoulder on the 94.1 meV emission line, which does not seem to be the case here. The red curve indicates a fit to the two observed peaks (according to the form (5.6)) and the two gray curves show the fit decomposed into individual peaks.

with energy 40.6 meV and the other 41.2 meV—each of which contributes a spin-orbit split pair. The separation of 0.6 meV between the two phonons is also seen in the corresponding emission lines, as seen in Figure 33. The dependence of the LTPL on excitation power between 0.06 and 0.2 mW supports the notion that the two peaks are due to separate phonons rather than a pair of exciton sub-levels, since the relative heights of the individual peaks do not change considerably as the power is increased (in addition to the local temperature at the point of excitation). This would not be true for the latter case, as demonstrated schematically in the simulated LTPL of Figure 9.

The emission lines due to these two phonons have been resolved in previous LTPL measurements [49, 28], although their listed energies show their separation to be 1.1–1.3 meV (see Table 4). This is double the separation that is observed here and likely cannot be accounted for by experimental error. The discrepancy likely originates from the phonon energies in references [49] and [28] having been measured using the *bound exciton* phonon replicas. In fact, the same 1.1 meV separation measured in reference [28] is observed in Figure 25 between $P_{40.3}$ and $P_{41.4}$. What causes the measured phonon energies to differ between the free and bound excitons is unknown in this case, but for the present purposes it is sufficient that the emission lines shown in Figure 33 are consistent with the assignments given in Figure 32.

For the remaining absorption onsets which do not exhibit a splitting the separation between the M_1 and M_3 exciton sub-levels may be determined indirectly in the following way. Since, from a symmetry standpoint, the two excitons EX_1 and EX_{so} are indistinguishable (both have their electron in an M_4 symmetry conduction band minimum and their hole in a Γ_5 symmetry valence band maximum in the case without spin, and both split into the quadruplets $M_1 \oplus M_2 \oplus M_3 \oplus M_4$ in the case with spin), the same sub-levels should be active for both in the same spectrum. For instance, with $\mathbf{E} \parallel \hat{c}$ each phonon with symmetry M_1 will give rise to one absorption onset due to the excitons EX_1 and one onset due to EX_{so} , and moreover the active exciton sub-levels in both cases have M_1 symmetry. As a result, the apparent spin-orbit splittings observed in the $\mathbf{E} \parallel \hat{c}$ absorption spectrum in Figure 21 come in two varieties: $\Delta'_{so}{}^{(1)} = E_{gx}^{(so,1)} - E_{gx}^{(1,1)}$ and $\Delta'_{so}{}^{(3)} = E_{gx}^{(so,3)} - E_{gx}^{(1,3)}$, where the former are observed when M_1 symmetry phonons assist the transitions and the latter are observed for M_3 symmetry phonons (see Figure 34). The situation for the $\mathbf{E} \perp \hat{c}$ polarized spectrum

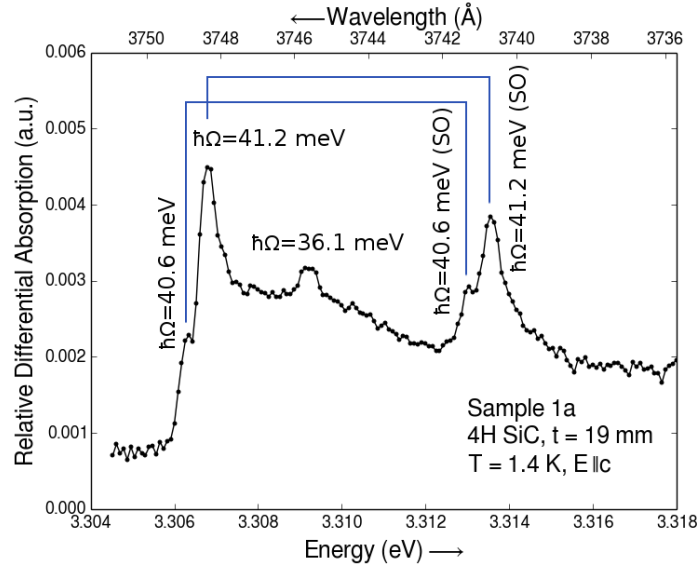


Figure 32: Two pairs of small splittings are observed in the wavelength modulated absorption spectrum for $\mathbf{E} \parallel \hat{c}$ which are comparable to the ones observed in Figures 28 through 30. Unlike those splittings, however, these are *not* due to the splittings in the exciton sub-levels. Rather, they result from the small energy separation of the two phonons that are involved: 40.6 meV and 41.2 meV. Each of these gives rise to two absorption onsets (one for the lowest-lying exciton and the other for the spin-orbit split-off exciton) that are slightly offset from each other by the difference in the phonon energies.

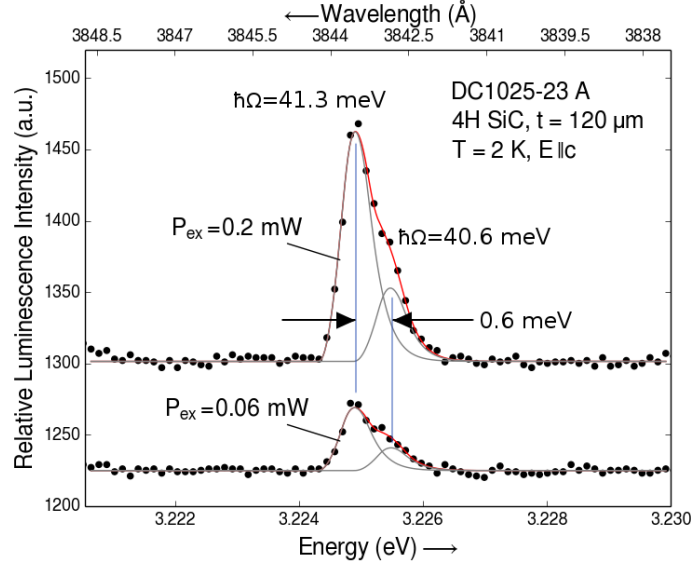


Figure 33: The spacing between the two phonons observed in Figure 32 is corroborated in their corresponding emission lines, which also show a 0.6 meV separation. The spectrum is measured at two different excitation intensities to raise the sample temperature, and it is seen that the relative heights for the two peaks does not vary appreciably. This supports the assignment of these two features to separate phonons rather than different exciton sub-levels, since the LTPL from the upper sub-level would increase in intensity with temperature. The red curve shows the overall fit to the two peaks in the data (according to the form (5.6)) and the gray curves show the fits decomposed into individual peaks. An offset between the two data sets has been introduced for clarity.

is not definitive, since in those cases where a splitting is not observed, it is unknown which of the two allowed sub-levels is dominant.

In Figure 35 is shown a histogram of the spin-orbit splittings measured from many independently recorded absorption spectra for both polarizations. In both cases the distribution is seen to be bimodal, which gives a preliminary indication that these energy separations do in fact fall among the two varieties mentioned above. The spread in the distribution is likely determined by the wavelength precision of the WMA measurement (in measuring energy differences of this size, the precision is roughly 0.1–0.3 meV). Since for $\mathbf{E} \parallel \hat{c}$, each of the observed spin-orbit splittings is correlated with the symmetry of the participating phonon, this analysis could be taken a step further if the symmetries of the phonons were known.

This may be done using Table 1 from Serrano *et al.* [79], which lists the calculated energies of the principal phonons alongside their symmetries. Associating each of the listed phonons with the ones measured here was established indirectly through the measured phonon energies reported by Ivanov *et al.*, which are shown in the table alongside the calculated phonon energies Serrano *et al.* have associated them with (although they do not state their rationale). Assuming these to be correct, and making use of the correspondence already made in Table 4 to the work by Ivanov *et al.*, the following (tentative) equivalence was made:

$$\hbar\Omega (\text{This work}) \iff \hbar\Omega (\text{Ivanov } et \text{ al.}) \iff \hbar\Omega (\text{Serrano } et \text{ al.}) \quad (5.7)$$

Once the calculated phonon energy was identified with the measured values in this work, its associated symmetry listed alongside it was identified as well. The result of this comparison is summarized in Table 6.

In the table, the column denoted Δ'_{so} gives the measured spin-orbit splitting for the particular phonon listed alongside it in the same row. The values of Δ'_{so} have been averaged over only those data sets for which *both* absorption onsets in a given spin-orbit split pair are observed. Here what is meant by data set is a single, continuous sweep through a segment of the absorption spectrum, *without* reversing the rotation direction of the monochromator's diffraction gratings. This is to avoid measurement errors due to backlash of the monochromator gearing mechanism, but it also ensures that day-to-day temperature drifts do not

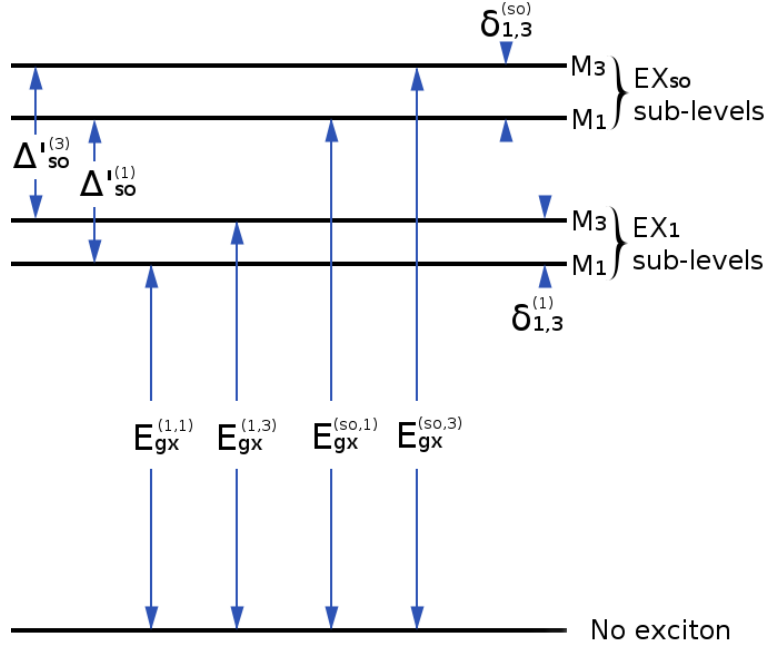


Figure 34: For both the lowest-lying exciton EX_1 and the spin-orbit split-off exciton EX_{so} , their optically active sub-levels at their corresponding band minima have symmetry M_1 and M_3 . Their energetic separations relative to each other and to the "vacuum state" with no excitons present are referred to in the text by the displayed labels. For simplicity the level scheme is represented such that the M_3 symmetry sub-levels are higher than the M_1 sub-levels for both EX_1 and EX_{so} , although this need not be the case. Note that the arrows simply denote energy separations, and are not meant to indicate optical transitions.

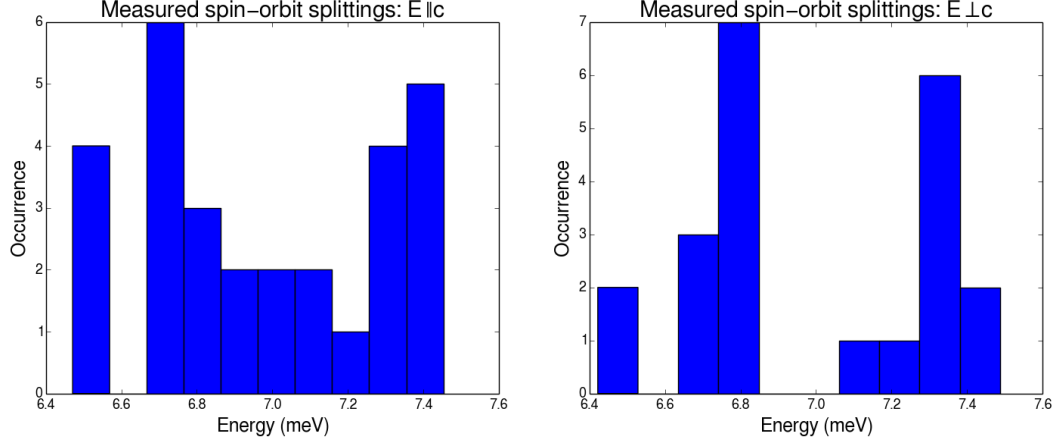


Figure 35: Histogram of the spin-orbit splittings measured from a group of several independently recorded wavelength modulated absorption spectra. The distribution appears to be bimodal for both $\mathbf{E} \parallel \hat{c}$ and $\mathbf{E} \perp \hat{c}$, and this may be associated with the energy splitting in the exciton sub-levels of the lowest-lying exciton and the spin-orbit split-off exciton.

play a role. The spin-orbit splittings for certain principal phonons are missing from the table because no such data sets were available (those phonons which exhibit exciton sub-level splittings are also excluded).

It is seen that for the $\mathbf{E} \parallel \hat{c}$ component of the table, the average measured Δ'_{so} for the M_1 symmetry phonons is in all cases larger than that for the M_3 symmetry phonons. To summarize the results for all of the $\mathbf{E} \parallel \hat{c}$ active phonons, it is found that for M_1 symmetry phonons $\Delta'_{so}{}^{(1)} = 7.2 \pm 0.3$ meV and for M_3 symmetry phonons $\Delta'_{so}{}^{(3)} = 6.7 \pm 0.3$ meV. For the $\mathbf{E} \perp \hat{c}$ active phonons there does not appear to be an obvious correlation with the phonon symmetries, although this might be expected for the reasons already discussed. In this case it is found that for both M_2 and M_4 symmetry phonons $\Delta'_{so} = 7.0 \pm 0.3$ meV.

For the spin-orbit splitting measured in the $\mathbf{E} \parallel \hat{c}$ spectra, we may directly relate the small difference between $\Delta'_{so}{}^{(1)}$ and $\Delta'_{so}{}^{(3)}$ to the measured fine structure splittings $\delta_{1,3}^{(1)}$ and $\delta_{1,3}^{(so)}$. To do so we assume that $\Delta'_{so}{}^{(1)}$ is indeed larger than $\Delta'_{so}{}^{(3)}$ as the above would indicate, and further take $\delta_{1,3}^{(so)} > \delta_{1,3}^{(1)}$ as suggested in the measurements in figures 28, 29, and

Table 5: The principal phonons are identified in the left-most column by their energy $\hbar\Omega$ measured in this work. In order to identify their symmetries, they are associated first with the closest experimental value given in reference [49] (as was done in Table 4), which have themselves been associated by the authors of reference [79] with calculated phonon energies and symmetries. The correspondences made by those authors is carried over to the following table, so that the symmetries given in the right-most column correspond with the measured principal phonon energies determined in this work.

$\hbar\Omega$ (meV)	Ref [49]: $\hbar\Omega$ (meV)	Ref [79]: $\hbar\Omega$ (meV)	Ref. [79]: Phonon symmetry
$\mathbf{E} \parallel \hat{c}$			
36.1	36.6	34.9	M_1
40.6	40.6	38.7	M_3
41.2	41.9	39.4	M_3
52.3	52.7	51.3	M_1
68.4	68.8	68.5	M_1
77.9	78.0	75.8	M_1
94.5	94.7	93.2	M_3
96.2	96.5	94.4	M_3
103.0	103.5	96.9	M_1
106.0	106.3	103.5	M_1
$\mathbf{E} \perp \hat{c}$			
32.5	33.2	32.5	M_2
40.2	41.1	39.4	M_4
45.6	46.3	45.1	M_2
50.4	50.9	50.2	M_4
67.8	68.1	67.8	M_4
76.2	76.3	74.7	M_4
94.1	94.5	93.0	M_2
95.7	96	94.0	M_4
103.3	103.9	102.5	M_4
106.5	106.8	106.2	M_4

Table 6: Measured spin-orbit splittings Δ'_{so} between pairs of wavelength modulated absorption onsets due to the same principal phonon are compared with the symmetry of the phonon, as given by reference [79]. The identification of the phonon symmetries follows the associations given in Table 5. The values Δ'_{so} have been averaged over several data sets for which both onsets in the given pair appear. For some phonons, these data sets were not available, and so do not appear in the table.

		Ref. [79]:
Δ'_{so} (meV)	$\hbar\Omega$ (meV)	Phonon symmetry
$\mathbf{E} \parallel \hat{c}$		
7.4	36.1	M ₁
6.6	40.6	M ₃
6.6	41.2	M ₃
7.2	52.3	M ₁
7.4	68.4	M ₁
7.2	77.9	M ₁
6.7	94.5	M ₃
7.0	103.0	M ₁
7.4	106.0	M ₁
$\mathbf{E} \perp \hat{c}$		
6.8	32.5	M ₂
7.2	50.4	M ₄
6.8	67.8	M ₄
6.6	76.2	M ₄
6.7	106.5	M ₄

30. Two possibilities which are consistent with these observations then arise, as shown in Figure 36. In Case 1 of the figure, the energetic ordering of the sub-levels between exciton EX_1 and exciton EX_{so} is reversed, and we have for the difference in the observed splittings: $\Delta'_{so}{}^{(1)} - \Delta'_{so}{}^{(3)} = \delta_{1,3}^{(so)} + \delta_{1,3}^{(1)}$. For Case 2 the ordering is the same between the two excitons so that we have instead $\Delta'_{so}{}^{(1)} - \Delta'_{so}{}^{(3)} = \delta_{1,3}^{(so)} - \delta_{1,3}^{(1)}$. Assuming we have $\delta_{1,3}^{(so)} = 0.8$ meV and $\delta_{1,3}^{(1)} = 0.6$ meV as in Figure 28, we then find $\Delta'_{so}{}^{(1)} - \Delta'_{so}{}^{(3)} = 1.4$ or 0.2 meV. The latter of these seems to fit with the measurements given above, but only marginally so. For this case we could conclude from the figure that $E_{gx}^{(so,1)} > E_{gx}^{(so,3)}$ and $E_{gx}^{(1,1)} > E_{gx}^{(1,3)}$. At this point, however, it is clear that better experimental precision is needed in order to affirm this.

A more promising avenue for exploring the size and nature of these small sub-level splittings would be to study the temperature dependence of the LTPL spectra under high resolution. It has been assumed in this work that all observed free exciton photoluminescence originates from recombination of an exciton in its lowest active sub-level, but if the temperature is raised somewhat above liquid helium temperature, it should be possible to observe recombination from the higher active sub-level, as shown in concept by Figure 9. An attempt at this has been made on a few occasions here by increasing the excitation intensity (see Figure 33), however in this case the control and monitoring of the temperature is not adequate. Furthermore, in order to better measure these effects at the required resolution, it may be necessary to re-configure the LTPL measurement apparatus with more finely grooved diffraction gratings, as already mentioned.

Besides temperature dependent effects, another aspect of the absorption and emission spectrum which might be studied is the dependence on external perturbations like uniaxial strain and magnetic fields. Methods for doing so have been developed and implemented in the case of the cubic semiconductors silicon and germanium [83, 84, 85, 86, 87]. Analogous measurements could conceivably be performed in the case of the cubic 3C SiC polytype, but for a hexagonal polytype like 4H SiC the analysis of the resulting spectra would likely be fairly complicated due to their reduced symmetry.

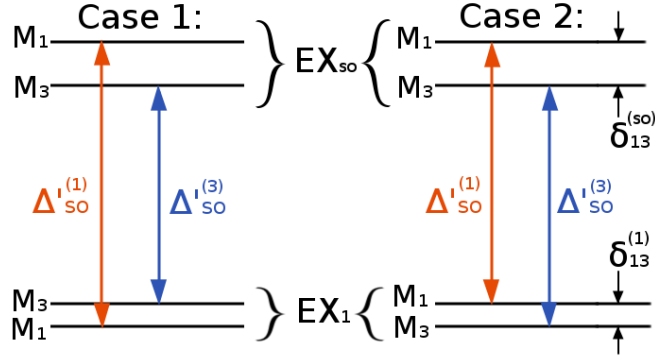


Figure 36: The two different orderings of the sub-levels for the lowest-lying exciton (EX₁) and the spin-orbit split-off exciton (EX_{so}) which are consistent with the observed spin-orbit splittings in the $\mathbf{E} \parallel \hat{c}$ polarized wavelength modulated absorption spectrum. In either case the spin-orbit splitting $\Delta'_{so}{}^{(1)}$ is observed for M₁ symmetry phonons and for M₃ symmetry phonons it is $\Delta'_{so}{}^{(3)}$. Between Case 1 and Case 2 the ordering of the sub-levels between EX₁ and EX_{so} is reversed. Other possibilities have been eliminated from the experimental observations that $\Delta'_{so}{}^{(1)} > \Delta'_{so}{}^{(3)}$ and $\delta_{1,3}^{(so)} > \delta_{1,3}^{(1)}$.

5.5 SPECTRAL FEATURES DUE TO ENERGY BAND NONPARABOLICITY

In the preceding discussion, the highlighted features of the wavelength modulated absorption spectrum were the threshold energies $\hbar\omega^{(a)}$ at which an indirect exciton could be created in a specified exciton band minimum E_{gx} . With account made for broadening, these closely followed the expected inverse-square-root dependence for $d\alpha/d\lambda$ on photon energy in the near-vicinity of the onsets, as shown in Figure 20. However, as the photon energy is increased further above these thresholds, the measured absorption onsets show strong deviations from the expected shape. This is most clearly seen in the overview of the $\mathbf{E} \parallel \hat{c}$ polarized wavelength modulated absorption spectrum shown in Figure 21 in the absorption onsets assigned to the 52.3, 68.4, and 77.9 meV energy phonons. It is seen that each of these phonons gives rise to a spin-orbit split pair of sharp absorption onsets, in between which lies a much broader bump. A similar feature appears just below the spin-orbit split-off absorption onset for the 50.4 meV phonon for $\mathbf{E} \perp \hat{c}$ as well, although it is partially obscured by onsets due to other phonons.

None of these features could be adequately fit to the expected shape for an indirect absorption onset even when accounting for broadening, but they do bear a striking similarity to one found in the wavelength modulated absorption measurements of germanium [88, 89]. There, the feature was attributed to an avoided crossing between two exciton bands split by mass anisotropy (see Figure 1 in reference [89]). Given that germanium is a cubic semiconductor, a direct comparison of these two observations cannot be made. However, it does strongly suggest that similar avoided crossings seen in the calculated valence bands of 4H SiC play a role. In the following it will be argued that the features mentioned above are the result of optical transitions of electrons originating from these highly nonparabolic regions of the valence bands, specifically those where the top two spin-orbit split valence bands undergo an avoided crossing.

This assertion is motivated in part by the fact that, roughly speaking, the absorption coefficient is proportional to the density of states for the exciton band [19, 89], and this in turn is connected to the curvature of the valence bands. As argued in Section 3.3, it may

be possible to introduce the effects of energy band nonparabolicity when either the valence band effective mass or conduction band effective mass is significantly larger than the other. This is at least partially true for the component of the valence band effective mass along the Γ -A direction, which from Table 1 appears to be 3–6 times larger than the components of the conduction band effective mass. Assuming this to be adequate, we have from (3.30) that above a given absorption onset with threshold $\hbar\omega^{(a)} = E_{gx} + \hbar\Omega$, the absorption coefficient then follows very roughly as $N_v(\hbar\omega^{(a)} - \hbar\omega)$, where $N_v(E)$ is the density of states of the *valence band*.

Since the wavelength modulated absorption measurements do not measure the absorption coefficient itself but its wavelength derivative, directly relating this result to the present data requires not only calculating the density of states, but also its energy derivative. The valence band density of states has been computed from *ab initio* band structure calculations in various literature sources [20, 15], but its energy derivative is not available. In principle, however, if the form of the valence band is known as a function of the wavevector \mathbf{k} within the Brillouin zone, one may compute the density of states either numerically or analytically as in the simple example given in (3.32). In reference [15] the authors have fit a k·p theory energy band model to the results of their density functional theory calculations and listed the results of the fit in their Table 4. These same models and parameters are used here to compute the density of states and its energy derivative. It should be noted, however, that while the spin-orbit interaction is parameterized in the model, the value for the parameter is not fixed by their non-relativistic band structure calculations. That parameter was chosen here to produce a 7 meV separation between the top two valence band maxima, which roughly corresponds to the observed spin-orbit splittings in the absorption spectrum. Further discussion of the k·p theory model used in [15] and the selection of parameter values is given in Appendix B.

Six model valence bands are obtained from the parameters given in [15], and are plotted together in Figure 37 versus wavevector along two different symmetry directions in the Brillouin zone: Γ -M and Γ -A. These are just the three uppermost valence bands that have been referred to elsewhere but with their spin explicitly included. The spin-orbit splitting Δ_{so} and crystal field splitting Δ_{cf} referred to earlier are also represented in the figure. Along the

direction Γ –A these six valence bands form a group of three that are each twofold degenerate, while along Γ –M the degeneracy is broken. For simplicity this broken degeneracy will be ignored so that we only consider three bands with distinct maxima. It is seen that along the Γ –M direction the lower two valence bands undergo an avoided crossing at $k \approx 0.04 \text{ \AA}^{-1}$. In Figure 38 a similar avoided crossing is shown to occur between the two uppermost valence bands along the same direction at $k \approx 0.02 \text{ \AA}$. It will be shown that this particular feature in the band structure is likely to be primarily responsible for the bumps appearing in the WMA spectrum.

Because the functional form of each of the model valence bands obtained above are too complicated to be handled analytically, the density of states was computed numerically. The procedure follows that given in reference [90]. In essence the objective is to compute the following integral, to which the density of states is proportional:

$$N_v(E) \propto \int \frac{dS(E)}{|\nabla E_v(\mathbf{k})|}, \quad (5.8)$$

where $dS(E)$ is an infinitesimal area element in k -space within the surface $E_v(\mathbf{k}) = E$ (note that, by the chain rule for delta functions, this is equivalent to the expression (3.31) given in Section 3.3 [59]). The computation proceeds first by dividing k -space into many small tetrahedral cells and then linearly interpolating the integrand within each of the cells. The integral then becomes a sum over all of these cells with the contribution of each cell to the resulting sum being a simple piecewise quadratic function of E . Each of these contributions may be summed together to obtain the approximate integral. The derivative of the density of states is readily computed by summing over the derivative of each of the piecewise functions. The details of the computation as performed in this specific case are also given in Appendix B.

The density of states N_v and its corresponding energy derivative dN_v/dE are shown in Figure 39 for a range of energies encompassing the top two valence band maxima. The appearance of noise in the derivative is an artifact from the numerical integration above. In this range of energy N_v contains a contribution from both of the top two valence bands, as can be seen by two abrupt rises—one at $E = 0$ and the other at $E = -\Delta_{so} = -7 \text{ meV}$ corresponding to each maximum. Their shape is similar to the square root dependence on

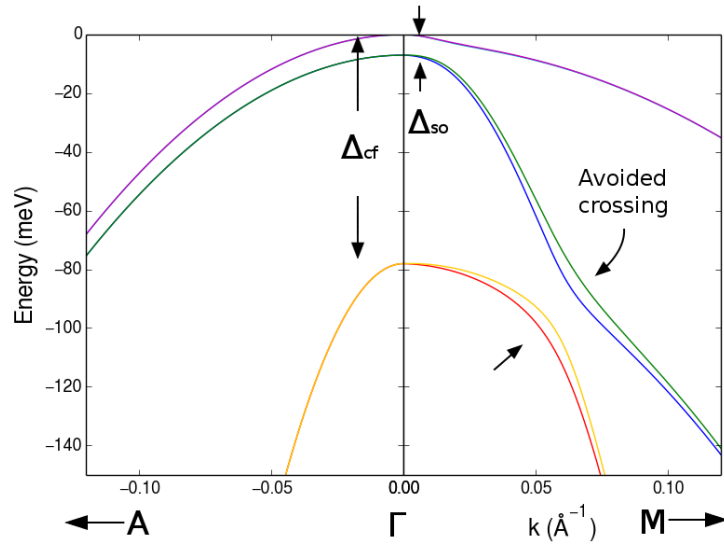


Figure 37: Top three valence bands of 4H SiC plotted in two directions in the Brillouin zone: Γ -M (right side of figure) and Γ -A (left side of figure). Each is twofold spin degenerate along the Γ -A axis, and along the Γ -M direction this degeneracy is broken. Along the Γ -M direction the lowest pair of bands (red and yellow curves) undergoes an avoided crossing with the second lowest pair (blue and green curves).

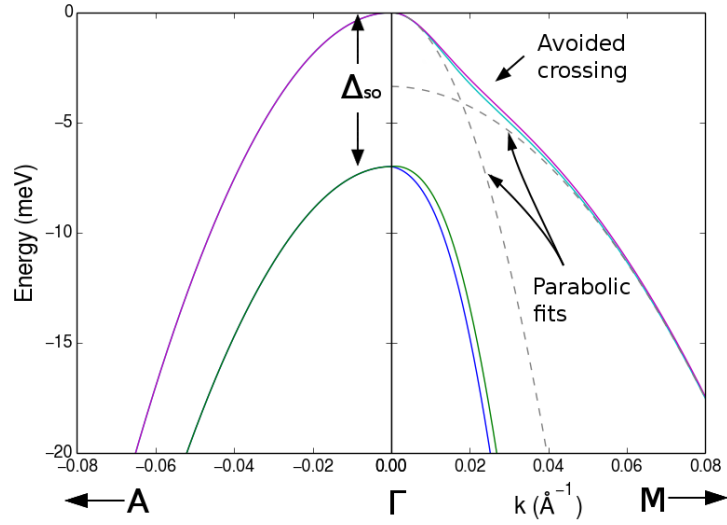


Figure 38: Expanded view of Figure 37 showing an avoided crossing between the topmost valence band (purple and cyan curves) and the spin-orbit split-off valence band (blue and green curves) along the Γ -M direction (their twofold spin degeneracy has also been broken along this direction). The dotted lines show parabolic fits to the uppermost valence band on either side of the avoided crossing on this axis, showing that the curvature of the band is altered from one side of the avoided crossing to the other.

energy expected for parabolic bands (see 3.32), although in the energy range between these there may be observed a slight bulging upwards due to the avoided crossing between this pair of valence bands. The corresponding features in the energy derivative dN_v/dE are more prominent: at the two band maxima appear sharp, inverse-square-root type peaks and in the region between appears a clear bump with an uncanny resemblance to the ones observed in the WMA measurements.

In Figure 40 is shown a direct comparison of the calculated derivative dN_v/dE with two of these features from the $\mathbf{E} \parallel \hat{c}$ polarized WMA spectrum. Two copies of the calculated dN_v/dE have been reflected about $E = 0$ and shifted rigidly up along the energy axis to align with the spin-orbit split pairs of absorption onsets due to the 68.4 and 77.9 meV phonons. This is justified by the rather naive approximation $\alpha(\hbar\omega) \sim N_v(\hbar\omega^{(a)} - \hbar\omega)$ given earlier, and yet the correspondence between the calculated curves and the measured spectra is very good. This suggests the following physical interpretation: For a given principal phonon, the initial, lower energy onset of absorption is associated with the threshold photon energy at which electrons may be promoted to the conduction band minimum from the uppermost valence band maximum. As the photon energy is increased higher still, it becomes possible to excite electrons from the lower portions of the valence band to the conduction band minimum while still conserving energy and momentum. In the regions where this band “flattens out” due to the avoided crossing with the lower valence band, a larger number of states with the required energy are available to be promoted to the conduction band, resulting in an increase of absorption that is somewhat more gradual than the initial onset. Conversely, the shape of the conduction band should play a similar role, but evidently it is the valence band which has the largest influence on the absorption spectrum, as had been initially supposed.

One difference between the calculated dN_v/dE and the absorption spectrum that may be commented upon is the added weight given to the spin-orbit split-off peak in the latter. In answer to this it should be pointed out that the above approximation has been made with complete neglect for probability amplitudes (3.14) which characterize the strength of electron-photon and electron-phonon interactions at play in each particular indirect transition. In this case these are likely somewhat different for the uppermost valence band maximum compared to the spin-orbit split-off valence band maximum. As in Elliott’s derivation

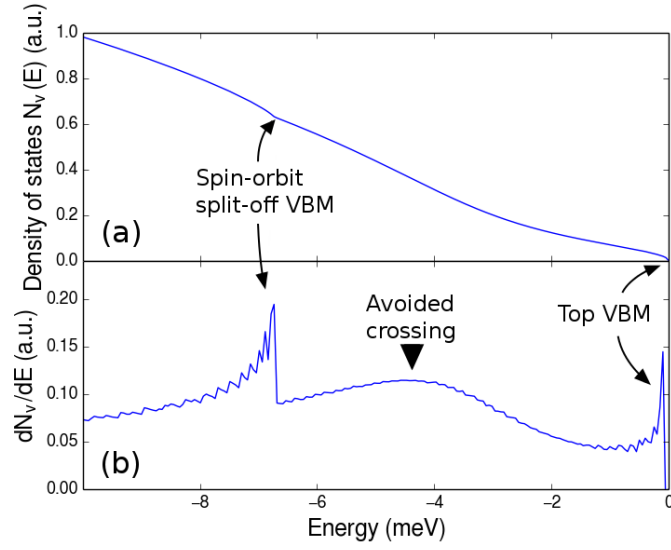


Figure 39: (a) The calculated density of states $N_v(E)$ of the valence bands in 4H SiC is shown along with (b) its energy derivative dN_v/dE for the energy range encompassing the top two valence band maxima (VBM). The apparent noise in the derivative is an artifact of the numerical calculation. At $E = 0$ there is an abrupt rise in N_v due to the maximum of the top valence band. At $E = -\Delta_{so} = -7$ meV a similar rise may be seen due to the second highest valence band maximum. In the derivative, these become sharp, asymmetric peaks. The broad bump in between is the result of an avoided crossing between these two valence bands.

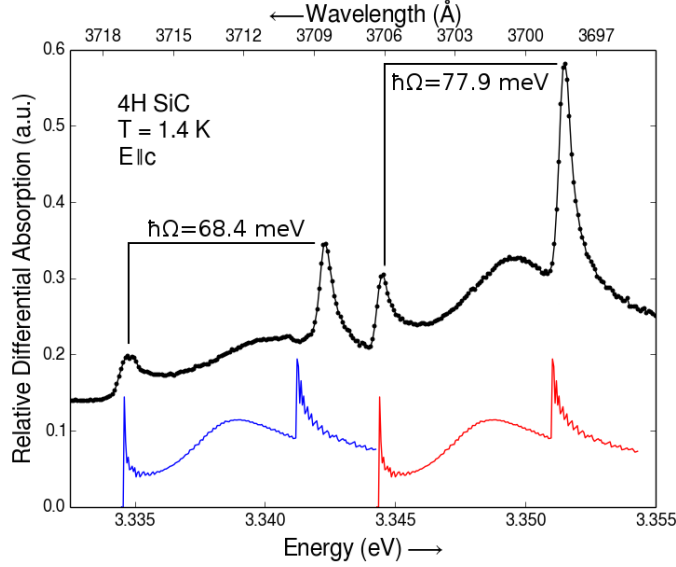


Figure 40: The calculated energy derivative of the density of states dN_v/dE for the valence bands of 4H SiC is compared to similar features appearing in the measured wavelength modulated absorption spectrum. In the measured data (black circles) two spin-orbit split pairs of peaks are observed due to emission of a 68.4 or 77.9 meV phonon (as indicated above each pair). The blue and red curves are two copies of the calculated derivative dN_v/dE and are shown superimposed (by reflection of dN_v/dE about $E = 0$ and shifting along the energy axis) on the plot below each spin-orbit pair for direct comparison of its features to the measured spectrum. The rounded bump in the calculated curves is due to an avoided crossing between the top two valence bands, and bears strong resemblance to the broad bumps appearing in the wavelength modulated absorption spectrum.

for the square root dependence of the absorption coefficient on photon energy, it is often assumed these probability amplitudes do not vary appreciably from that describing the initial absorption onsets [19].

However, if this simplification is removed, they could have a determining factor in the overall shape of the absorption onsets beyond the abrupt thresholds. This would explain why the shape of the density of states derivative dN_v/dE is not repeated throughout the rest of the WMA spectrum for all of the spin-orbit split pairs of onsets. For example, the 76.2 meV phonon-assisted pair of onsets appearing in Figure 22 exhibits a bump that is similar to the ones already described but whose peak is positioned closer to the lower energy onset. In light of this, it would seem for those onsets in which the similarity to dN_v/dE was most apparent, the electron-photon and electron-phonon coupling between the valence band maximum and conduction band minimum is most nearly constant in the vicinity of these extrema.

It was also supposed that a similar comparison could be made to the avoided crossing seen in Figure 37 between the second lowest and third lowest valence bands. At this point, however, only a preliminary effort has been made, and this has so far been unsuccessful. In this case the energy range over which the avoided crossing occurs is significantly larger than it was in the previous case, owing to the larger separation of this pair of bands at their maxima. It is therefore expected that if this does give rise to any features in the absorption spectrum that they will be considerably broader than the ones above. As will be seen in the next section, there are indeed some rather broad features in the wavelength modulated absorption spectrum that lie higher in energy than those that occur within the first ≈ 80 meV of the lowest energy absorption onset. These might be associated with the absorption due to free excitons whose hole occupies the spin-orbit split-off valence band in the vicinity of the avoided crossing shown in Figure 37. However, in this work these have been identified with excitons whose hole occupies the crystal field split-off valence band (EX_{cf}) or whose electron occupies the second lowest conduction band (EX_2).

5.6 ABSORPTION DUE TO CRYSTAL FIELD SPLIT-OFF VALENCE BAND AND SECOND LOWEST CONDUCTION BAND

In Figures 21 and 22 it was shown that, within the first 80 meV or so of the fundamental absorption edge, the wavelength modulated absorption spectrum contained a dense multitude of features that could each be attributed to the phonon-assisted creation of two classes of excitons, EX_1 and EX_{so} : both with their electron localized to the lowest conduction band minimum (CBM) but with the former having its hole localized to the uppermost valence band maximum (VBM) and the latter having its hole localized to the second highest VBM which is split off from the other due to spin-orbit interaction. Band structure calculations for 4H SiC indicate that there might be other classes of excitons that would produce additional onsets of absorption [12, 13, 14, 11, 15, 56]. In this section we will examine the as-yet unidentified features in the wavelength modulated absorption spectrum that might be attributed to two such classes of excitons, referred to here as EX_{cf} and EX_2 : The first class of exciton has its electron occupying the lowest CBM and its hole occupying the *third highest* VBM, which lies at the same point Γ as the top two but is lower in energy by an amount referred to as the crystal field splitting Δ_{cf} . The second has its hole occupying the topmost VBM while its electron occupies the second lowest CBM, which band structure calculation show lies at the same point M as the lowest conduction band [15, 14, 17].

Since each of these excitons consists of an electron at an M-point minimum and a hole at a Γ -point maximum, the same set of principal phonons will be involved in the associated indirect absorption onsets. As with the EX_1 and EX_{so} excitons, these should occur at the threshold photon energies $\hbar\omega = E_{gx} + \hbar\Omega$, where E_{gx} is the exciton bandgap for the particular exciton and $\hbar\Omega$ is the principal phonon energy involved in the onset. If $E_x^{(cf)}$ and $E_x^{(2)}$ are the binding energies of excitons EX_{cf} and EX_2 , then their corresponding exciton bandgaps are:

$$\begin{aligned}
 E_{gx}^{(cf)} &= E_g + \Delta_{cf} - E_x^{(cf)} \\
 &= (E_g - E_x^{(1)}) + \Delta_{cf} + (E_x^{(1)} - E_x^{(cf)}) \\
 &= E_{gx}^{(1)} + \Delta_{cf} + (E_x^{(1)} - E_x^{(cf)}) \equiv E_{gx}^{(1)} + \Delta'_{cf}
 \end{aligned} \tag{5.9}$$

$$\begin{aligned}
E_{gx}^{(2)} &= E_g + \Delta_{12} - E_x^{(2)} \\
&= (E_g - E_x^{(1)}) + \Delta_{12} + (E_x^{(1)} - E_x^{(2)}) \\
&= E_{gx}^{(1)} + \Delta_{12} + (E_x^{(1)} - E_x^{(2)}) \equiv E_{gx}^{(1)} + \Delta'_{12},
\end{aligned} \tag{5.10}$$

where $E_x^{(1)}$ and $E_{gx}^{(1)} = 3.266$ eV (determined in Section 5.3) are the binding energy and exciton bandgap of the lowest energy exciton, EX_1 , and Δ_{12} we define to be the energy separation between the two lowest CBM. We expect from these results that the set of phonon-assisted absorption onsets due to EX_{cf} and EX_2 should be offset to higher energy from those due to EX_1 by an amount equal to $\Delta'_{cf} \approx \Delta_{cf}$ and $\Delta'_{12} \approx \Delta_{12}$, assuming the binding energies are not so different between the different classes of excitons. For this reason the measurement range in this work was extended beyond what was covered in the most recent study on 4H SiC [5] to $\hbar\omega = 3.6$ eV. An overview of the entire region covered is given in Figures 41 and 42, which also include the parts of the spectrum shown earlier in figures 21 and 22. Like figures 21 and 22, they are composed from several measurements over smaller wavelength intervals and for different samples, with each having been scaled an amount necessary to produce an unbroken curve.

It is seen that in either of the two polarized spectra there is a stark contrast between the regions lying either above or below $\hbar\omega \approx 3.38$ eV: whereas the lower energy region consists of many sharp onsets that were assigned earlier to excitons EX_1 and EX_{so} , the higher energy region exhibits much broader features that are also fewer in number (note that the noise level is also visible in the figures). This is a generic property of the part of the absorption spectrum associated with higher energy excitons. It was discussed, for example, in the case of the exciton associated with the lower spin-orbit split-off valence band in germanium [91, 92]. In the absorption and reflectivity spectra of the hexagonal materials ZnO [93] and CdS [94] (both direct gap semiconductors), the features associated with the crystal field split-off valence band were also significantly broader than those due to the upper valence bands. Several other instances have been reported in the literature for other materials, and the common interpretation among them is that the energy levels of the associated excitons overlap with the energy continuum of the lower-lying excitons, as shown schematically in Figure 43. It is argued that if there is an efficient mechanism by which the higher energy

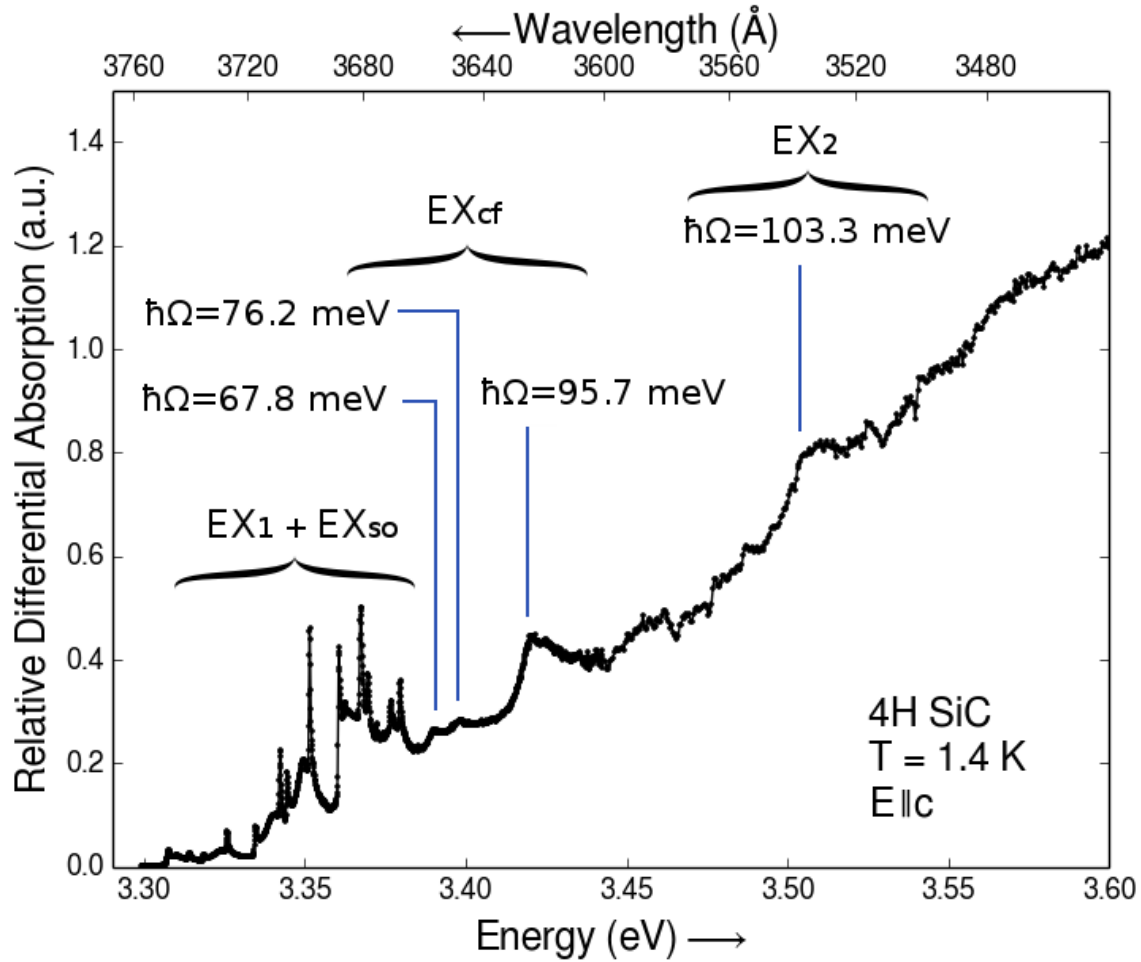


Figure 41: Overview of wavelength modulated absorption measurements in 4H SiC covering the range $\hbar\omega = 3.3\text{--}3.6$ eV for $\mathbf{E} \parallel \hat{c}$. The region 3.3–3.38 eV is densely populated by sharp onsets due to the lowest-lying excitons, referred to in the text as EX_1 and EX_{so} . The broader absorption onsets at higher photon energies have their positions marked, and have been identified with either of two higher energy excitons, EX_{cf} and EX_2 . These differ from the lowest energy excitons EX_1 and EX_{so} in that their electron and hole occupy more widely separated valence and conduction band extrema, and so their associated features in the absorption spectrum are necessarily offset to higher photon energies. The smaller peaks appearing in the ranges $\hbar\omega \approx 3.43\text{--}3.49$ eV and $3.51\text{--}3.6$ eV are not reproduced in other spectra.

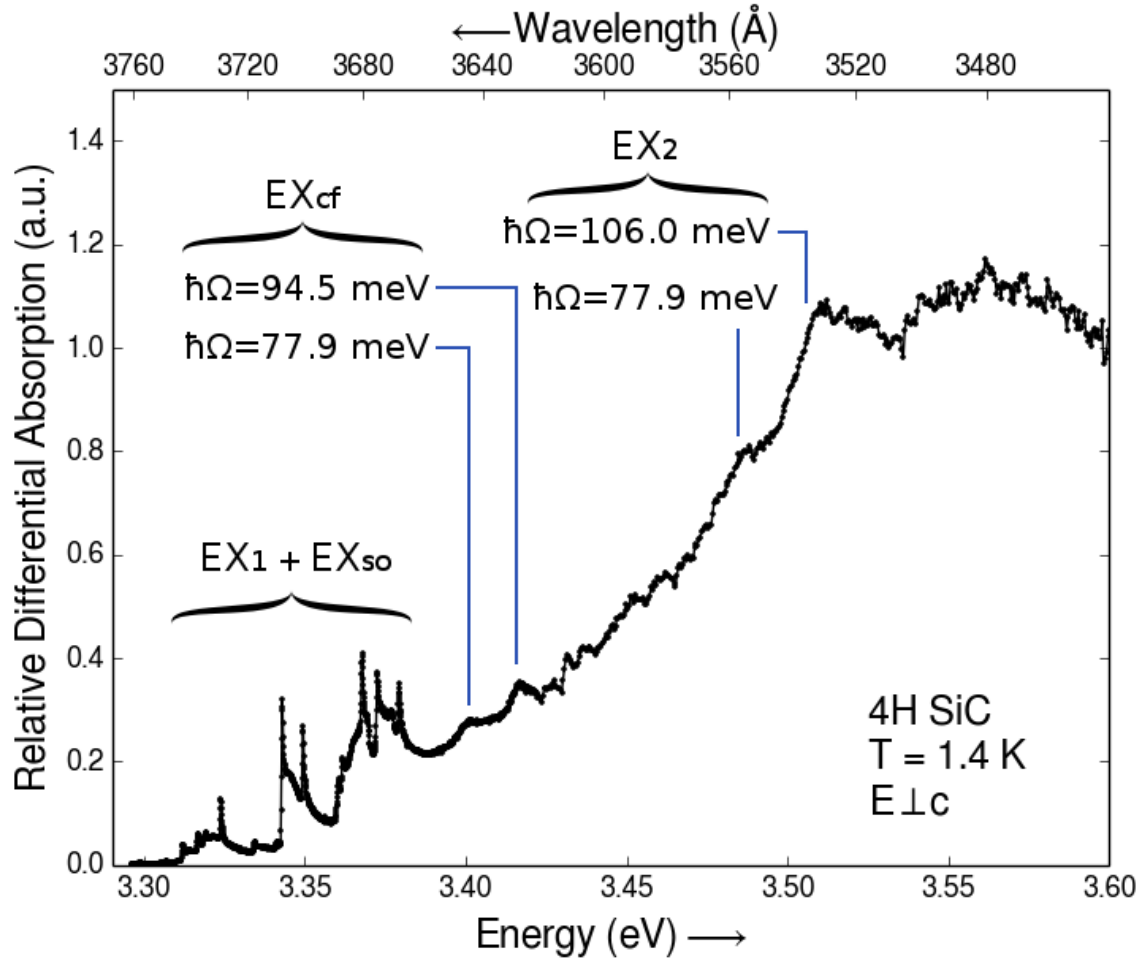


Figure 42: Same as for Figure 41 but with the spectrum polarized $\mathbf{E} \perp \hat{c}$. Note that the rounding off of the spectrum at $\hbar\omega \approx 3.56$ eV is an experimental artifact. It results from parts of the beam missing the sample and still reaching the detector. The smaller peaks appearing in the ranges $\hbar\omega \approx 3.42$ – 3.48 eV and 3.51 – 3.6 eV are not reproduced in other spectra.

exciton could decay to one of the continuum states (say, by scattering with phonons), the resulting lifetime reduction should be accompanied by an observed spectral broadening [92].

Four of the major features in this part of the absorption spectrum have been highlighted in the $\mathbf{E} \parallel \hat{c}$ polarized measurements (Figure 41) and another four have been highlighted in the $\mathbf{E} \perp \hat{c}$ polarized measurements (Figure 42). Each of these has been adequately fit to the same functional form (5.1) as for the lower energy onsets, but with the broadening parameter η found to be about a factor of 10 larger, in general ($\eta > 1$ meV compared to $\eta \approx 0.2$ meV, the latter likely being limited by instrumental resolution). The numbers which label the features are the onset energies determined from the same fit. As these absorption onsets are generally much broader and weaker than their counterparts at the low energy part of the spectrum, these onset energies are determined to somewhat lower precision from the fits (~ 0.5 meV as opposed to ~ 0.1 meV or less for the sharper onsets at lower energies). Since there is some imprecision in the wavelength calibration of the data as well (~ 0.3 – 1 Å or ~ 0.3 – 0.1 meV energy precision), the onset energies for these features are given to the nearest 1 meV.

More detailed views of some of these features are shown in figures 44 and 45 alongside some other weaker ones. These other features ($\hbar\omega = 3.457, 3.461, 3.469, 3.478, 3.452, 3.459$ eV) are seen to reproduce for the different samples shown, however they have not been reproduced for all measurements in this wavelength interval. These might not originate from the samples themselves but rather from small features in the spectral profile of the light incident on the sample, as described in Section 4.1.3. This so far has not been verified, since both the light source and diffraction gratings were different for those measurements than those in the current configuration (2400 lines/mm ruled gratings were replaced with 4320 lines/mm holographic gratings, and the 150 W xenon lamp was replaced with a 1000 W xenon lamp). These features will therefore be neglected in the following discussion.

In order to identify the main features in this part of the absorption spectrum, essentially the same procedure was followed as in the assignment of the lower energy onsets (see Section 5.3). Because these features are generally much broader than those associated with EX_1 and EX_{so} , no consideration was given for the fourfold splittings predicted in the group theory analysis of Section 3.2 despite these having been shown to hold for the excitons EX_{cf} and

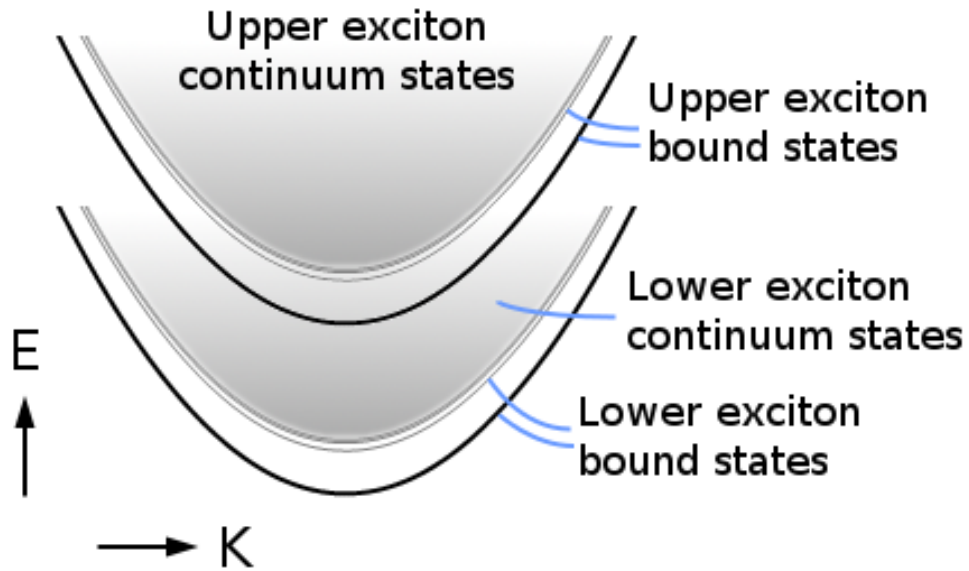


Figure 43: A scheme is shown by which the energy levels of a higher energy exciton may be broadened due to overlap with the energy levels of a lower energy exciton. The solid lines represent bound states of the electron-hole pair while the regions of graded color represent a continuum of states in which the electron and hole are free from their mutual attraction. For the lower energy exciton, the conduction band and valence band extrema lie closer together in energy than the corresponding pair for the other exciton, whose energy bands are therefore higher. If the upper exciton bands are positioned as shown in the figure, its bound states will overlap with the continuum states of the lower exciton. If there is a means for the upper exciton bound states to decay to the continuum states, the features in the absorption spectrum due to the upper exciton may become both weaker and broader than those corresponding to the lower exciton.

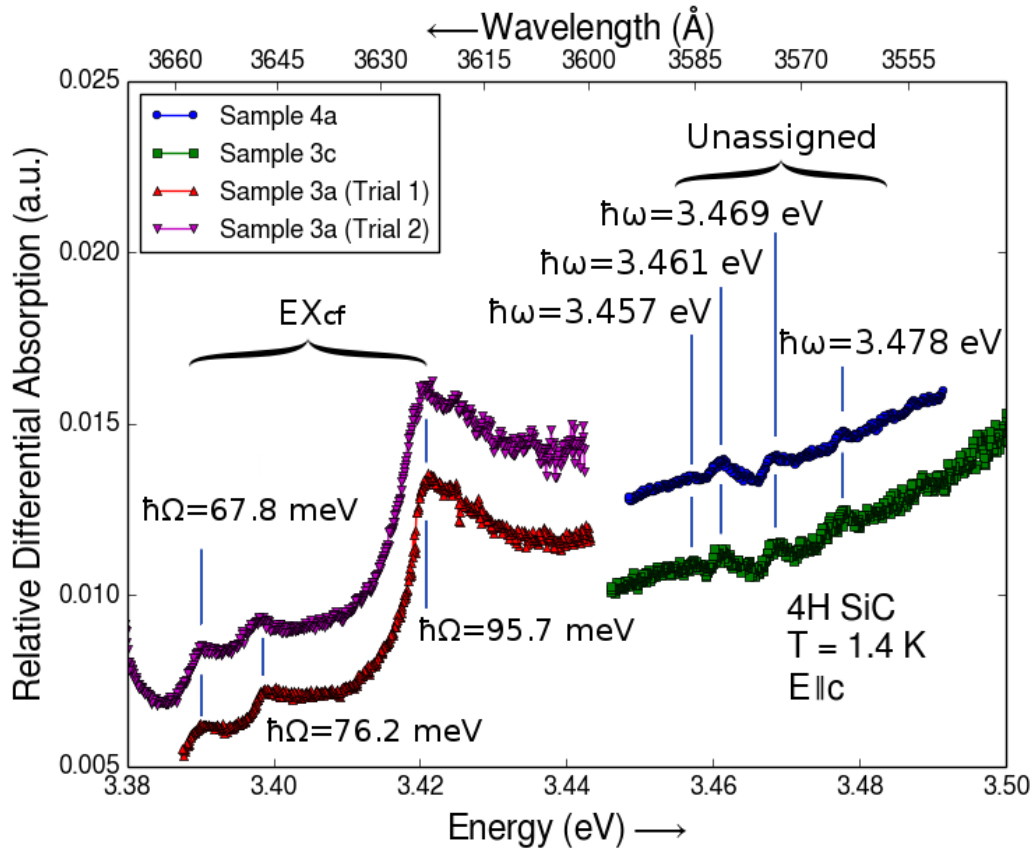


Figure 44: Detailed view of the $\mathbf{E} \parallel \hat{c}$ polarized absorption spectrum in the range 3.38–3.5 eV. Four spectra are shown: two are separate trials for a single boule sample (Sample 3a, 0.5 mm thick) and the same wavelength interval, and the other two are measurements over the same wavelength interval using two distinct samples cut from the same boule (Sample 3c, 0.25 mm thick; Sample 4a, 0.14 mm thick). All absorption onsets which reproduce for the cases shown are labeled by the photon energy at their onset. The four features seen at higher energies have reproduced for the two cases shown, but have not reproduced in the latest configuration of the experimental apparatus, which has different diffraction gratings and a higher power xenon lamp.

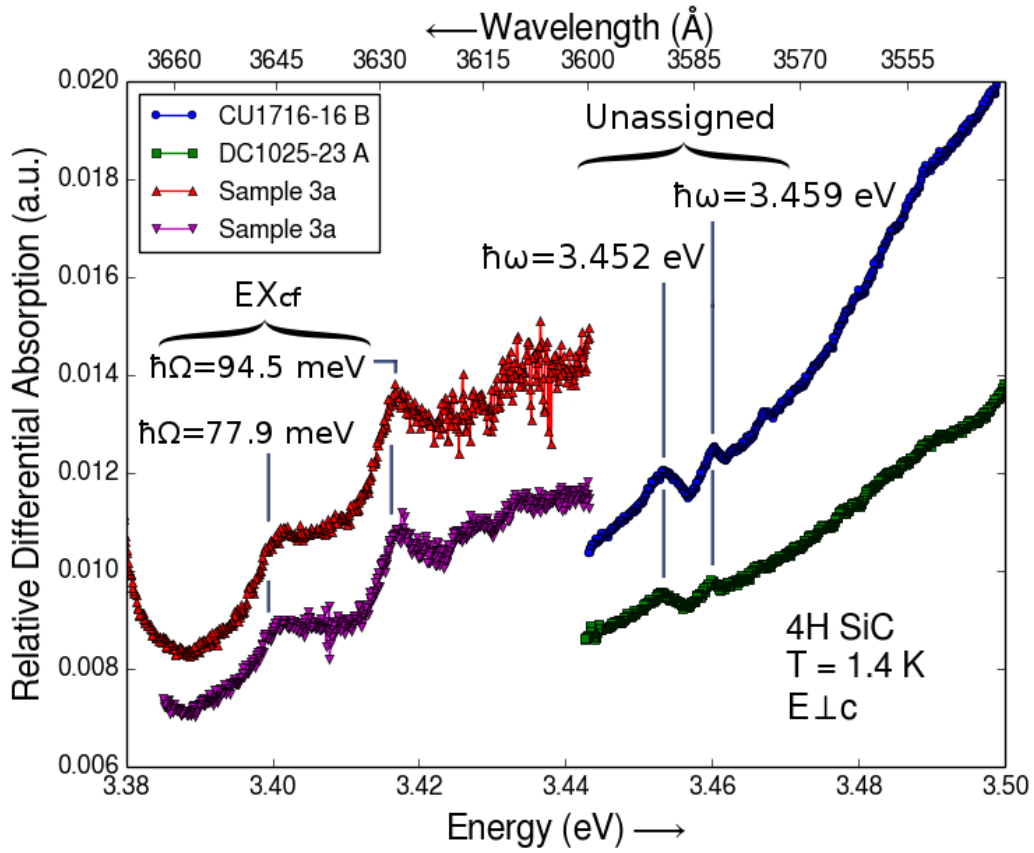


Figure 45: The same wavelength interval is shown as for Figure 44 but with the incident light polarized $\mathbf{E} \perp \hat{c}$. The four spectra shown here are: two are separate trials for a single boule sample (Sample 3a, 0.5 mm thick) and the same wavelength interval, and the other two are measurements over the same wavelength interval using two independent, epitaxial layers with their substrates removed (CU1716-16 B, 0.23 mm thick; DC1025-23 A, 0.11 mm thick). All of the absorption onsets which have been reproduced for the cases shown are labeled by the photon energy at their onset, but the four features seen at higher energies have not been reproduced in the latest configuration of the experimental apparatus, which has different diffraction gratings and a higher power xenon lamp.

EX₂ as well. In other words, for the two exciton bands associated with EX_{cf} and EX₂ and pictured in Figure 6, the finely spaced sub-bands highlighted in the figure were presumed to be indistinguishable from each other, at least insofar as could be determined by their associated absorption onsets. Given that the selection rules derived for the case without spin succeeded in identifying the principal phonons involved in the absorption onsets of both EX₁ and EX_{so}, it was assumed that a similar derivation would apply in this case as well. These are obtained in an analogous way to the group theory analysis given in Section 3.2: the products $\Gamma^{(\omega)} \otimes M^{(\Omega)}$ are sought which contain the same symmetry representations as are contained in the exciton's symmetry representation, $M^{(Ex)} = M^{(e)} \otimes \Gamma^{(h)}$ (the symmetry of the exciton's envelope function has been assumed fully symmetric as was done in Section 3.2). With spin left out, we take the electron and hole symmetries to be the single group representations of the valence and conduction band extrema which they occupy (see Table 3):

$$M_{cf}^{(Ex)} = M_4 \otimes \Gamma_1 = M_4 \quad (5.11)$$

$$M_2^{(Ex)} = M_1 \otimes \Gamma_5 = M_1 \otimes (\Gamma_2 \oplus \Gamma_4) = \Gamma_2 \oplus \Gamma_4 \quad (5.12)$$

For an allowed transition associated with exciton EX_{cf} to occur, it is therefore necessary to have the representation M₄ contained in the product $\Gamma^{(\omega)} \otimes M^{(\Omega)}$. For the exciton EX₂, those products containing either M₂ or M₄ will give rise to an allowed transition. In general, it is found that for the crystal field split-off exciton EX_{cf}, phonons of symmetry M₁ and M₃ could contribute to absorption for $\mathbf{E} \perp \hat{c}$, and for $\mathbf{E} \parallel \hat{c}$ only those phonons of symmetry M₄ could contribute. For exciton EX₂ it was found that for $\mathbf{E} \perp \hat{c}$ both M₁ and M₃ symmetry phonons could contribute, and for $\mathbf{E} \parallel \hat{c}$ both M₂ and M₄ symmetry phonons could contribute. These results are summarized in Table 7 along with the selection rules applicable to the excitons EX₁ and EX_{so}.

It is seen from the table that the selection rules for EX_{cf} and EX₂ are nearly opposite to the ones which were found to apply for the lower energy excitons, EX₁ and EX_{so}. In other words, a principal phonon that was found to participate in the $\mathbf{E} \parallel \hat{c}$ polarized absorption and emission spectra of EX₁ will now participate in the absorption spectrum polarized $\mathbf{E} \perp \hat{c}$ when excitons EX_{cf} and EX₂ are involved, and vice versa. The exception occurs for EX_{cf},

Table 7: The symmetries of the phonons for which indirect transitions may occur are shown according to the polarization of the incident light ($\mathbf{E} \parallel \hat{c}$ or $\mathbf{E} \perp \hat{c}$) and the particular exciton involved (EX_1 , EX_{so} , EX_{cf} , EX_2). The selection rules are those derived in Section 3.2 with spin neglected

	$\mathbf{E} \parallel \hat{c}$	$\mathbf{E} \perp \hat{c}$
EX_1	M_1, M_3	M_2, M_4
EX_{so}	M_1, M_3	M_2, M_4
EX_{cf}	M_4	M_1, M_3
EX_2	M_2, M_4	M_1, M_3

for which M_2 phonons are entirely forbidden from either polarization. Before identifying the unknown absorption onsets, it was not presumed beforehand which of the known principal phonon energies correspond to these particular symmetries (note that the correspondences made earlier in Table 5 of Section 5.4 are to be considered tentative). Also, since only 4 of the 24 principal phonons in 4H SiC have M_2 symmetry (see (3.19)), this exception was not taken into consideration.

With account made for the above selection rules, assignments were made using a similar strategy to the one used for the lower energy part of the absorption spectrum. For instance, in the assignment of the features in the $\mathbf{E} \parallel \hat{c}$ absorption spectrum, the positions in the $\mathbf{E} \perp \hat{c}$ emission lines were mirrored about $E_{gx}^{(1)} = 3.266$ eV and subsequently shifted by an amount ΔE into the vicinity of the unidentified features, with the shift introduced to account for the offsets (5.9) and (5.10) of the exciton bandgaps $E_{gx}^{(cf)}$ and $E_{gx}^{(2)}$ from $E_{gx}^{(1)}$. As was the case earlier with the pair of excitons EX_1 and EX_{so} , a second copy of the emission lines was reflected about $E_{gx}^{(1)}$ and shifted by some other amount $\Delta E'$ into this vicinity to account for all possible indirect transitions for both EX_{cf} and EX_2 simultaneously. By visual inspection, ΔE and $\Delta E'$ could be determined when the mirrored and shifted LTPL spectra best aligned with the full set of unidentified absorption onsets. In addition, for each mirrored and shifted emission line matched to a particular absorption onset, its associated principal

phonon (determined in Section 5.3) could then be identified with that onset. A schematic view of the end result of this procedure is shown in Figure 46.

In Tables 8 and 9 are shown the summarized results of the assignments to excitons EX_{cf} and EX_2 . It is found that the exciton bandgap for EX_{cf} is 3.322 ± 0.002 eV and 3.402 ± 0.002 eV for EX_2 . The choice to identify one bandgap with EX_{cf} and not EX_2 would seem somewhat arbitrary given that the above procedure does not consider what energy bands are occupied by the electron and hole (only their energy separation). Ultimately, however, the identification was made using the relationship mentioned at the beginning of this section between the offsets in the exciton bandgaps and the energy separations Δ_{cf} and Δ_{12} in the electronic band structure. From Table 8 we find $\Delta'_{cf} = E_{gx}^{(cf)} - E_{gx}^{(1)} = (3.322 \pm 0.002)$ eV - (3.266 ± 0.001) eV = 56 ± 3 meV, while band structure calculations place the crystal field splitting in the range 56–74 meV [11, 12, 14, 15]. From table 9 we find $\Delta'_{12} = E_{gx}^{(2)} - E_{gx}^{(1)} = (3.402 \pm 0.002)$ eV - (3.266 ± 0.001) eV = 136 ± 3 meV, which compares well to the calculated value for $\Delta_{12} = 120$ [15, 14, 17]. This latter value is also well-supported by room temperature absorption measurements [16] and ballistic electron emission microscopy measurements [17, 18], which both report $\Delta_{12} = 140$ meV.

Despite the strong agreement, however, it must be stressed that the assignments given in tables 8 and 9 are tentative, at most. With the absorption onsets here being generally weaker, broader, and much fewer in number than was the case for the low energy part of the spectrum, the procedure followed above is far too flexible to lead to one set of assignments that is appreciably better than others. From Figure 46 it is clear that many different sets of assignments are possible, and some of these may even be more optimal than the one chosen here (in terms of how well the reflected emission lines line up with the absorption onsets). A more sophisticated technique than visual inspection would likely help matters, but only to an extent. What is needed most of all in this part of the absorption spectrum is greater stability and reproducibility in its measurement so that a larger number of potentially weak absorption onsets may be discovered.

Because the samples used here are typically very thin ($\sim 100 \mu\text{m}$) in this wavelength region, the measurements are acutely sensitive to interference from various external sources. As detailed in Section 4.1.3, one of these is the wavelength variation of the incident light

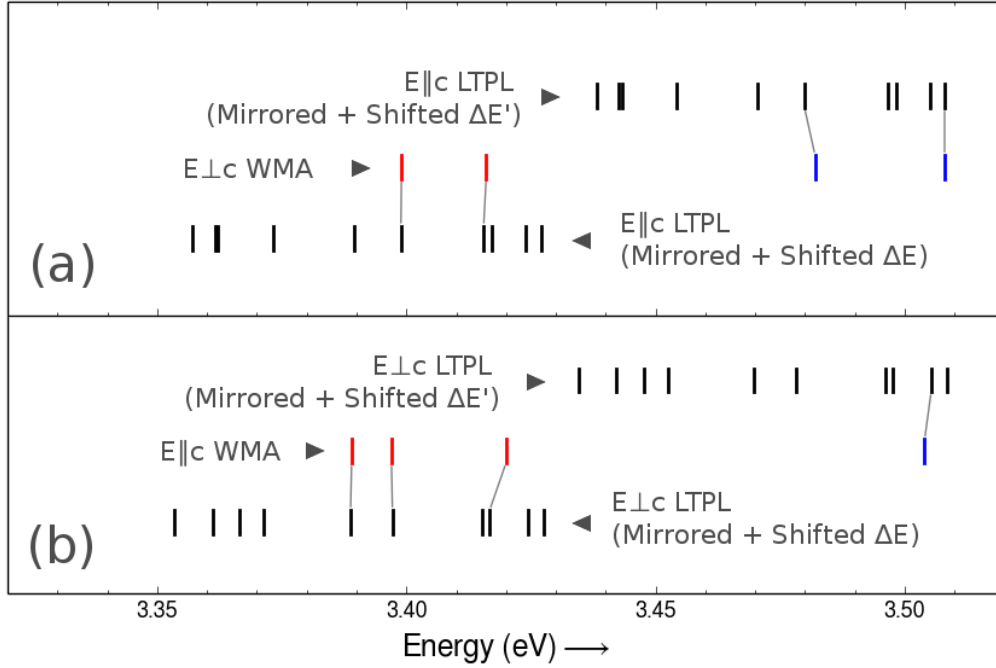


Figure 46: Visualization of the assignments given to several phonon-assisted absorption onsets in the wavelength modulated absorption (WMA) spectrum due to either of two excitons: one with its electron in the *lowest* conduction band minimum and its hole in the crystal field split-off valence band maximum (exciton EX_{cf}) or the other with its electron occupying the *second lowest* conduction band minimum and its hole in the *topmost* valence band maximum (exciton EX_2). The positions of these features in the correspondingly polarized spectra are marked in (a) “ $\mathbf{E} \perp \hat{c}$ WMA” and in (b) “ $\mathbf{E} \parallel \hat{c}$ WMA.” A similar procedure to the one visualized in Figure 27 is carried out to assign these indirect absorption onsets to the principal phonons involved in the low temperature photoluminescence (LTPL). Here, however, the comparison is made to the LTPL of the opposite polarization to account for the difference in selection rules for excitons EX_{cf} and EX_2 compared to the lowest energy exciton (EX_1), which is involved in the LTPL spectrum. The shifts ΔE and $\Delta E'$ are to account for the offsets of the bandgaps for these two excitons from that of EX_1 .

Table 8: Assignments are given to the highlighted absorption onsets from Figures 41 and 42 according to the method described in the text and shown graphically in Figure 46. The left-most column gives the photon energy $\hbar\omega^{(a)}$ of each particular absorption onset (as determined by the fit to (5.1)), whereas the two middle columns give the assigned phonon energy $\hbar\Omega$ and the calculated bandgap $E_{gx}^{(cf)} = \hbar\omega^{(a)} - \hbar\Omega$ of the exciton. The offset $\Delta'_{cf} = E_{gx}^{(cf)} - E_{gx}^{(1)}$ of this bandgap from that of the lowest-lying exciton is given in the right-most column, and from (5.9) is related the crystal field splitting of the uppermost valence bands.

	$\hbar\omega^{(a)}$	$\hbar\Omega$ (meV)	$E_{gx}^{(cf)}$ (meV)	Δ'_{cf} (meV)
E \hat{c}				
	3.389	67.8	3.321	55
	3.397	76.2	3.321	55
	3.420	95.7	3.324	58
E \perp \hat{c}				
	3.399	77.9	3.321	55
	3.416	94.5	3.322	56

Table 9: Same as for Table 8 but now with assignments given to the exciton whose electron lies in the second lowest conduction band minimum. The quantity $\Delta'_{12} = E_{gx}^{(2)} - E_{gx}^{(1)}$ likewise gives the offset of this exciton's bandgap from that of the lowest-lying exciton, and from (5.10) is related to the energy separation between the two lowest-lying conduction band minima.

	$\hbar\omega^{(a)}$	$\hbar\Omega$ (meV)	$E_{gx}^{(2)}$ (meV)	Δ'_{12} (meV)
E \hat{c}				
	3.504	103.3	3.401	135
E \perp \hat{c}				
	3.482	77.9	3.404	138
	3.508	106.0	3.402	136

itself, which may compete with the small changes in transmission due to the sample. Another has to do with small irregularities in the sample thickness over its illuminated cross-section. Since the measurement is proportional to the sample's thickness (see (4.4)) even very small variations may become important for thinner samples. If the beam is nonuniform, the measurement's insensitivity to spatial and temporal intensity fluctuations of the light source may be greatly diminished, as described in Section 4.3. Similarly, very small mechanical drifts of the sample while in the path of the beam could produce a similar effect. The double beam arrangement discussed in Section 4.1.3 has been implemented as a first step towards canceling out the wavelength dependence of the light source, but a strategy to address these other concerns has not yet been devised. These would need to be overcome in future attempts to measure this part of the absorption spectrum or to extend the measurement range to higher energies.

APPENDIX A

INDIRECT, HYDROGENIC EXCITON WAVEFUNCTION

The objective here is to give an explicit form for the hydrogenic exciton wavefunction to make its symmetry properties more apparent and to assist in the derivation of optical selection rules. We have the result [19, 21] from the effective mass approximation for an indirect, hydrogenic exciton that the envelope function has the form:

$$\Phi(\mathbf{r}_e, \mathbf{r}_h) = e^{i\mathbf{K}\cdot\mathbf{R}}\phi'(\mathbf{r}), \quad (\text{A.1})$$

where \mathbf{K} for now will just be considered an index, $\mathbf{R} = (m_e\mathbf{r}_e + m_h\mathbf{r}_h)/(m_e + m_h)$ is the exciton center of mass, and $\mathbf{r} = \mathbf{r}_e - \mathbf{r}_h$ is the electron-hole separation. The function $\phi'(\mathbf{r})$ is defined by:

$$\phi'(\mathbf{r}) = e^{i(m_h\mathbf{K}_c + m_e\mathbf{K}_v)\cdot\mathbf{r}/M}\phi_{nlm}(\mathbf{r}), \quad (\text{A.2})$$

where $M = m_e + m_h$ is the exciton's total mass, \mathbf{K}_c is the wavevector at the conduction band minimum, \mathbf{K}_v is the wavevector at valence band maximum, and $\phi_{nlm}(\mathbf{r})$ is a hydrogen-like orbital with the effective Bohr radius a_x given earlier (see (3.10)). The prefactor to $\phi_{nlm}(\mathbf{r})$ is introduced for the transformation from equation (3.4) to (3.7). The overall function $\Phi(\mathbf{r}_e, \mathbf{r}_h)$ is defined as the Fourier transform of the coefficients $C_{\mathbf{k}_e, \mathbf{k}_h}$ appearing in the expansion of the exciton wavefunction (3.1) [21, 19]:

$$\Phi(\mathbf{r}_e, \mathbf{r}_h) = \sum_{\mathbf{k}_e, \mathbf{k}_h} C_{\mathbf{k}_e, \mathbf{k}_h} e^{i(\mathbf{k}_e\cdot\mathbf{r}_e + \mathbf{k}_h\cdot\mathbf{r}_h)}. \quad (\text{A.3})$$

If we take the inverse Fourier transform of (A.1) we obtain the coefficients:

$$\begin{aligned}
C_{\mathbf{k}_e, \mathbf{k}_h} &= \frac{1}{v^2} \int \int d^3 r_e d^3 r_h e^{i\mathbf{K} \cdot \mathbf{R}} \phi'(\mathbf{r}) e^{-i(\mathbf{k}_e \cdot \mathbf{r}_e + \mathbf{k}_h \cdot \mathbf{r}_h)} \\
&= \frac{1}{v^2} \int \int d^3 R d^3 r e^{i\mathbf{K} \cdot \mathbf{R}} \phi'(\mathbf{r}) e^{-i(\mathbf{k}_e + \mathbf{k}_h) \cdot \mathbf{R}} e^{-i(m_h \mathbf{k}_e - m_e \mathbf{k}_h) \cdot \mathbf{r}/M} \\
&= \frac{1}{v} \delta_{\mathbf{K}, \mathbf{k}_e + \mathbf{k}_h} \int d^3 r \phi_{nlm}(\mathbf{r}) e^{i[m_e(\mathbf{K}_v + \mathbf{k}_h) + m_h(\mathbf{K}_c - \mathbf{k}_e)] \cdot \mathbf{r}/M} \\
&= \delta_{\mathbf{K}, \mathbf{k}_e + \mathbf{k}_h} C'_{\mathbf{q}(\mathbf{k}_e, \mathbf{k}_h)}
\end{aligned} \tag{A.4}$$

In the second line we have changed the integration variables from \mathbf{r}_e and \mathbf{r}_h to \mathbf{r} and \mathbf{R} (note that the corresponding Jacobian is unity) and in the third line we have used:

$$\int d^3 R e^{i(\mathbf{K} - \mathbf{k}_e - \mathbf{k}_h) \cdot \mathbf{R}} = v \delta_{\mathbf{K}, \mathbf{k}_e + \mathbf{k}_h}, \tag{A.5}$$

where v is the volume of the solid. In the last line in (A.4) the $C'_{\mathbf{q}(\mathbf{k}_e, \mathbf{k}_h)}$ are the Fourier coefficients of ϕ_{nlm} , with $\mathbf{q}(\mathbf{k}_e, \mathbf{k}_h) = -[m_e(\mathbf{K}_v + \mathbf{k}_h) + m_h(\mathbf{K}_c - \mathbf{k}_e)]/M$. For an $n = 1$ S orbital $\phi_1(\mathbf{r}) \propto e^{-r/a_x}$ we have:

$$\begin{aligned}
C'_{\mathbf{q}} &= \frac{1}{v} \int d^3 r e^{-r/a_x} e^{-i\mathbf{q} \cdot \mathbf{r}} \\
&= \frac{2\pi}{v} \int_0^\pi d\theta \sin \theta \int_0^\infty dr r^2 e^{-(1/a_x + iq \cos \theta)r} \\
&= \frac{4\pi}{v} \int_0^\pi d\theta \sin \theta (1/a_x + iq \cos \theta)^{-3} \\
&= \frac{8\pi/a_x v}{[(1/a_x)^2 + q^2]^2}.
\end{aligned} \tag{A.6}$$

If the exciton is truly weakly bound such that a_x is large, these coefficients should be significant only for a small range about $\mathbf{q} = \mathbf{0}$. Using the exciton Bohr radius $a_x = 20$ Å found earlier in section 3, it is seen from Figure 47 that this is reasonably true for 4H SiC. Along with the Kronecker delta $\delta_{\mathbf{K}, \mathbf{k}_e + \mathbf{k}_h}$ this results in the largest contribution to the exciton wavefunction from those Bloch functions with:

$$\begin{aligned}
\mathbf{k}_e &= \mathbf{k}_e^o \equiv [m_e(\mathbf{K} + \mathbf{K}_v) + m_h \mathbf{K}_c]/M \\
\mathbf{k}_h &= \mathbf{k}_h^o \equiv [m_h(\mathbf{K} - \mathbf{K}_c) - m_e \mathbf{K}_v]/M
\end{aligned} \tag{A.7}$$

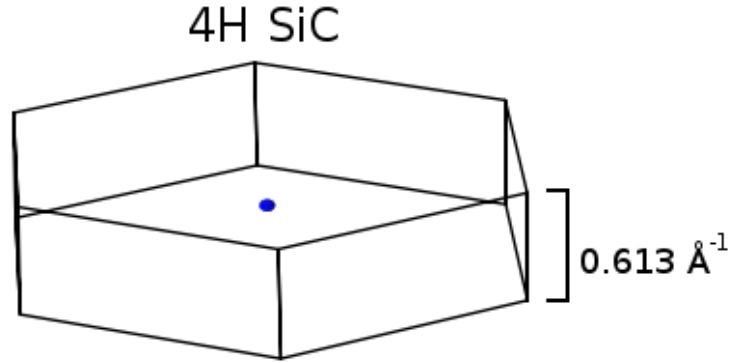


Figure 47: The envelope function of the exciton takes the form of a hydrogenic orbital with effective Bohr radius a_x . Its Fourier components $C'_{\mathbf{q}}$ are largest for $\mathbf{q} = \mathbf{0}$ and begin to fall off for $q \approx 1/a_x$, as shown in (A.4). Using $a_x = 20 \text{ \AA}$ found in section 3.1, contour plots for these coefficients are shown within the Brillouin zone of 4H SiC (using the lattice parameters $a = 3.079 \text{ \AA}$, $c = 10.254 \text{ \AA}$ [37]). The contour shown is that for which the coefficients reach their half-maximum value, and appears as a sphere at the center of the hexagonal prism (since $C'_{\mathbf{q}}$ depends only on the magnitude q). It is seen that the expansion coefficients are fairly well-confined to the center of the Brillouin zone, as required by the effective mass approximation.

If the periodic parts of the electron and hole Bloch functions $u_{c,\mathbf{k}_e}(\mathbf{r}_e)$ and $u_{v,\mathbf{k}_h}(\mathbf{r}_h)$ do not depend strongly on their wavevectors over this small range, they may be brought out of the expansion of Ψ_{Ex} with the replacements (A.7):

$$\begin{aligned}
\Psi_{Ex} &= \sum_{\mathbf{k}_e, \mathbf{k}_h} C_{\mathbf{k}_e, \mathbf{k}_h} \psi_{c, \mathbf{k}_e}(\mathbf{r}_e) \psi_{v, \mathbf{k}_h}(\mathbf{r}_h) \\
&= \sum_{\mathbf{k}_e, \mathbf{k}_h} \delta_{\mathbf{K}, \mathbf{k}_e + \mathbf{k}_h} C'_{\mathbf{q}(\mathbf{k}_e, \mathbf{k}_h)} e^{i\mathbf{k}_e \cdot \mathbf{r}_e} u_{c, \mathbf{k}_e}(\mathbf{r}_e) e^{i\mathbf{k}_h \cdot \mathbf{r}_h} u_{v, \mathbf{k}_h}(\mathbf{r}_h) \\
&\approx u_{c, \mathbf{k}_e^o}(\mathbf{r}_e) u_{v, \mathbf{k}_h^o}(\mathbf{r}_h) \sum_{\mathbf{k}_e, \mathbf{k}_h} \delta_{\mathbf{K}, \mathbf{k}_e + \mathbf{k}_h} C'_{\mathbf{q}(\mathbf{k}_e, \mathbf{k}_h)} e^{i(\mathbf{k}_e \cdot \mathbf{r}_e + \mathbf{k}_h \cdot \mathbf{r}_h)} \\
&\approx u_{c, \mathbf{k}_e^o}(\mathbf{r}_e) u_{v, \mathbf{k}_h^o}(\mathbf{r}_h) e^{i\mathbf{K} \cdot \mathbf{r}_h} \sum_{\mathbf{k}_e} C'_{\mathbf{k}_e - \mathbf{k}_e^o} e^{i\mathbf{k}_e \cdot \mathbf{r}}
\end{aligned} \tag{A.8}$$

In the last line we have used $\mathbf{q}(\mathbf{k}_e, \mathbf{K} - \mathbf{k}_e) = \mathbf{k}_e - \mathbf{k}_e^o$. Note that the sum over \mathbf{k}_e is to be performed over the first Brillouin zone by definition. If we allow the volume $v \rightarrow \infty$ the sum over the Brillouin zone becomes an integral:

$$\begin{aligned}
\sum_{\mathbf{k}_e} C'_{\mathbf{k}_e - \mathbf{k}_e^o} e^{i\mathbf{k}_e \cdot \mathbf{r}} &\longrightarrow \frac{v}{(2\pi)^3} \int d^3 k_e C'_{\mathbf{k}_e - \mathbf{k}_e^o} e^{i\mathbf{k}_e \cdot \mathbf{r}} \\
&= \frac{v}{(2\pi)^3} \int d^3 k_e C'_{\mathbf{k}_e} e^{i(\mathbf{k}_e + \mathbf{k}_e^o) \cdot \mathbf{r}} \\
&= \frac{v}{(2\pi)^3} e^{i\mathbf{k}_e^o \cdot \mathbf{r}} \int d^3 k_e C'_{\mathbf{k}_e} e^{i\mathbf{k}_e \cdot \mathbf{r}} \\
&= e^{i\mathbf{k}_e^o \cdot \mathbf{r}} \phi_{nlm}(\mathbf{r})
\end{aligned} \tag{A.9}$$

Note that in the last line we have assumed that the coefficients $C'_{\mathbf{k}_e}$ are negligibly small outside the Brillouin zone such that the integral can be extended to infinity. We now have for the exciton wavefunction:

$$\begin{aligned}
\Psi_{Ex} &= u_{c, \mathbf{k}_e^o}(\mathbf{r}_e) u_{v, \mathbf{k}_h^o}(\mathbf{r}_h) e^{i\mathbf{K} \cdot \mathbf{r}_h} e^{i\mathbf{k}_e^o \cdot \mathbf{r}} \phi_{nlm}(\mathbf{r}) \\
&= e^{i\mathbf{k}_e^o \cdot \mathbf{r}_e} u_{c, \mathbf{k}_e^o}(\mathbf{r}_e) e^{i\mathbf{k}_h^o \cdot \mathbf{r}_h} u_{v, \mathbf{k}_h^o}(\mathbf{r}_h) \phi_{nlm}(\mathbf{r}) \\
&= \psi_{c, \mathbf{k}_e^o}(\mathbf{r}_e) \psi_{v, \mathbf{k}_h^o}(\mathbf{r}_h) \phi_{nlm}(\mathbf{r}),
\end{aligned} \tag{A.10}$$

where in the second line we have used $\mathbf{r} = \mathbf{r}_e - \mathbf{r}_h$ and $\mathbf{K} = \mathbf{k}_e^o + \mathbf{k}_h^o$. At the minimum of the exciton energy band (i.e. where the \mathbf{K} -dependent kinetic energy term in (3.8) is zero), $\mathbf{K} = \mathbf{K}_c - \mathbf{K}_v$, $\mathbf{k}_e^o = \mathbf{K}_c$, and $\mathbf{k}_h^o = -\mathbf{K}_v$, and the electron and hole Bloch functions are exactly those corresponding to the valence and conduction band extrema (note that

the wavevector of the hole is the negative of the wavevector of the missing electron). The hydrogenic orbital is called the *envelope function*, and it is seen to give increased weight to the two Bloch functions wherever $|\mathbf{r}_e - \mathbf{r}_h| \approx 0$. An S orbital is fully symmetric under any rotation, reflection, or translation of *both* \mathbf{r}_e and \mathbf{r}_h , and so the symmetry properties of the overall wavefunction are determined entirely by the electron and hole Bloch functions in this case.

In particular, for translations $T_{\boldsymbol{\tau}} : \mathbf{r}_e \rightarrow \mathbf{r}_e - \boldsymbol{\tau}, \mathbf{r}_h \rightarrow \mathbf{r}_h - \boldsymbol{\tau}$ by the lattice vector $\boldsymbol{\tau}$ we have:

$$\begin{aligned}
\Psi_{Ex}(\mathbf{r}_e - \boldsymbol{\tau}, \mathbf{r}_h - \boldsymbol{\tau}) &= e^{i\mathbf{k}_e^{\circ} \cdot (\mathbf{r}_e - \boldsymbol{\tau})} u_{c, \mathbf{k}_e^{\circ}}(\mathbf{r}_e - \boldsymbol{\tau}) e^{i\mathbf{k}_h^{\circ} \cdot (\mathbf{r}_h - \boldsymbol{\tau})} u_{v, \mathbf{k}_h^{\circ}}(\mathbf{r}_h - \boldsymbol{\tau}) \phi_{nlm}(\mathbf{r}) \\
&= e^{i\mathbf{k}_e^{\circ} \cdot (\mathbf{r}_e - \boldsymbol{\tau})} u_{c, \mathbf{k}_e^{\circ}}(\mathbf{r}_e) e^{i\mathbf{k}_h^{\circ} \cdot (\mathbf{r}_h - \boldsymbol{\tau})} u_{v, \mathbf{k}_h^{\circ}}(\mathbf{r}_h) \phi_{nlm}(\mathbf{r}) \\
&= e^{-i(\mathbf{k}_e^{\circ} + \mathbf{k}_h^{\circ}) \cdot \boldsymbol{\tau}} \Psi(\mathbf{r}_e, \mathbf{r}_h) \\
&= e^{-i\mathbf{K} \cdot \boldsymbol{\tau}} \Psi(\mathbf{r}_e, \mathbf{r}_h)
\end{aligned} \tag{A.11}$$

The above result is the same as would apply to a generic Bloch function:

$$\psi_{n, \mathbf{k}}(\mathbf{r} - \boldsymbol{\tau}) = e^{-i\mathbf{k} \cdot \boldsymbol{\tau}} \psi_{n, \mathbf{k}}(\mathbf{r}), \tag{A.12}$$

and so, as with the Bloch functions, the symmetry properties of Ψ_{Ex} under rotations and reflections will be determined by the group of its wavevector \mathbf{K} . This remains true not only for free excitons within the simple hydrogenic model, but also for those free excitons associated with anisotropic valence and conduction bands (this results from the translational invariance under operations $T_{\boldsymbol{\tau}}$ of the Coulomb interaction between the electron and hole, which depends only on \mathbf{r}) [95]. It is therefore possible to use the symmetry properties associated with an exciton's wavevector \mathbf{K} to derive energy level splittings and selection rules even for the case in anisotropic crystals such as 4H SiC.

APPENDIX B

VALENCE BAND DENSITY OF STATES

The purpose here is to arrive at an accurate model for the three topmost valence bands in 4H SiC such that the associated density of states $N_v(E)$ may be computed and compared to the absorption spectrum. More precisely, since the wavelength modulated absorption spectrum has been measured in this work, it will be necessary to compute the energy derivative dN_v/dE and compare it directly with the measured spectrum. To begin, it is necessary to have an expression for the energy bands as a function of an arbitrary point \mathbf{k} in the Brillouin zone such that the following integral can be computed, which is proportional to the density of states for a single band $E_v(\mathbf{k})$ [90, 59]:

$$N_v(E) \propto \int \frac{dS(E)}{|\nabla E_v(\mathbf{k})|}, \quad (\text{B.1})$$

where $dS(E)$ is an infinitesimal area element in k-space within the the surface defined by $E_v(\mathbf{k}) = E$. This is to be evaluated for all three valence bands, and the contribution from each summed together to obtain the overall density of states.

The modeling of the valence bands as a function of \mathbf{k} is made possible using k·p theory, which uses symmetry arguments similar to the ones applied in section 3.2 to specify this functional dependence up to a set of adjustable parameters (see reference [31] for a general discussion of k·p theory and reference [96] for its implementation with respect to the valence bands of wurtzite structure materials). Values for these parameters have been obtained for the valence bands in 4H SiC from fits to band structure calculations from Lambrecht *et al.* [12] and Wellenhofer and Rössler (WR) [15]. The model used by WR is specified in greater

Table 10: From k·p theory, the Hamiltonian given in expression (B.2) and parameterized by $A_1 \dots A_7$, and Δ_1 may be diagonalized to produce model expressions for the top three valence bands in 4H SiC. The values values for the parameters have been obtained by the authors of reference [15] from their own fit to their band structure calculation. They are listed in atomic units. The parameter Δ_1 gives the energy separation in atomic units of the third highest valence band maximum from the topmost valence band maximum, which is the crystal field splitting. It has been re-expressed to coincide with Table 4 of the above reference, with its label changed to Δ_{cr} and its value listed in units of meV (it is also referred to as Δ_{cf} elsewhere in this work).

A_1	A_2	A_3	A_4	A_5	A_6	A_7	Δ_1	Δ_{cr} (meV)
-4.76	-0.628	-4.14	-1.11	-1.45	-1.49	0.0127	0.027	74

detail, and so their parameters are used here.

The model valence bands WR used to fit to their band structure calculation are obtained from the parameterized Hamiltonian appearing in their expression (4) (reproduced below). When diagonalized, it gives the form of the three uppermost valence bands for a hexagonal crystal in terms of the components of the wavevector \mathbf{k} and the eight parameters $A_1, A_2 \dots A_7, \Delta_1$ (Δ_1 plays the role of the crystal field splitting and is referred to by Δ_{cr} in their Table 4 and by Δ_{cf} elsewhere in this work). The values obtained by WR are reproduced in Table 10.

It must be emphasized that the models parameterized in this way make no allowance for spin-orbit interaction. For WR this was not needed to obtain the fitting parameters $A_1 \dots A_7$ and Δ_1 because their band structure calculation was not relativistic. However, given that the anomalous bumps in the absorption spectrum appear in between spin-orbit split pairs of onsets, it is necessary to extend the k·p model to incorporate spin and spin-orbit interaction. WR go on to do this with the introduction of the k·p Hamiltonian appearing in their expression (3), which is reproduced below in (B.3). With the electron spin now incorporated, this new Hamiltonian matrix is doubled in size from (B.2) and also features two additional

parameters, Δ_2 and Δ_3 , which characterize the spin-orbit interaction (compare the top left 3×3 block in (B.3) with the spin-orbit Hamiltonian given in (4) of reference [96]). We will follow suit with WR in making the choice $\Delta_2 = \Delta_3$ (see page 64 of reference [96] for an explanation) and assuming that the spin-orbit splitting is small enough that the values for the other parameters may be carried over into this new Hamiltonian.

$$H_{3 \times 3}(\mathbf{k}) = \begin{pmatrix} \Delta_1 + \lambda + \theta & -H^* & K^* \\ -H & \lambda & I^* \\ K & I & \Delta_1 + \lambda + \theta \end{pmatrix} \quad (\text{B.2})$$

$$H_{6 \times 6}(\mathbf{k}) = \begin{pmatrix} F & 0 & -H^* & 0 & K^* & 0 \\ 0 & G & \Delta & -H^* & 0 & K^* \\ -H & \Delta & \lambda & 0 & I^* & 0 \\ 0 & -H & 0 & \lambda & \Delta & I^* \\ K & 0 & I & \Delta & G & 0 \\ 0 & K & 0 & I & 0 & F \end{pmatrix} \quad (\text{B.3})$$

$$\begin{aligned} F &= \Delta_1 + \Delta_2 + \lambda + \theta, & k_+ &= k_x + ik_y, & H &= iA_6k_zk_+ - A_7k_+, \\ G &= \Delta_1 - \Delta_2 + \lambda + \theta, & \Delta &= \sqrt{2}\Delta_3, & \lambda &= A_1k_z^2 + A_2(k_x^2 + k_y^2), \\ I &= iA_6k_zk_+ + A_7k_+, & K &= A_5k_+^2, & \theta &= A_3k_z^2 + A_4(k_x^2 + k_y^2) \end{aligned} \quad (\text{B.4})$$

At this point it is necessary only to make a choice of the free parameter Δ_2 in order to accurately model the valence bands when the spin-orbit interaction is included. It is pointed out that while this characterizes the strength of the spin-orbit interaction, it *does not* give the spin-orbit splitting itself. WR choose $\Delta_2 = \Delta_{so}/3$, where $\Delta_{so} = 7$ meV is taken to reproduce the experimental measurements of the spin-orbit splitting of the valence band maximum $\mathbf{k} = \mathbf{0}$ [97, 98, 4]. This will turn out to produce a spin-orbit splitting which is too small, even when taking the measured value to be correct. Since the spin-orbit splitting is defined to be the energy separation of the top two valence bands at the point $\mathbf{k} = \mathbf{0}$, we must look for the eigenvalues of the Hamiltonian (B.3) at this point. This yields three

doubly degenerate eigenvalues which we label by E_1 , E_{so} , and E_{cf} in order of decreasing energy:

$$\begin{aligned}
E_1 &= \Delta_1 + \Delta_2 \\
E_{so} &= \frac{\Delta_1 - \Delta_2}{2} + \sqrt{\left(\frac{\Delta_1 - \Delta_2}{2}\right)^2 + 2\Delta_2^2} \\
E_{cf} &= \frac{\Delta_1 - \Delta_2}{2} - \sqrt{\left(\frac{\Delta_1 - \Delta_2}{2}\right)^2 + 2\Delta_2^2}
\end{aligned} \tag{B.5}$$

The spin-orbit splitting is then given by:

$$\Delta_{so} = E_1 - E_{so} = \frac{\Delta_1 + 3\Delta_2}{2} - \sqrt{\left(\frac{\Delta_1 - \Delta_2}{2}\right)^2 + 2\Delta_2^2} \tag{B.6}$$

Solving for Δ_2 we find:

$$\Delta_2 = \left(\frac{\Delta_1 - \Delta_{so}}{2\Delta_1 - 3\Delta_{so}}\right) \Delta_{so} \approx \frac{\Delta_{so}}{2}, \tag{B.7}$$

where in the approximation it has been assumed the spin-orbit splitting is much less than the crystal field splitting: $\Delta_{so} \ll \Delta_1$ (WR calculate the crystal field splitting Δ_1 to be 74 meV). If WR chose their parameter Δ_2 in this limit, theirs is a factor of 3/2 smaller than the correct lower limit. Since the model valence bands are meant only for qualitative comparison purposes, we take Δ_{so} to be the experimentally observed 7 meV. Strictly speaking, since this value has been measured from the absorption spectrum, this is not the spin-orbit splitting of the valence bands but the spin-orbit splitting of the exciton bands. In this case it is somewhat advantageous to use this value, since the comparison to be made is with the absorption spectrum. Using the atomic units in which the other parameters are expressed (1 Ha = 27.211 eV), we have $\Delta_{so} = 0.00026$ and from (B.7) we have $\Delta_2 = 0.00013$.

Once this value and the others given in Table 10 have been substituted into the Hamiltonian (B.3), the six eigenvalues obtained as a function of \mathbf{k} are the model expressions for the valence bands that were sought. It is seen from Figure 38 that the resulting spin-orbit splitting between the top two valence band maxima at the Γ point produces the desired 7 meV separation. From Figure 37 it is seen that, with spin now included, the three bands that were referred to earlier have now become six in number. These are grouped into three doubly degenerate bands for \mathbf{k} lying along the Γ -A axis of the Brillouin zone (in terms of the definitions (B.4) this is the k_z axis), while along perpendicular directions this degeneracy

is broken (see Figure 37). For the remainder of the discussion, this broken degeneracy will be ignored so that we consider only three of these bands which are distinct along the Γ -A direction.

With the model valence bands so obtained, it is now possible to compute the density of states and its energy derivative. Because of the complexity of the expressions for the valence bands, the integration given in (B.1) for the density of states was performed numerically. The procedure for doing so has been given in detail in reference [90], and will be outlined for this specific case here. The basic premise for the method given in [90] is to break up the region of integration in (B.1) into very many small tetrahedra such that the gradient $\nabla E_v(\mathbf{k})$ may be interpolated linearly between the vertices. The integral then becomes a sum of all of these tetrahedral cells, each one of which gives the contribution:

$$i_o(E) = \begin{cases} \frac{v}{2} \frac{(E-\varepsilon_0)^2}{(\varepsilon_1-\varepsilon_0)(\varepsilon_2-\varepsilon_0)(\varepsilon_3-\varepsilon_0)} & \varepsilon_0 \leq E \leq \varepsilon_1 \\ \frac{v}{2} \left[\frac{(E-\varepsilon_0)^2}{(\varepsilon_1-\varepsilon_0)(\varepsilon_2-\varepsilon_0)(\varepsilon_3-\varepsilon_0)} - \frac{(E-\varepsilon_1)^2}{(\varepsilon_1-\varepsilon_0)(\varepsilon_2-\varepsilon_1)(\varepsilon_3-\varepsilon_1)} \right] & \varepsilon_1 \leq E \leq \varepsilon_2 \\ \frac{v}{2} \frac{(E-\varepsilon_3)^2}{(\varepsilon_3-\varepsilon_0)(\varepsilon_3-\varepsilon_1)(\varepsilon_3-\varepsilon_2)} & \varepsilon_2 \leq E \leq \varepsilon_3, \end{cases} \quad (\text{B.8})$$

where $\varepsilon_0 \leq \varepsilon_1 \leq \varepsilon_2 \leq \varepsilon_3$ are the energies of a particular band evaluated at the four vertices, and v is the volume of that particular cell. For energies $E \leq \varepsilon_0$ or $E \geq \varepsilon_3$, i_o is defined to be zero. The energy derivative of the density of states may be evaluated as a sum over the same set of tetrahedra, but with each one giving the contribution di_o/dE :

$$\frac{di_o}{dE} = \begin{cases} v \frac{E-\varepsilon_0}{(\varepsilon_1-\varepsilon_0)(\varepsilon_2-\varepsilon_0)(\varepsilon_3-\varepsilon_0)} & \varepsilon_0 \leq E \leq \varepsilon_1 \\ v \left[\frac{E-\varepsilon_0}{(\varepsilon_1-\varepsilon_0)(\varepsilon_2-\varepsilon_0)(\varepsilon_3-\varepsilon_0)} - \frac{E-\varepsilon_1}{(\varepsilon_1-\varepsilon_0)(\varepsilon_2-\varepsilon_1)(\varepsilon_3-\varepsilon_1)} \right] & \varepsilon_1 \leq E \leq \varepsilon_2 \\ v \frac{E-\varepsilon_3}{(\varepsilon_3-\varepsilon_0)(\varepsilon_3-\varepsilon_1)(\varepsilon_3-\varepsilon_2)} & \varepsilon_2 \leq E \leq \varepsilon_3, \end{cases} \quad (\text{B.9})$$

In practice this is set up by first defining the boundaries of the k-space volume which is to be taken up by the tetrahedra. In (B.1) it is implied that the integration is to be carried out over the entire volume of the Brillouin zone. This is computationally expensive, and is to be avoided if the energy bands do not extend to all parts of the Brillouin zone for the range of energies E that are of interest. In the present case of the valence bands, it was decided that the range of interest was from $E = 0$ meV at the maximum of the topmost valence

band to about $E = -100$ meV (the k·p model valence bands obtained above were shifted uniformly by an amount $\Delta_1 + \Delta_2$ down in energy to have the top valence band maximum at $E = 0$ meV). The intent was to include the effects of all three valence band maxima, whose energies lie in this range. A sphere of radius $k_{max} = 0.1$ Bohr ($= 0.18897 \text{ \AA}^{-1}$) was then defined which enclosed every one of the modeled valence bands for the entirety of this range of energies. To improve the computational efficiency, the region was further reduced to that for which $k_z > 0$, $k_x > 0$, and $k_y < k_x/\sqrt{3}$. This is to take advantage of the symmetry of the k·p model valence bands, which are unchanged for those reflections and rotations that belong to the C_{6v} group corresponding to the Γ point.

From here a strategy must be devised to subdivide the region into tetrahedra. The method that was used here and found to be convenient was an algorithmic approach known as “marching tetrahedra” [99]. In this method, the region is first divided into a contiguous set of cubes whose sides are oriented along the k_x , k_y , and k_z axes and are all of length k_{step} , where k_{step} is chosen to be a small fraction of k_{max} and largely determines the accuracy of the calculation. From here the cubes are further subdivided into six tetrahedra, as in Figure 48. This has the advantage that the locations and orientations of all the tetrahedra may be computed on the fly, without having to store a vast register of their vertices. One simply needs to define a fixed ordering for the tetrahedra within the cubes (as shown in Figure 48) such that the location and orientation of one may be found from that of the previous one. Also, the volumes of the tetrahedra need not be calculated since they are identical for all tetrahedra.

To calculate the energies $\varepsilon_0 \leq \varepsilon_1 \leq \varepsilon_2 \leq \varepsilon_3$ at the vertices of a given tetrahedron, the wavevector \mathbf{k} at each vertex is substituted into the Hamiltonian (B.3) whose eigenvalues are then calculated (for this the Eigen family of C++ libraries was used [100]). In this case six eigenvalues—one for each valence band—would be obtained at any given vertex, and if one is interested in the contribution from a subset of those, one must know their energetic ordering (instances where two bands exchange their ordering at certain points in the Brillouin zone did not occur here, and so will not be discussed). Of the six, three eigenvalues corresponding to the bands with distinct energy maxima were stored. The eigenvalues corresponding to these same three bands were selected from each of the other vertices.

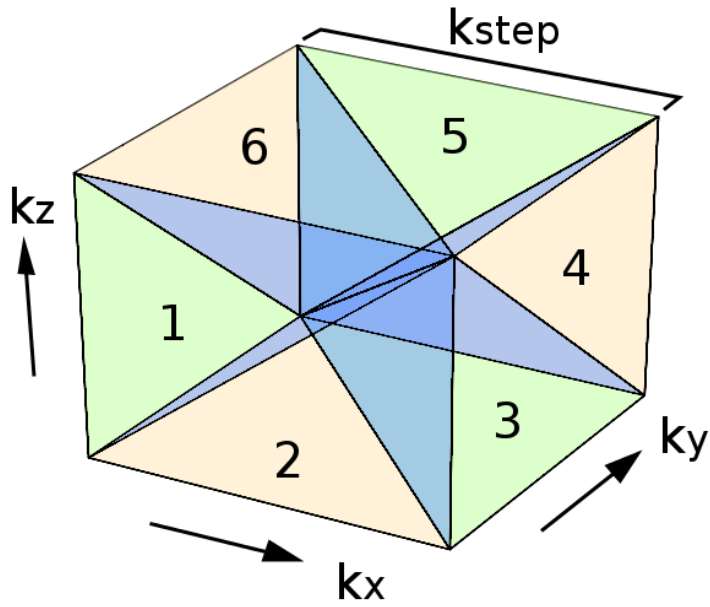


Figure 48: The numerical integration over k -space given in the text is performed by first dividing k -space into many small cubes and then further subdividing the cubes into the tetrahedra shown numbered one through six. The cube's sides are aligned with the k_x , k_y , and k_z axes and have length k_{step} chosen small enough to adequately approximate the integral.

For a fixed energy E (chosen to be in the range given earlier), the functions $i_o(E)$ and di_o/dE were evaluated for the single tetrahedron using the energies $\varepsilon_0 \leq \varepsilon_1 \leq \varepsilon_2 \leq \varepsilon_3$ evaluated at the four vertices and corresponding to the same energy band. $i_o(E)$ and di_o/dE would then be added to running sums for $N_v(E)$ and dN_v/dE , respectively. Since the total density of states was computed, this was repeated for the remaining two valence bands whose eigenvalues were stored, with the contributions from these being added to the same running sums for $N_v(E)$ and dN_v/dE . This procedure can then be repeated one tetrahedron at a time, iterating through the defined volume in some regular, pre-determined way. This completes the sum for one single energy E in the calculated $N_v(E)$ and dN_v/dE curves. To build up the rest of the desired curves the process is repeated over again at some chosen increment $E' = E + \Delta E$.

APPENDIX C

COUPLING LIGHT INTO A MONOCHROMATOR

Optical spectroscopy consists fundamentally of four things: the sample under study, a light source, a dispersive element, and a detector. For the measurements discussed in this work, the dispersive element is either a monochromator or spectrometer (the difference being that the former is equipped with a single-channel detector such as a PMT and the latter an array detector such as a CCD). In either case, light is coupled into the dispersive element through an entrance slit. The slit width, i.e. its dimension in the plane of dispersion, is a determining factor in the ultimate wavelength resolution achieved at the dispersive element's output: the narrower the slit, the higher the resolution and the easier it is to distinguish two or more closely spaced spectral features. However, along with that inevitably comes a reduction in light throughput to the detector. In such cases where the light source is weak, the intensity loss sustained from narrowing the entrance slit may outweigh the improvement in resolution, and so it becomes critically important to optimize the efficiency with which light is coupled into the monochromator or spectrometer.

For practical reasons, the light source is often some distance away from the entrance slit, and so it becomes necessary to use auxiliary optical elements to both collect the light and direct it towards the slit. A typical arrangement is to have two converging lenses between the light source and the entrance slit. The lens closest to the source (lens 1) is placed so as to collimate the light, and the other lens (lens 2) is placed at a position so as to focus the light on the entrance slit (see Figure 49). The source and the two lenses all lie along the optic axis of the monochromator, which connects the center of the entrance slit to the center of

the nearest concave mirror inside the monochromator. This can be determined by shining a well-collimated laser through the center of the entrance slit to a suitably small target placed at the center of the mirror.

C.1 CHOOSING THE CORRECT LENS MATERIAL

The first step in selecting a pair of lenses is to consider the lens material. While glass lenses may be a simple and cost-effective solution in some cases, they have two distinct disadvantages that render them nearly useless in other cases. For one thing, lenses are themselves dispersive elements: since glass has a higher index of refraction for blue light than it does for red light, rays of blue light passing through a glass lens will bend to a larger degree than rays of red light. This effectively gives the lens a focal length that depends on wavelength, with shorter wavelengths corresponding to shorter focal lengths. This becomes problematic when carrying out experiments over large spectral ranges, where proper focus may be obtained for only a portion of the wavelength region of interest. Although for glass lenses this has an observable impact even for visible wavelengths, the problem only worsens for the UV, where the change in refractive index over a given wavelength interval increases (See Figure 50, which shows the refractive index of Thorlabs' N-BK7 borosilicate crown glass). As a result, when using a white light source as a source of UV, obtaining a proper focus or collimation with the observed visible light will not guarantee the same for the UV. In this case it may be helpful to block out the visible light from the source using a shortpass filter, and observe the transmitted UV with a phosphor.

A second problem with using glass lenses has to do with their transmittance. Figure 51 shows the transmittance for a 10 mm thick plate of N-BK7 borosilicate glass, demonstrating that while glass is largely transparent for most wavelengths visible to the eye, it can be almost totally absorbing for the UV and near-infrared. This alone renders glass lenses nearly useless for many of the experiments discussed in this work, where the UV is the primary wavelength region of interest. In this case it is preferable to use high purity fused silica or quartz lenses which have high transmittance for wavelengths as short as 2000 Å, although lower purity,

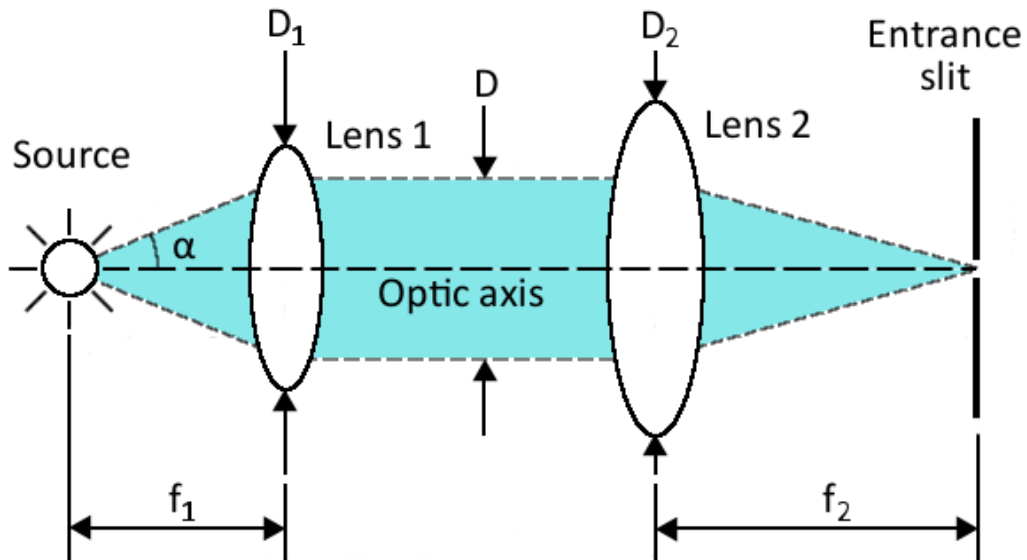


Figure 49: Basic setup using a pair of lenses to collect light from a source and focus its image on an entrance slit. With the source placed one focal length f_1 from Lens 1, the light is collimated and sent to Lens 2. The latter in turn focuses the light on the entrance slit at its focal length f_2 . The collimated beam diameter D is determined by the smaller of the two lens diameters, D_1 and D_2 . α denotes the half-angle for the light cone collected from the source.

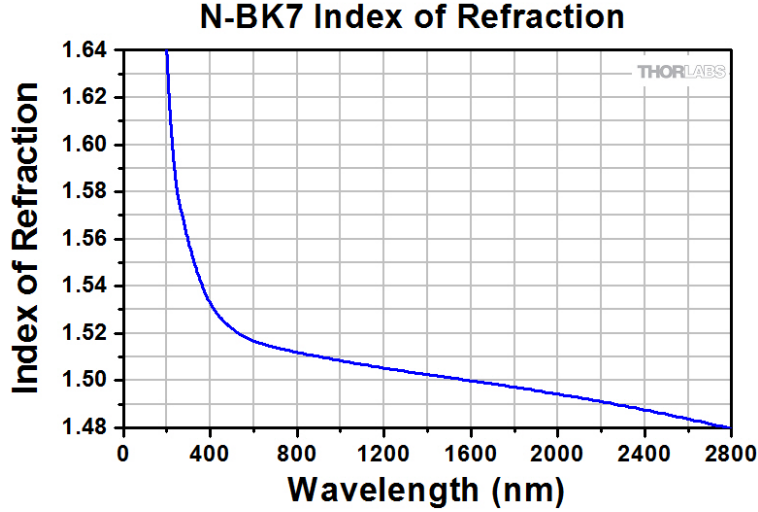


Figure 50: Refractive index of Thorlabs’ N-BK7 borosilicate crown glass [101]

commercial grade quartz may be perfectly suitable for wavelengths as short as 3000 Å. An added advantage to using quartz is that it has somewhat lower dispersion than glass (compare Figure 52, which shows the refractive index of Thorlabs’ UV Fused Silica, to Figure 50). For similar reasons, MgF₂ and CaF₂ are also well-suited for UV applications.

C.2 OPTIMIZING LENS DIMENSIONS AND POSITIONING

The next step in selecting a pair of lenses is to determine their dimensions, namely their diameters and focal lengths. We denote the focal length and diameter for the lens closest to the source f_1 and D_1 , respectively, and similarly for the second lens. We take the slit to have height h_{slit} and width w_{slit} . For simplicity the source is taken to be rectangular, with height h_{source} and width w_{source} , and has zero length along the optic axis. The optimal dimensions for the pair of lenses in terms of light throughput will depend on these quantities.

To see how, consider the radiant flux $d\Phi$ (dimension: energy per unit time) emitted from

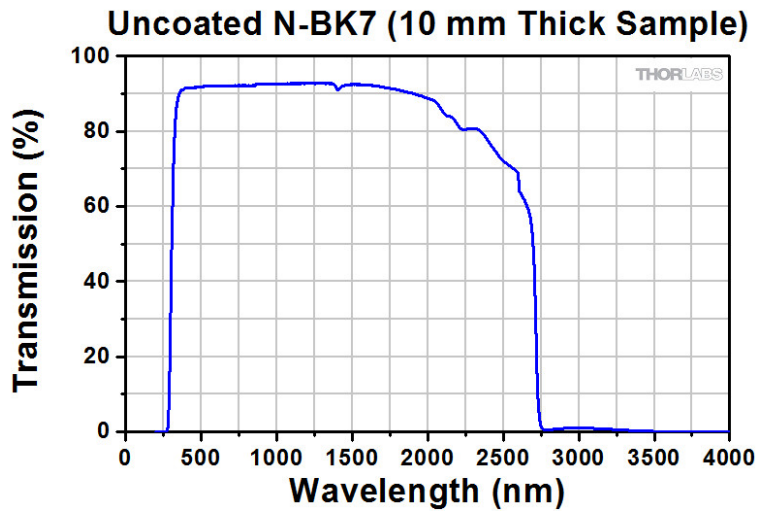


Figure 51: Transmittance of a 10 mm plate of Thorlabs' N-BK7 borosilicate crown glass [101]

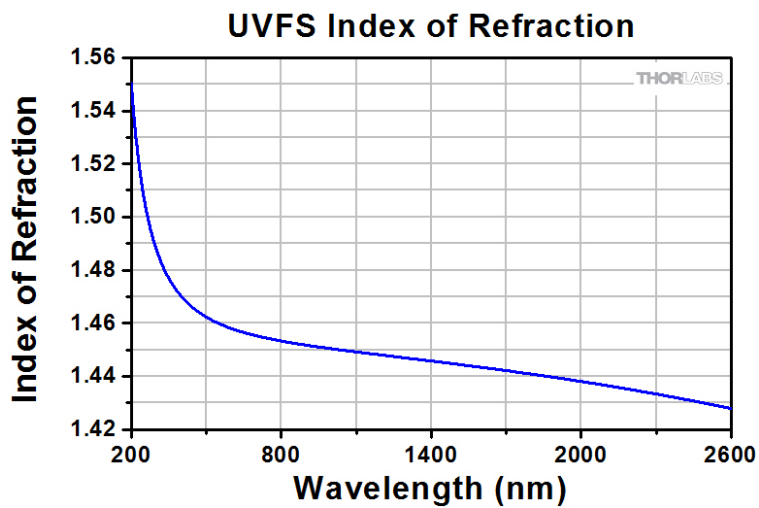


Figure 52: Refractive index of Thorlabs' UV fused silica [101]

a single infinitesimal element of a radiating surface [102]:

$$d\Phi = LdSd\omega, \quad (\text{C.1})$$

where L and dS are, respectively, the radiance (dimension: energy per unit time per unit area) and projected area of the surface element, and $d\omega$ is the solid angle into which light is emitted at a specified direction. In general, any one of these quantities could depend on the direction at which the light is emitted as well as the position on the surface where the specified infinitesimal element is located. For instance, the projected area will vary as $dS = dS_0 \cos \theta$ where dS_0 is the total area of the infinitesimal surface element, and θ is the angle the emitted light makes with the surface normal. For the entirety of the surface, the total flux is given by [102]:

$$\Phi = \int_{S_0} \int_{\Omega} L dS d\omega, \quad (\text{C.2})$$

where S_0 is the total surface area of the radiating object and Ω is the total solid angle collected from a specified point on the surface (see Figure 53).

In order to actually evaluate the integral in terms of adjustable parameters, we return to the specific example of a light source imaged on an entrance slit by two lenses. Just as in Figure 49, we assume the source is positioned at the exact focus of lens 1, the slit is positioned at the exact focus of lens 2, and each element is aligned with its center lying on the optic axis. We can then write the integral over S_0 in terms of a rectangular x-y coordinate system with the origin at the center of the source on the optic axis.

For each point on the surface, we can write the integral over the total solid angle Ω in terms of a spherical coordinate system whose colatitude angle θ is measured from the normal to the surface of the source at that point. All the light collected from a given point is defined by the solid angle Ω captured by lens 1. In general Ω will vary from point to point on the surface, and so to simplify the calculation we assume that the source is small enough compared to the dimensions of lens 1 that the integral over Ω is constant and equal to that at the center of the source.

The radiance L , which roughly corresponds with how bright the object is, clearly plays an important role in how much light can be gathered from the object, but cannot practically be manipulated once a light source and its operating conditions are chosen. Assuming that

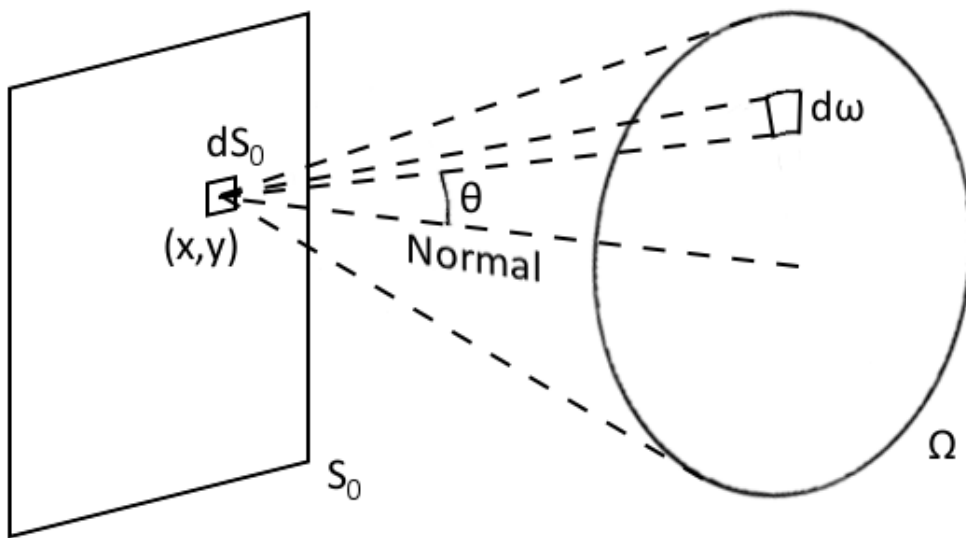


Figure 53: Diagram showing the relevant quantities for calculating the radiant flux emitted into a solid angle Ω from a planar surface S_0

it doesn't vary with the position on the surface or the direction of the emitted rays, it can be brought out of both integrals. This last assumption may be the least justified in the case of the xenon lamp used in this work. The operation manual even states that the light-generating plasma inside the lamp shows spatial variations in brightness up to about 20% of the mean brightness, with most of it concentrated at one of the two electrodes. In any case, with the radiance now being a simple multiplicative constant, it will be dropped in order to focus attention on the remaining, purely *geometric* quantities that may be chosen more freely.

With all the above simplifications, we can finally express the explicit form for the light flux captured from the source:

$$\Phi = \int_{-w_{src}/2}^{w_{src}/2} dx \int_{-h_{src}/2}^{h_{src}/2} dy \int_0^{2\pi} d\phi \int_0^\alpha d\theta \cos \theta \sin \theta. \quad (\text{C.3})$$

Here, w_{src} and h_{src} are, respectively, the width and height of the source, and α is the half angle defining the solid angle for the light collected from the center of the source, as shown in Figure 49. Note that in the integral over θ the $\sin \theta$ comes from the expression for $d\omega$ in spherical coordinates, whereas the $\cos \theta$ comes from the angular dependence of $dS = dS_0 \cos \theta$. The integrals can be easily evaluated to give:

$$\Phi = \pi w_{src} h_{src} \sin^2 \alpha = \pi A_{src} \sin^2 \alpha, \quad (\text{C.4})$$

where $A_{src} = w_{src} h_{src}$ is the total area of the source. Referring back to Figure 49, we see that we can express $\sin \alpha$ in terms of adjustable parameters:

$$\sin \alpha = \frac{D/2}{\sqrt{f_1^2 + (D/2)^2}} = \left[1 + \left(\frac{2f_1}{D} \right)^2 \right]^{-1/2}. \quad (\text{C.5})$$

The diameter D of the collimated beam is determined by the diameter of the smaller lens. Having one lens larger than the other affords no advantage in terms of light throughput (neglecting spherical aberrations from the lens), and so we take both lenses to have this same diameter. Although this is sufficient to form an image of the source on the entrance slit, one must also account for losses which may occur beyond the entrance slit.

Consider what happens when the half-angle corresponding to the light focused on the entrance slit is too large, as shown in Figure 54. We see that, although light does manage

to pass through the entrance slit and illuminate the first mirror inside the monochromator/spectrometer, the rays at the peripheries miss the mirror. Not only is this a loss of signal passing through to the detector, but it is also a significant source of scattered light, which could raise the noise level at the detector output. It is for this reason that it becomes necessary to reduce the half-angle for the light cone entering the slit to the point that the first mirror is fully illuminated, and no more. At this point we say we have matched the *f-number* of the lens system to that of the monochromator/spectrometer.

For the monochromator/spectrometer, the f-number is the ratio of the focal length of the first mirror to the mirror's diameter, and may be seen to decrease with increasing half-angle of the light cone illuminating the mirror. We may analogously define the f-number corresponding to lens 2 as the ratio of its focal length to its diameter. The mirror will be fully illuminated when these two are equal:

$$\text{f-number} = N = f_{\text{mirror}}/D_{\text{mirror}} = f_2/D. \quad (\text{C.6})$$

With that condition having been satisfied, we can rewrite the expression for $\sin \alpha$ as:

$$\sin \alpha = \left[1 + \left(\frac{2Nf_1}{f_2} \right)^2 \right]^{-1/2} = \left[1 + \left(\frac{2N}{M} \right)^2 \right]^{-1/2}, \quad (\text{C.7})$$

where $M = f_2/f_1$ is the magnification of the two-lens system. Our expression for the total flux becomes:

$$\Phi = \pi A_{\text{src}} \left[1 + \left(\frac{2N}{M} \right)^2 \right]^{-1}. \quad (\text{C.8})$$

It must be noted, however, that this is only the light flux that reaches the slit, *not* the light flux that actually passes through the slit, which is the more important quantity. We know that the linear dimensions of the source get scaled by a factor of M when the image is formed at the entrance slit, and if these lengths exceed the dimensions of the slit, some of the light forming the image will be blocked. This is known as *vignetting*, and we may account for it by multiplying expression (C.8) by a *vignetting factor* V . When the entire image of the source passes through the slit, there is no vignetting and we set $V = 1$.

What happens when this is not the case depends on the particular dimensions of the source and slit. To give an explicit example, we consider the case of the arc lamp source,

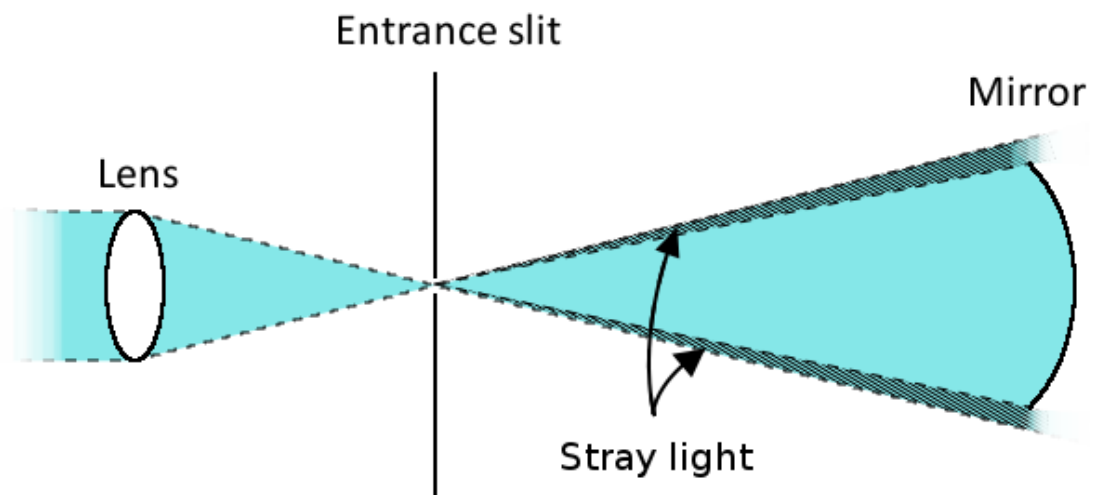


Figure 54: Diagram showing a lens with smaller f -number than that of the monochromator into which it is directing light. The solid angle of the light cone illuminating the mirror beyond the entrance slit is too large, and the light that misses the mirror contributes to scattered light inside the monochromator.

with $h_{src} = 2\text{mm}$ and $w_{src} = 0.5\text{mm}$. For the slit we take typical values: $h_{slit} = 5\text{ mm}$ and $w_{slit} = 0.1\text{ mm}$. In this case, as the image is magnified, the image is vignetted along its horizontal dimension first, since $M_1 = w_{slit}/w_{src} = 0.2 < M_2 = h_{slit}/h_{src} = 2.5$. For $M_1 < M < M_2$, V should be the fraction of the image's width that makes it through the slit, which is simply w_{slit}/Mw_{src} . For $M > M_2$, when the image is vignetted along both horizontal and vertical dimensions, V should include an additional factor h_{slit}/Mh_{src} . Putting this all together, we have for the final expression of light flux passing *through* the entrance slit:

$$\Phi = \begin{cases} \pi w_{src} h_{src} \left[1 + \left(\frac{2N}{M}\right)^2\right]^{-1} & M < M_1 \\ \pi (w_{slit} h_{src} / M) \left[1 + \left(\frac{2N}{M}\right)^2\right]^{-1} & M_1 < M < M_2 \\ \pi (w_{slit} h_{slit} / M^2) \left[1 + \left(\frac{2N}{M}\right)^2\right]^{-1} & M > M_2 \end{cases} \quad (\text{C.9})$$

We plot this relationship in Figure 55 with the above source and slit dimensions for typical f-numbers $N = 5, 7, 10$. It can be seen that for all cases a maximum in radiant flux is reached for $M = M_2 = 2.5$, i.e., as soon as the image of the source fills the slit along both its horizontal and vertical dimensions. Any further magnification will tend to reduce the flux getting through the entrance slit, although this problem is apparently less severe for higher f-number. One caveat with this result is that while radiant flux may be optimized when the entire height of the entrance slit is filled, the optical aberrations induced in the image at the detector by the monochromator/spectrometer may increase with this height as well, and so it is up to the experimenter to determine the maximum usable height of the slit to minimize these aberrations to an acceptable level.

It is seen that Φ depends only on the *ratio* of the focal lengths of the two lenses, namely the magnification M , and not at all on their diameter D . Of course, one cannot choose arbitrarily large lenses, because the sum of the two focal lengths must be smaller than the separation between the source and the slit. In practice, the selection of the pair of lenses should proceed as follows: calculate the optimal magnification according to the source and slit dimensions and decide upon an f_1 and f_2 that can be accommodated by the spatial constraints of the system. Then one must choose their diameter such that the light cone entering the slit matches the f-number of the monochromator/spectrometer. If a pair of lenses cannot be found with the required diameter, one can use lenses of larger diameter

and simply reduce the collimated beam diameter with an iris placed between them until the f-numbers are matched.

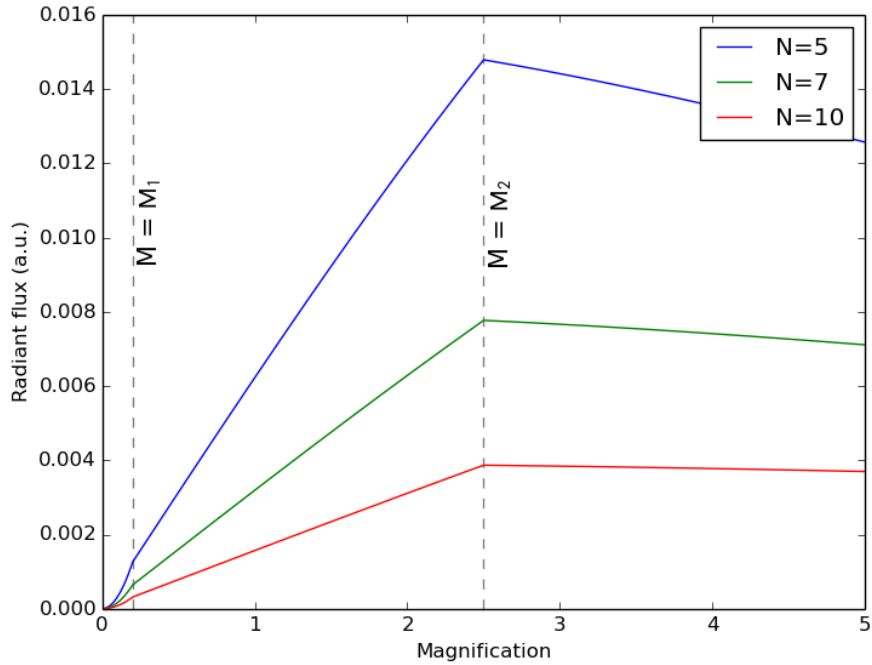


Figure 55: Plots of radiant flux Φ as a function of source magnification M . The source is assumed to have dimensions 2 mm by 0.5 mm and the slit is assumed to have dimensions 5 mm by 0.1 mm. Each curve corresponds to a unique f-number N for the lens focusing the light on the entrance slit, which is assumed to match that of the monochromator/spectrometer.

APPENDIX D

MONOCHROMATOR ALIGNMENT AND CALIBRATION

In the Appendix C it was discussed how to position a light source and a pair of ancillary lenses along some pre-determined optic axis for optimal throughput into the entrance slit of a monochromator. For practical purposes, this optic axis ought to be determined by the optical elements inside of the monochromator, since these are the most difficult to align. The purpose of this Appendix is to give specific step-by-step instructions for the basic alignment of a few of these optical components for the case of the SPEX 1401 double monochromator used in this work for absorption measurements. The intent is not to provide a complete re-alignment procedure, which is already given in the SPEX 1401 manual. It is presumed that all of the mirrors are in their factory-set positions, and they are to remain that way throughout the following instructions. The only components that will be adjusted are the pair of diffraction gratings, the pair of concave mirrors closest to the exit slit, and the three slits (entrance, intermediate, and exit). Adjustments to any of the other mirrors are discouraged if one has not at least consulted the manual or a trained support technician. The instructions given here should hold equally well for using the monochromator with and without use of wavelength modulation; however, certain details have special import when wavelength modulation is being used. These will be highlighted when relevant.

Once the monochromator has been re-aligned, it needs to be recalibrated. The standard practice is to illuminate the entrance slit with light from various gas discharge lamps and monitor the light reaching the exit slit of the monochromator with a detector as the gratings are rotated. The emission spectrum from these lamps consists of a series of sharp

peaks. This allows one to determine the wavelength to which the monochromator has been set for only a discrete set of grating orientations, which are measured through a dial indicator on the outside of the monochromator. To determine the wavelength being selected by the monochromator at any dial reading, one needs a scheme for interpolating between these points. The most accurate interpolation must take into account the specific gearing mechanism which couples the dial to the rotating grating shaft. The SPEX 1400 series is somewhat atypical in this respect, and so it is worth some discussion.

An overview of the internal optical elements of the SPEX 1401 double monochromator is shown in Figure 56. The dotted line passing through the entrance slit S1 is the optic axis, and its extension through the rest of the instrument indicates the path a beam of light should take after subsequent reflections and diffraction if all of the optical elements have been properly aligned and the light is of the correct wavelength to fulfill the grating equation:

$$m\lambda = 2d \sin \theta \cos \phi. \quad (\text{D.1})$$

In the above, m is the diffraction order (for all measurements in this work, $m = 1$), λ is the wavelength, d is the grating's groove spacing, θ is the grating's angle of rotation from its zero order position (in which the grating normal faces directly between the two opposite-facing concave mirrors), and $\phi = 6.9^\circ$ is fixed by the monochromator geometry. Along the path S1-M1, the beam is diverging, and upon reflecting off of mirror M1 it is collimated in the direction of G1. The beam diffracted by G1 towards M2 is then focused and redirected by M2 along the path M2-M3-S2, with the intermediate slit S2 coinciding with the final, focused slit image.

Depending on the width of this intermediate slit, a large proportion of stray light and unwanted spectral components from the original beam are mostly blocked, and the remaining light passes through a similar trajectory in the second half of the double monochromator. If the slit widths of S1 and S3 are identical, the dispersion (angular spread $\delta\theta/\delta\lambda$ between constituent wavelengths) and overall wavelength resolution is doubled with respect to that of a single grating.

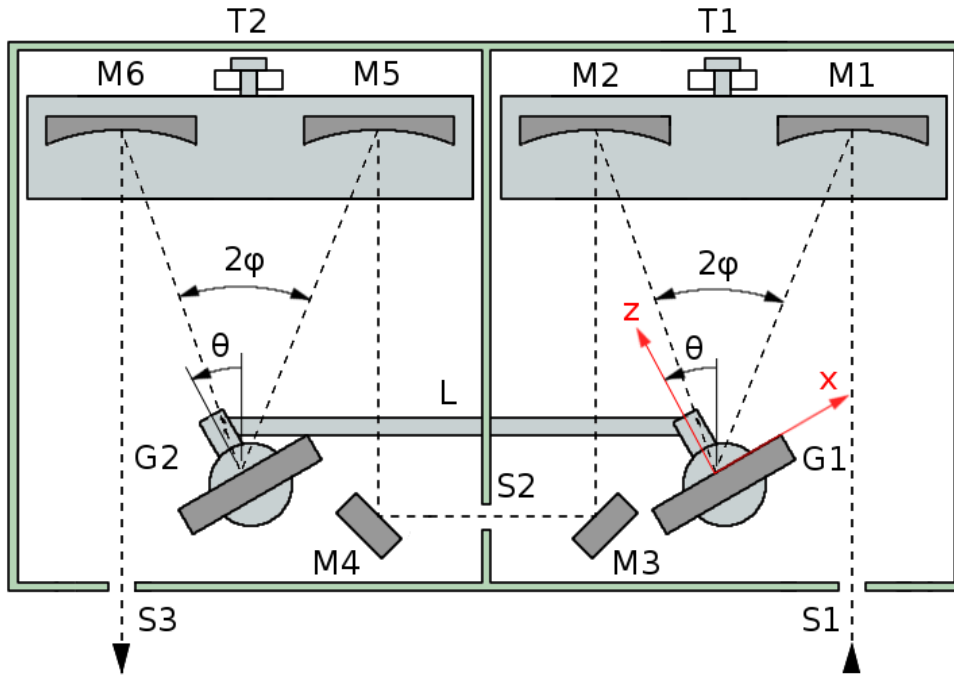


Figure 56: Top down view of SPEX 1401 double monochromator. Components include slits S1, S2, and S3, mirrors M1 through M6, and gratings G1 and G2 mechanically linked by a bar L. Concave mirrors M1, M2, M5, and M6 may be translated towards or away from the gratings in pairs through adjustment screws T1 and T2. A monochromatic beam from the exit slit S3 propagates along the dotted line. The coordinate system refers to that shown in Figure 59.

D.1 CONSIDERATIONS FOR WAVELENGTH RANGE OF INTEREST

The beam should be centered on all components, and as mentioned in Appendix C, proper f-number matching results in the four concave mirrors being fully illuminated. It should be noted that as the gratings rotate towards larger θ , the effective f-number of the monochromator increases (since the projected areas of the gratings normal to the beam decrease), in which case it may be necessary to adjust the external optics to illuminate a smaller region at the center of the concave mirrors and match the reduced f-number. Since from (D.1) different θ correspond to different wavelengths, it is advisable to confine one's measurements to small wavelength ranges to avoid having to make such adjustments, if possible.

Similarly, the focal planes inside the monochromator are not identical for all wavelengths of light. For instance, if a beam of red light is focused properly at each of the slits, a beam of blue light comes to a focus some distance before each of these slits along the path of propagation. This is not due to the monochromator itself, since it is made up entirely of reflective optics, but to the external lens system. Proper focus can be attained for small wavelength intervals ($\sim 1000\text{-}2000 \text{ \AA}$) by adjusting screws T1 and T2 (see Figure 57), which translate the pairs of concave mirrors in either half of the monochromator toward or away from the gratings, and this in turn translates the focal planes toward or away from slits S2 and S3 (presumably one has already established proper focus for the desired wavelength range at S1 as discussed in Appendix C). One should note that the plate on which the two pairs of mirrors are mounted slides along a track fixed to the monochromator base board, which ensures that adjustments to T1 and T2 translate the mirrors with little to no rotation.

In practice one sets the width of the intermediate slit S2 much larger than that for S1 and S3 since its purpose is primarily to eliminate stray light, so a proper focus at this slit is not so critical. To verify that the beam is properly focused at the exit slit S3, one can pass light from a source of very narrow ($\Delta\lambda \ll 1 \text{ \AA}$) spectral lines (commercially available "pen lamps" containing various noble gases are convenient sources), and record the output from a detector placed outside S3 while scanning the grating through one of these lines at various positions of the concave mirrors. Of course, to observe this effect the slits S1 and S3 must be narrower than the broadening due to improper focus.

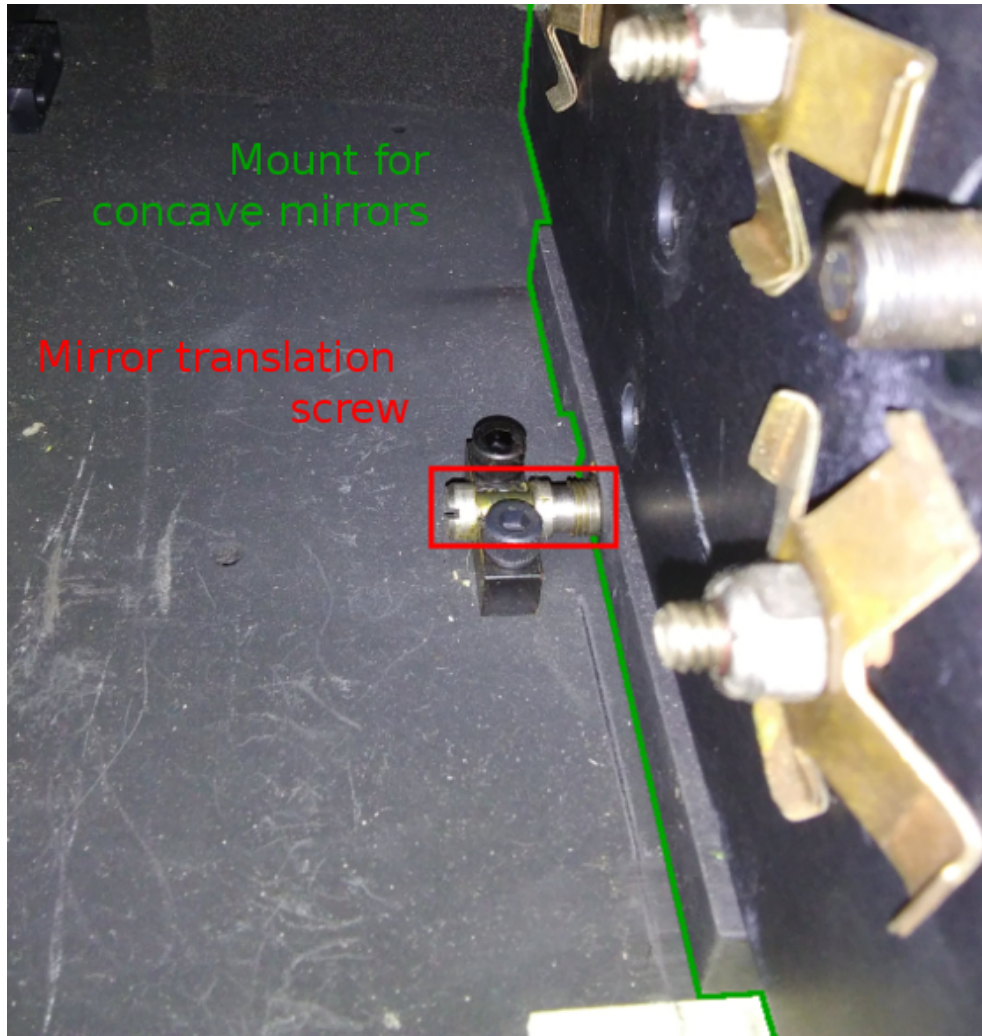


Figure 57: Adjustment screw for translating the pair of concave mirrors in either half of the SPEX 1401. This is done to shift the focal plane to coincide with the exit slit.

D.2 GRATING INSTALLATION AND ALIGNMENT

When one has settled upon a given wavelength interval and tuned the monochromator to that interval as in the previous steps, it may yet be necessary to modify the alignment based on other criteria. For this work, the two most important criteria were light throughput and spectral resolution. The slit widths of S1 and S3 are the most easily adjusted experimental parameters for increasing one at the expense of the other, and this alone would not require any re-alignment, assuming the monochromator was aligned to begin with. However, in cases where exceedingly high resolution is required, the necessary slit widths may be impractically small. In this instance it may be preferable to install diffraction gratings with higher groove density (smaller d in (D.1)) so that the increased angular dispersion $\delta\theta/\delta\lambda$ allows for a larger slit width for a given wavelength resolution. The instructions that follow give the procedures for installing and aligning both gratings in the SPEX 1401.

Both diffraction gratings are held in place in mounting plates such as that shown in Figure 59, reproduced from the SPEX 1401 manual. For easy installation of the gratings, one may release the mounting plates from their backing plates by lifting up the lever shown in Figure 58. It may be necessary to loosen screw A to provide clearance. Extreme care needs to be taken when installing the diffraction gratings in the mounting plates. Even light contact with the reflective surface can introduce imperfections in the grooves and the reflective coating.

One should also pay close attention to the orientation of the grating as it is being installed. For one thing, the grooves should be oriented along the y direction in Figure 59 (which is normal to the plane of dispersion), but if the grating has been blazed as in Figure 60, most of the diffracted light will be directed into either the positive or negative orders (m from equation (D.1)). The gratings ought to come with some sort of indication of the blaze direction (it is typically an arrow pointing toward the higher intensity orders). One should ensure that, first: both gratings are oriented with their blaze directions pointed the same way, and second: the gratings are rotated to angles θ such that mirrors M2 and M6 will receive the higher intensity orders. From (D.1) one can change between positive and negative orders by changing the grating rotation angle from θ to $-\theta$. However, if for some reason the

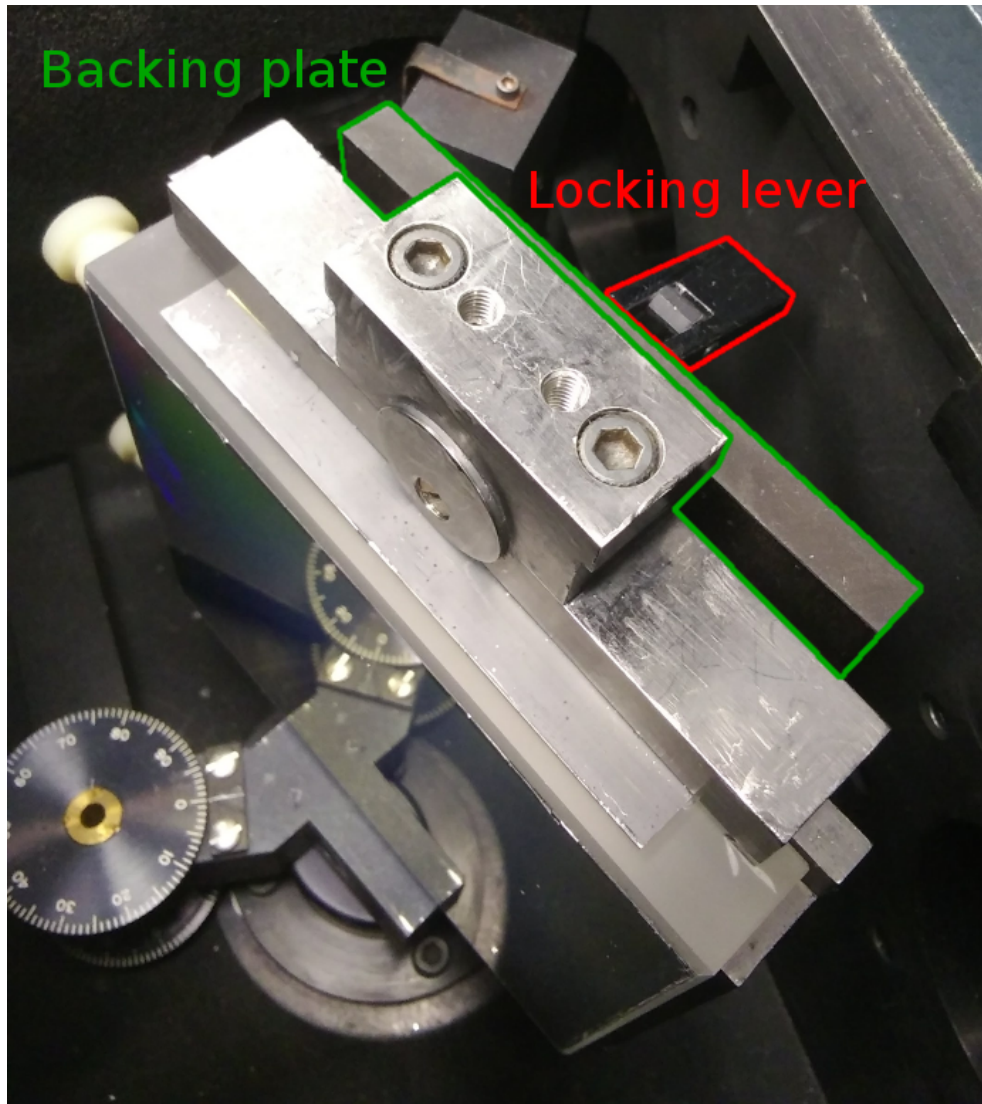


Figure 58: The grating and its mounting plate are locked up against the backing plate by a locking lever. Pulling up on the lever allows the grating and its mounting plate to be removed for replacement.

user must constrain the gratings to, say, positive θ , one should ensure when installing them that the positive orders will fall on mirrors M2 and M6 for those angles. For example, in this work the optical scanner used to modulate the wavelength was mounted just inside the entrance slit S1, and so it was desirable to have the grating G1 facing away from the scanner at S1. This is the configuration shown in Figure 56, and in this view the blaze direction for both gratings ought to point in the positive x direction. For symmetric groove profiles such as the sinusoidal profile commonly offered with holographic gratings, these considerations are unnecessary.

With the proper orientation for the gratings having been established, place the gratings in the channel-shaped recess of the mounting plates (these can accommodate gratings up to 110 mm in height). The gratings can then be fixed in place with nylon screws threaded into the holes marked F and G in Figure 59. To provide additional grip, one may also apply silicone rubber cement through the back of the plate at the holes H, I, and J. With the gratings securely in place, return the mounting plates to the backing plates from which they were removed, making sure the hook on the backing plate is engaged with the fixture on the back of the mounting plate. Push the lever down to secure the mounting plate to its backing plate. The gratings are now ready for alignment.

Aligning the gratings is achieved by turning screws A through E in Figure 59. Screws A, B, and C pass through to the back of the mounting plate and are pulled up against the backing plate by the hook to form a three point mounting arrangement. Adjust these three screws until the mounting plate is roughly parallel with the backing plate. Tilting the grating about the x axis is now accomplished simply with adjustment to the single screw A. A tilt about the y axis can be accomplished with an adjustment to B (unscrewing a quarter turn, say) and an equal and opposite adjustment to screw C (screwing in a quarter turn). Both screws D and E tilt the grating about the z axis, with one acting as a stop to the other (these are the small, recessed screws nearest to each other seen atop the mounting plate in Figure 58, not the larger cap screws on the outside). To adjust this tilt, first unscrew one and then screw in the other the desired amount. Finally, screw the first one back in until tight.

The gratings will now be tilted about the x axis to center the light's propagation path

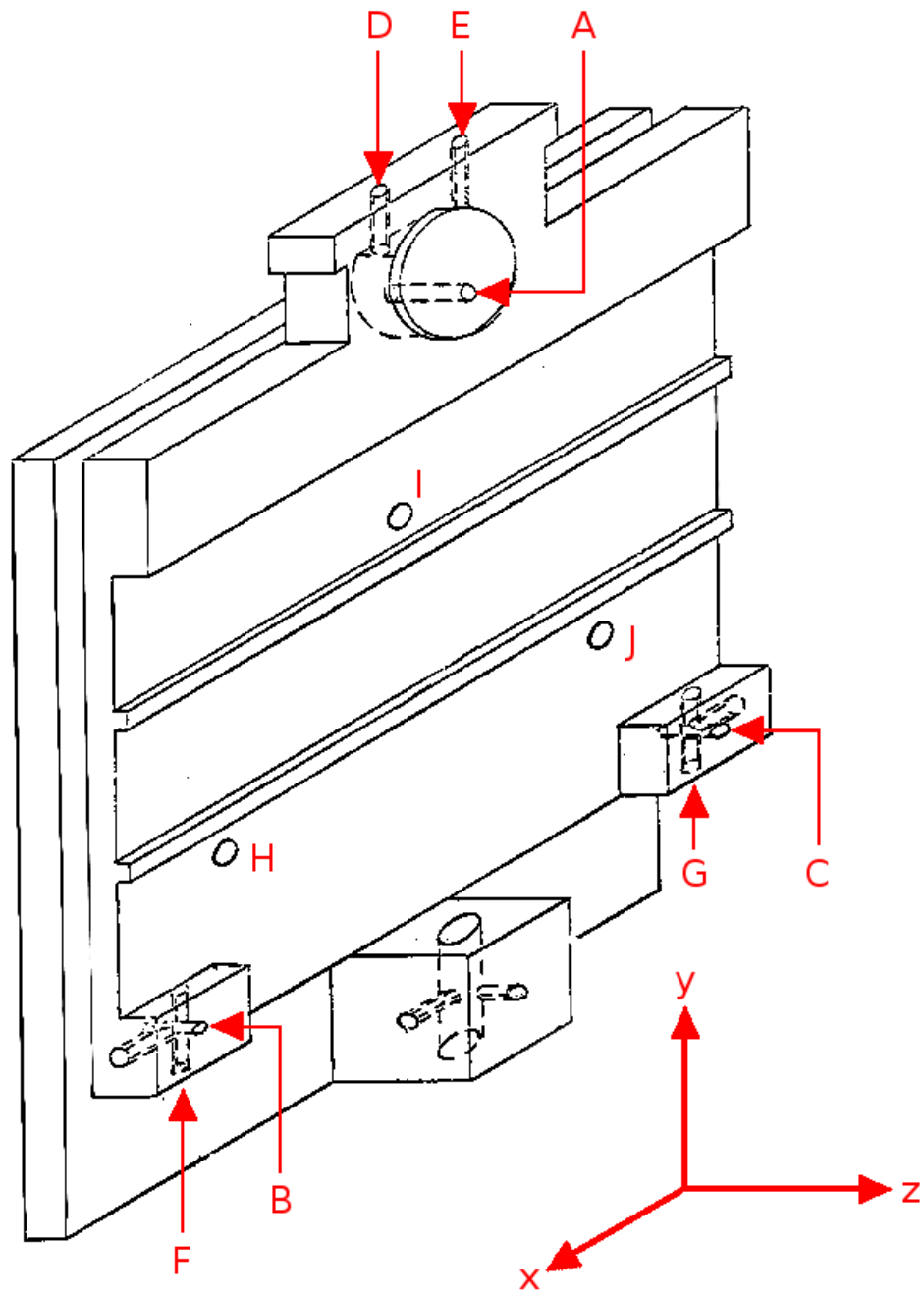


Figure 59: Grating mounting plate marked with locking and adjustment screw positions

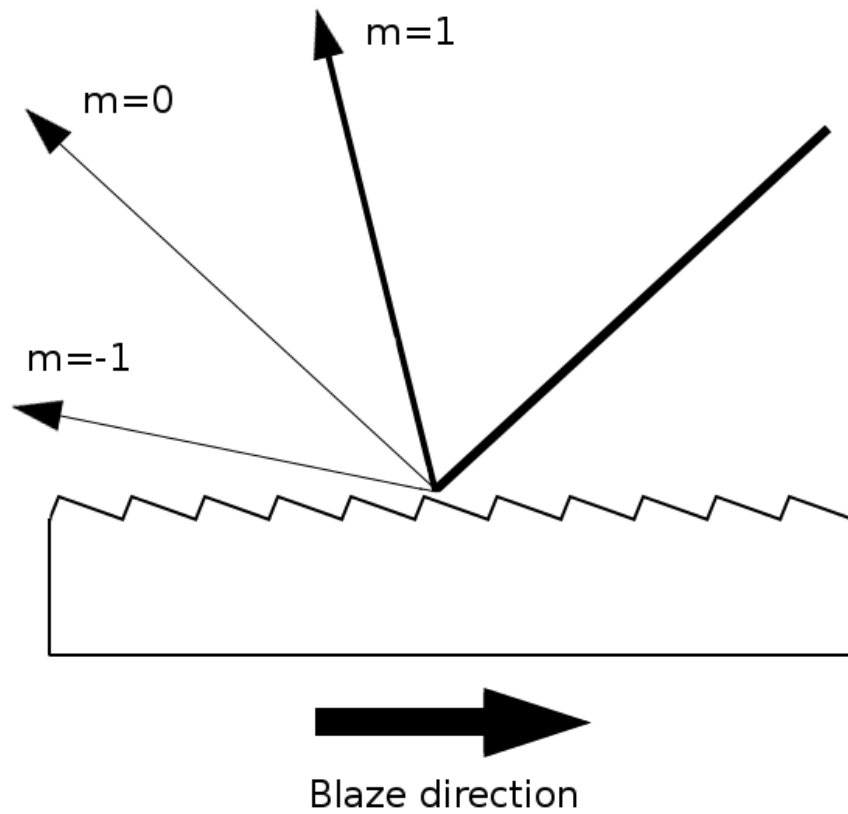


Figure 60: Illustration of a blazed groove profile of a diffraction grating (the grooves are oriented normal to the figure). The facets that make up the grooves are inclined towards the blaze direction, which directs most of the radiant energy into one particular diffraction order. In the case shown the $m = 1$ diffraction order is stronger than the $m = -1$ diffraction order.

vertically on all optical components. Assuming the external optics have been aligned with the monochromator's optic axis, illuminate the entrance slit with a white light source. It will be necessary to rotate the gratings to $\theta = 0^\circ$ such that the zero order reflection (in which all colors overlap) follows the dotted line path in Figure 56. It is recommended that the gratings be rotated manually, as this step and others that follow could take exceedingly long when rotating the gratings with the stepper motor. To do so, remove the side panels of the monochromator where the wavenumber dial appears, and loosen the two set screws highlighted in Figure 61 that secure the lever bar to the shaft that rotates the grating G1. The gratings can now be freely rotated in unison by moving the bar L (see Figure 56) that links them together (do not try to rotate the gratings, mounting plates, or backing plates directly as this could introduce misalignment).

With both gratings rotated to $\theta = 0^\circ$, a white light image of the entrance slit S1 should appear at or near to both S2 and S3. Adjust screw A on both mounting plates until these images are centered vertically on S2 and S3. Now rotate the gratings while observing the intermediate slit. At a certain point a band of color should appear across the slit (open the entrance slit and place a notecard or phosphor in front of the slit if you suspect the light is too dim). This is the first order diffracted light. Continue to rotate the gratings in the same direction as far as possible without letting it become too dim to see conveniently. Now compare the height of the band of color with that of the image that appeared there at zero order (rotate the gratings back and forth between this position and $\theta = 0^\circ$ if necessary). If the band of color is either high or low in comparison, adjust the tilt about z for grating G1 until the band is centered vertically on S2. Rotate the gratings slowly back to $\theta = 0^\circ$ and verify that the band of color does not shift vertically with the rotation. If not, then G1 is now properly aligned and one can now adjust the z tilt for grating G2 in the same manner but while observing the slit image on the exit slit S3. In this case the band of color may be quite a bit narrower, since now the range in observed wavelengths has been limited by the intermediate slit S2. This may make it harder to see, and if so one may open one or both of the slits S1 and S2 to allow in more light.

The image may also appear off to one side of the slit S3. If that is the case the gratings are slightly offset from one another, i.e. one is tilted about its y axis relative to the other.

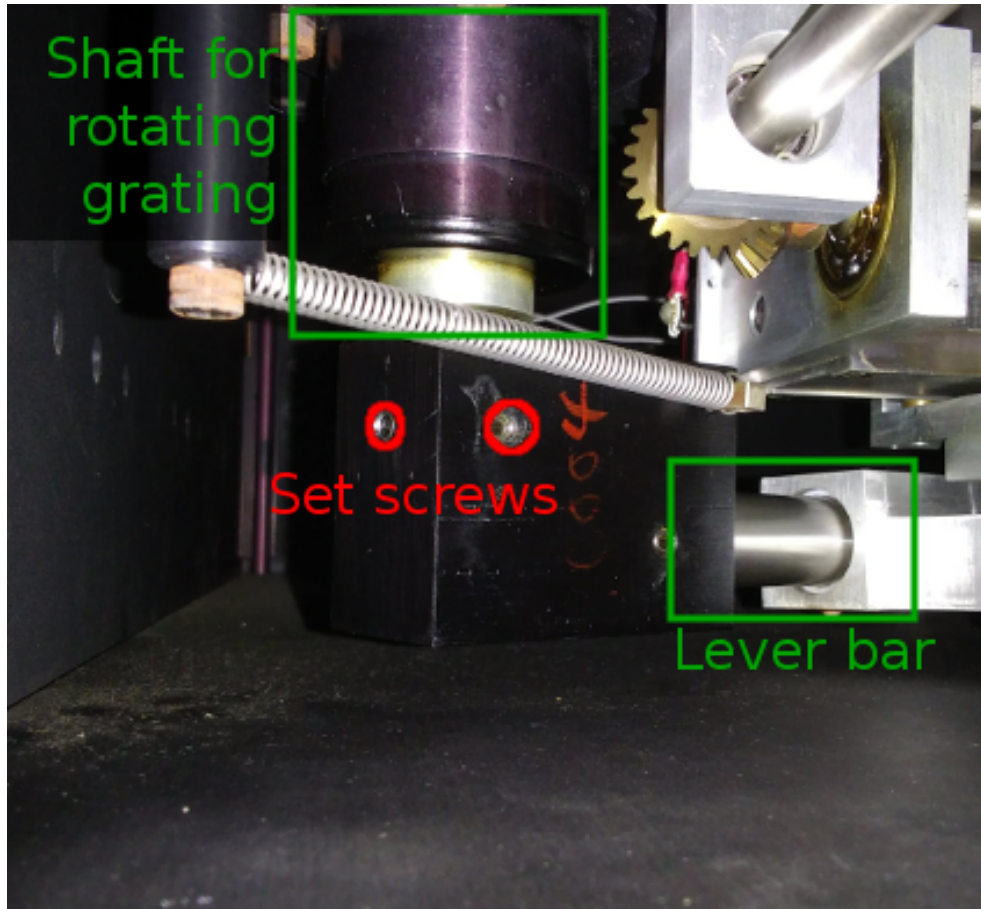


Figure 61: View of the mechanical drive system underneath the SPEX 1401. In order to rotate the gratings manually during alignment, the lever bar may be detached from the shaft on which the grating rotates by loosening the set screws circled in red.

The adjustment to the tilt about the z axis can be accomplished even if this is so, and once that is done one can adjust the tilt about the y axis for grating G2 in the following steps. First, consider the wavelength range in which the monochromator is to be used, and rotate the gratings such that light from the central portion of that range will appear at the exit slit (use (D.1) to estimate the required grating angle and a notecard or phosphor to observe the beam if it is in the ultraviolet). Be aware that any slight misalignments in the steps following or preceding may make it necessary to repeat the following procedure when operating the monochromator outside that range. Re-tighten the set screws holding the lever bar to the rotating shaft under the grating G1, and re-attach the side panels that were removed. Now make a course adjustment to the tilt about y to get the image to approximately overlap with S3. As described earlier, make slight adjustments to one of the two screws B or C and follow with an equal and opposite adjustment to the other.

In order to make further, fine adjustments as precisely as possible, it will now be necessary to reduce the width of the image appearing on S3. This can be done by reducing the widths of both slits S1 and S2 to about 100 μm or less. Do the same for the exit slit S3. Place a detector with sufficient sensitivity in the chosen wavelength range outside the exit slit and connect an appropriate measuring device to monitor its output in real time. Make fine adjustments to one of the two screws B or C for grating G2 until the detector output is at a maximum. If the course adjustment made earlier was performed adequately, a net 1/8 to 1/4 of a turn should be all that is necessary to complete the fine adjustments. If not, then make another course adjustment as done previously, alternating between screws B and C, and then return to making fine adjustments. Once this step has been completed, visually verify that the image is centered both vertically and horizontally on S3, widening the slits S1 and S2 if necessary. If so, both gratings are fully aligned within the monochromator, and the system is ready for use.

At this point it is worth mentioning that after alignment has been completed and one is setting the slits S1 through S3 according to the requirements of the intended measurement, some special consideration should be granted to the width of the intermediate slit S2, particularly when wavelength modulation is to be used. As mentioned, the width of S2 is often set much wider than that of S1 and S3, and so the overall wavelength resolution is determined

by the latter two. As long as S2 is at least as wide as S1 and S3 (plus some amount extra to account for misalignment), it has no effect on the overall throughput or wavelength resolution. However, when the wavelength is being modulated as in this work, with the beam being deflected back and forth across the slits S2 and S3, one must also account for the distance the beam is deflected. As noted earlier during the alignment procedure, the image appearing at the exit slit S3 has a width that is determined by the width of the intermediate slit S2. As the wavelength is modulated, this image deflects back and forth, and if the intermediate slit is set too small, the image may not totally overlap with S3 during certain parts of the deflection, as shown in Figure 62. This will appear as a momentary drop in light intensity occurring with the same or double the frequency as the wavelength modulation frequency, and could therefore be mixed in with the signal measured using lock-in detection. If an oscillating quartz plate is used to deflect the beam as in this work, this will be the case whether the plate is placed inside the entrance slit or inside the exit slit. A suitable correction for this problem is to simply widen the intermediate slit a sufficient amount, however one should also be wary of introducing too much stray light when doing so.

D.3 CALIBRATION

With the monochromator properly aligned, it may now be calibrated. The wavelength to which the monochromator is set at any given instant is determined by the rotation angle θ of the two gratings. This rotation angle is not readily accessible to the user, but a dial indicator on the side of the monochromator housing is linked through the underlying gear mechanism to the shafts which rotate the gratings. As a result, there is a specific functional relationship between the wavelength selected by the monochromator and the dial indicator that may be used for the purpose of calibration. That relationship and its dependence on the particular gearing mechanism will be discussed in what follows. A basic procedure for using this relationship to calibrate the monochromator will also be discussed.

A partial view of the mechanical drive system anchored to the underside of the SPEX 1401 can be seen in Figure 61. A schematic, top-down overview of the drive system is shown

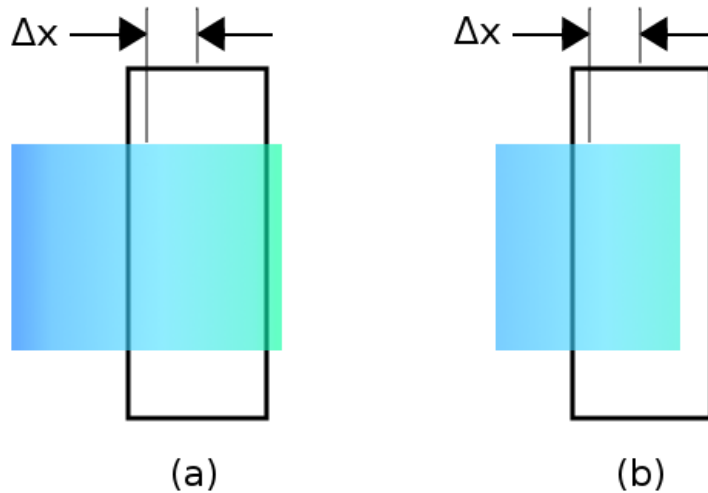


Figure 62: Illustration of the image formed at the exit slit as it is deflected an amount Δx to one side of the slit during wavelength modulation (it will be deflected to the other side by the same amount as the vibrating quartz plate at the entrance slit vibrates). In (a) the image width, which is determined by the intermediate slit width, is large enough that it totally overlaps the exit slit even during deflection. In (b) the exit slit is only partially illuminated during deflection so that the intermediate slit is too narrow. The latter case will produce an unwanted modulation in the intensity of the exiting beam.

in Figure 63. It consists of several components arranged along the sides of a right triangle PQR. The grating is situated at point P, with its rotation axis pointing out of the figure at the same point. Attached to the shaft and pointing towards the point Q is a bar that acts as a lever for rotating the grating. At Q it passes through a sleeve at the end of a second bar of fixed length A . The other end of this second bar is anchored at point R to a carriage that is threaded onto a leadscrew. The carriage is translated along the leadscrew as it rotates, moving the pivot point R along with it. This in turn causes both bars to rotate about the pivot points P and R, and with the sleeve allowed to slide along the lever bar, the right angle $\angle PQR$ is maintained.

Assuming the lever bar attached to the grating shaft points along the normal to the grating (this assumption will be relaxed shortly), the angle $\theta = \angle QPR$ in Figure 63 is the same as the one appearing in Figure 56 and (D.1). Consequently, using the grating equation (D.1):

$$x = PR = A \csc \theta = \frac{2Ad \cos \phi}{m\lambda} = k\nu, \quad (\text{D.2})$$

where $k = 2Ad \cos \phi / m$ and $\nu = 1/\lambda$ is the wavenumber. This particular implementation for a drive system is called a “cosecant drive” for the dependence of the distance x on θ [103, 104], and it is seen that this in turn results in a convenient linear dependence of x on wavenumber. For a uniformly threaded leadscrew, this distance should in turn be linear in the rotation of the primary drive shaft powered by the stepper motor. Furthermore, it should also be linear in the dial indicator, which is coupled to the drive shaft through a series of gears. In fact, the dial bears the units of cm^{-1} , the usual units for expressing wavenumber. This differs from the more common sine drive, which is linear in $\sin \theta$ as well as wavelength [103, 104]. The choice of cosecant drive reflects original intended use of the SPEX 1400 series for Raman spectroscopy, where spectra are conventionally plotted versus wavenumber.

The dial indicator reading is then given by $S = bx + a$, where b is a mechanical gear ratio, and a is some small offset due to imperfections in the drive system [104]. In order for the dial to give a true wavenumber reading $S = \nu$, a must be made as close to zero as possible, and b must be chosen equal to $1/k$. However, since k includes the order m and the groove spacing d , the dial will be incorrect when using a diffraction order m' or gratings with groove spacing d' different than those used during the factory calibration. Furthermore, in

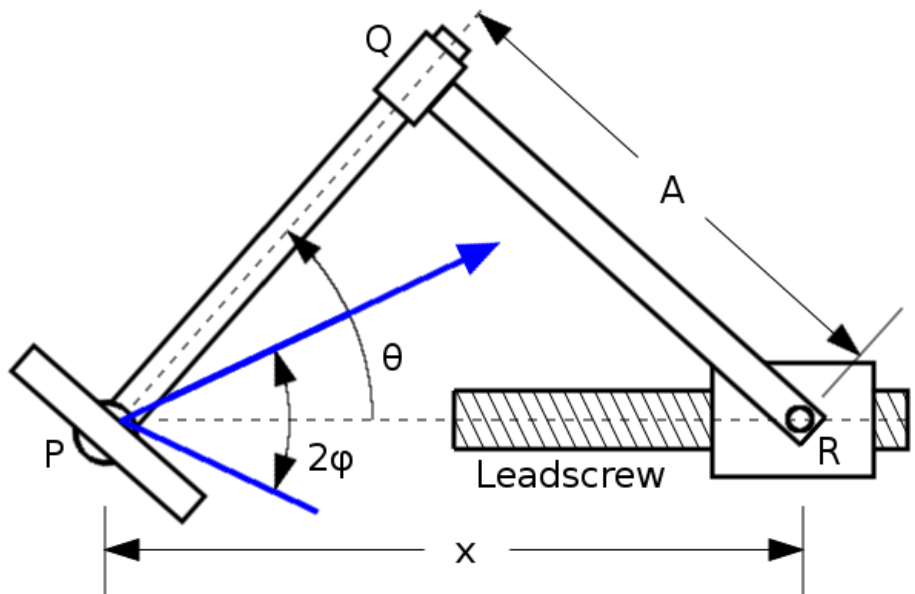


Figure 63: Top down view of the mechanical drive system for rotating the grating in the SPEX 1401. The grating is located at point P, and is rotated on a shaft by a linkage of two bars to a leadscrew at point R.

the process of installing and re-aligning the gratings presented in the previous section, it is likely that some small angular offset γ may have been introduced between the normal of the grating and the lever attached to the grating shaft (recall that it was assumed they were parallel). Taking all of these possibilities into account, we can re-express (D.1) in terms of the new parameters [104]:

$$\begin{aligned}
\lambda &= (k'/A) \sin \theta' = (k'/A) \sin(\theta - \gamma) \\
&= (k'/A)(\sin \theta \cos \gamma - \cos \theta \sin \gamma) \\
&= \frac{k'}{A} \left(\cos \gamma \frac{A}{x} - \sin \gamma \frac{\sqrt{x^2 - A^2}}{x} \right) \\
&= \frac{k'/k}{S - a} \left(\cos \gamma - \sin \gamma \sqrt{(k(S - a)/A)^2 - 1} \right),
\end{aligned} \tag{D.3}$$

where we have assumed $b = 1/k$ as required for a proper factory-set calibration. One can see that when setting $\gamma = a = 0$ and $k' = k$ (same groove spacing and diffraction order as from factory calibration), $S = 1/\lambda = \nu$ as intended.

While in principle the user knows how to compute k' for a newly re-configured monochromator, γ remains unknown, and so the new calibration (D.3) must be determined empirically. This can be accomplished by passing light through the monochromator from a source with a known spectral profile, preferably one with several narrow peaks. Commercial gas discharge lamps containing, for example, Hg, Ar, Ne, Kr, or Xe are readily available for this purpose. The exact intensities at each of the peaks in their emission spectrum vary from lamp to lamp for a given element; however, the central wavelengths at those peaks do not and have been tabulated in various sources [105, 106] for most of the strongest peaks from the ultraviolet to the infrared. As before, the light from one of these lamps may be focused with ancillary lenses onto the monochromator entrance slit along the optic axis.

As one rotates the gratings, the peaks in the lamp's emission spectrum will scan across the exit slit, and by monitoring the output of a detector placed outside this slit, one can record the dial readings at which these peaks occur. By comparing the relative spacings between peaks in the known emission profile for the lamp and the spacings between recorded dial readings, one can begin to match up specific wavelengths with each dial reading. A rough estimate for the wavelength at each of these peaks can be independently made by

measuring the rotation angle θ of the grating in each case and using (D.1) to calculate the expected wavelength. Once one has built up a table giving wavelength versus dial reading, one may then apply a fit of the form (D.3) to determine the unknown constants. With those determined, one may then use (D.3) to determine the wavelength from any dial setting within the interval for which one has recorded calibration points (be wary of extrapolating outside of this interval). An example of such a fit is shown in Figure 64.

While (D.3) is accurate, it cannot be inverted to express the dial setting needed to set the monochromator to a certain wavelength, which is often useful [104]. However, one may still compute a lookup table from (D.3) at arbitrarily small increments in the dial reading S . Another strategy is to expand (D.3) in terms of $1/S$:

$$\begin{aligned}
\lambda &= \frac{k'}{x} \left(\cos \gamma - \sin \gamma \sqrt{(x/A)^2 - 1} \right) \\
&= -\frac{k'}{A} \sin \gamma + k' \cos \gamma \frac{1}{x} - \frac{k'A \sin \gamma}{2} \left(\frac{1}{x} \right)^2 + \dots \\
&= -\frac{k'}{A} \sin \gamma + k' \cos \gamma \frac{1/k}{S-a} - \frac{k'A \sin \gamma}{2} \left(\frac{1/k}{S-a} \right)^2 + \dots \\
&= -\frac{k'}{A} \sin \gamma + k' \cos \gamma \left\{ \frac{1/k}{S} [1 + a/S + (a/S)^2 + \dots] \right\} \\
&\quad - \frac{k'A \sin \gamma}{2} \left\{ \frac{1/k}{S} [1 + a/S + (a/S)^2 + \dots] \right\}^2 + \dots \\
&\approx c_0 + c_1 \left(\frac{1}{S} \right) + c_2 \left(\frac{1}{S} \right)^2, \\
c_0 &= -\frac{k'}{A} \sin \gamma, \\
c_1 &= \frac{k'}{k} \cos \gamma, \\
c_2 &= \frac{ak'}{k} \cos \gamma - \frac{Ak'}{2k^2} \sin \gamma.
\end{aligned} \tag{D.4}$$

For small γ and a the second term should dominate while the others act as corrections. Higher order terms may be included for better accuracy at smaller dial readings (longer wavelengths), although this was found to be unnecessary for this work. The truncated form in (D.4) is easily inverted to give:

$$S = 2c_2 \left[-c_1 + \sqrt{c_1^2 - 4c_2(c_0 - \lambda)} \right]^{-1}. \tag{D.5}$$

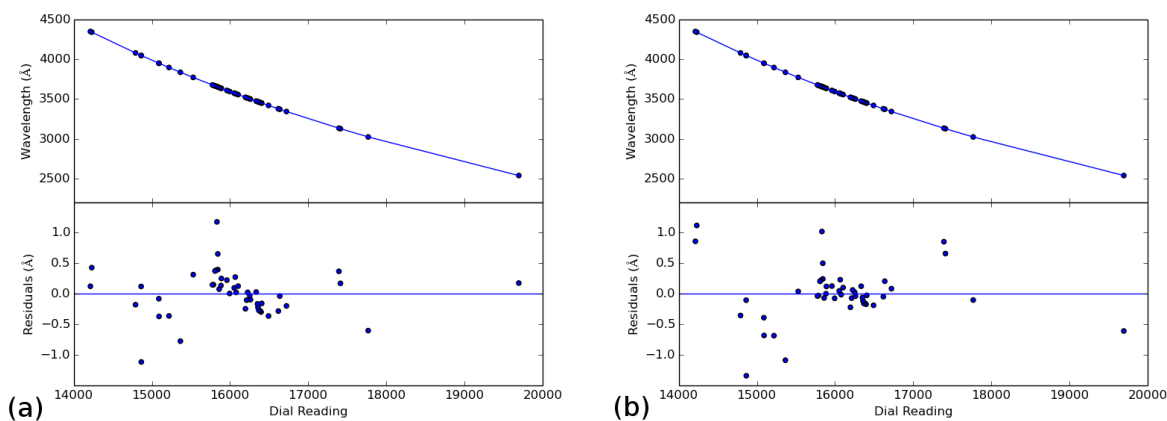


Figure 64: Example wavelength calibration of the dial indicator on the SPEX 1401 showing fits to (a) Equation (D.3) or (b) Equation (D.4). The corresponding residuals are shown in the lower plots.

A comparison of the two fits to actual calibration data is shown in Figure 64 for the SPEX 1401 equipped with two 1800 lines/mm ruled gratings used in first order. It is seen that the two methods are practically indistinguishable over the full range of calibration, with both yielding residuals falling mostly within the range $\pm 1 \text{ \AA}$. The calibration points were taken over the course of several days for three different types of calibration lamps: Hg, Ne, and Ar. The tabulated wavelengths of the spectral lines from these sources are likely known to high enough accuracy that the residuals appearing in Figure 64 result from measurement errors in the dial readings.

Backlash in the gear mechanism is one possible source of such an error. In order to counteract this problem, measurements are only recorded while scanning the gratings towards long wavelengths (forward direction). In the event that the monochromator needs to be set to a shorter wavelength λ_0 for a new measurement sequence, one scans the gratings in the reverse direction, overshooting λ_0 by a certain amount (the SPEX 1401 manual recommends a 200 cm^{-1} interval on the dial indicator), and finally scanning ahead in the forward direction to λ_0 . This procedure has been put into practice for all measurements taken in

this work for the SPEX 1401 (as well as photoluminescence measurements on the Fast-Fastie spectrometer), although the extent to which it is able to eliminate the effects of backlash has not been systematically studied.

A second possible source of measurement and calibration error may be ambient temperature fluctuations causing various components in the monochromator to mechanically drift and slip. Very little is known about the magnitude of these effects for the particular system used in this work, although it is a known issue that has been studied in other drive systems [107]. In this work it has been observed that the wavelength separation between pairs of closely spaced spectral features in a single measurement sequence is often more precisely measured than the absolute wavelengths of those features. Since these features could be measured together within a short span of time and without having to reverse the scanning direction, it's likely they would not be subject to errors due to temperature drift and backlash. Since the primary focus of this work has been on wavelength separations rather than absolute wavelengths, no attempt has been made to improve upon the measurement errors apparent in Figure 64.

BIBLIOGRAPHY

- [1] H. J. Round. A note on carborundum. *Electrical World*, 9:309, 1907.
- [2] O. V. Losev. CII. Luminous carborundum detector and detection effect and oscillations with crystals. *The London, Edinburgh, and Dublin Philosophical Magazine and Journal of Science*, 6(39):1024–1044, 1928. [*Telegrafiya i Telefoniya bez Provodov* 5(44):485–494, 1927].
- [3] J. A. Lely. Preparation of single crystals of silicon carbide and the effect of the kind and amount of impurities on the lattice. *Berichte der Deutschen Keramischen Gesellschaft*, 32(8):229–236, 1955.
- [4] R. G. Humphreys, D. Bimberg, and W. J. Choyke. Wavelength modulated absorption in SiC. *Solid State Communications*, 39(1):163–167, 1981.
- [5] S. G. Sridhara, S. Bai, O. Shigiltchhoff, R. P. Devaty, and W. J. Choyke. Differential absorption measurement of valence band splittings in 4H SiC. In *Materials Science Forum*, volume 338–342, pages 567–570. Trans Tech Publications, 2000.
- [6] W. J. Choyke, R. P. Devaty, and S. G. Sridhara. A survey of conduction and valence band edges in SiC. *Physica Scripta*, T79:9–15, 1999.
- [7] R. P. Devaty, W. J. Choyke, S. G. Sridhara, L. L. Clemen, D. G. Nizhner, D. J. Larkin, T. Troffer, G. Pensl, T. Kimoto, and H. S. Kong. Optical properties of silicon carbide: Some recent developments. In *Materials Science Forum*, volume 264–268, pages 455–460. Trans Tech Publications, 1998.
- [8] A. P. Krokhmal'. Fine structure of the long-wavelength edge of exciton-phonon absorption and hyperbolic excitons in silicon carbide of 6H polytype. *Semiconductors*, 37(3):249–255, 2003.
- [9] I. S. Gorban', V. A. Gubanov, V. G. Lysenko, A. A. Pletyushkin, and V. B. Timofeev. Fine structure of S states of indirect excitons in cubic silicon carbide. *Soviet Physics Solid State*, 26(8):1385–1388, 1984.
- [10] R. P. Devaty, S. Bai, W. J. Choyke, D. Hobgood, D. J. Larkin, et al. Valence band splittings of 15R SiC measured using wavelength modulated absorption spectroscopy.

- In *Materials Science Forum*, volume 353–356, pages 357–360. Trans Tech Publications, 2001.
- [11] P. Käckell, B. Wenzien, and F. Bechstedt. Electronic properties of cubic and hexagonal SiC polytypes from ab initio calculations. *Physical Review B*, 50(15):10761–10768, 1994.
 - [12] W. R. L. Lambrecht, S. Limpijumnong, S. N. Rashkeev, and B. Segall. Electronic band structure of SiC polytypes: A discussion of theory and experiment. *Physica Status Solidi (b)*, 202(1):5–33, 1997.
 - [13] C. Persson and U. Lindefelt. Detailed band structure for 3C-, 2H-, 4H-, 6H-SiC, and si around the fundamental band gap. *Physical Review B*, 54(15):10257–10260, 1996.
 - [14] C. Persson and U. Lindefelt. Relativistic band structure calculation of cubic and hexagonal SiC polytypes. *Journal of Applied Physics*, 82(11):5496–5508, 1997.
 - [15] G. Wellenhofer and U. Rössler. Global band structure and near-band-edge states. *Physica Status Solidi (b)*, 202(1):107–123, 1997.
 - [16] S. G. Sridhara, T. J. Eperjesi, R. P. Devaty, and W. J. Choyke. Penetration depths in the ultraviolet for 4H, 6H and 3C silicon carbide at seven common laser pumping wavelengths. *Materials Science and Engineering*, B61–62:229–233, 1999.
 - [17] H. -J. Im, B. Kaczer, J. P. Pelz, S. Limpijumnong, W. R. L. Lambrecht, and W. J. Choyke. Nanometer-scale investigation of metal-SiC interfaces using ballistic electron emission microscopy. *Journal of Electronic Materials*, 27(4):345–352, 1998.
 - [18] B. Kaczer, H. -J. Im, J. P. Pelz, J. Chen, and W. J. Choyke. Direct observation of conduction-band structure of 4H-and 6H-SiC using ballistic electron emission microscopy. *Physical Review B*, 57(7):4027–4032, 1998.
 - [19] R. J. Elliott. Intensity of optical absorption by excitons. *Physical Review*, 108(6):1384–1389, 1957.
 - [20] C. Persson and U. Lindefelt. Density of states in hexagonal SiC polytypes. *Journal of Applied Physics*, 83(1):266–269, 1998.
 - [21] G. Dresselhaus. Effective mass approximation for excitons. *Journal of Physics and Chemistry of Solids*, 1:14–22, 1956.
 - [22] J. M. Luttinger and W. Kohn. Motion of electrons and holes in perturbed periodic fields. *Physical Review*, 97(4):869–883, 1955.
 - [23] W. Kohn. Theory of bloch electrons in a magnetic field: The effective hamiltonian. *Physical Review*, 115(6):1460–1478, 1959.

- [24] C. H. Kittel and A. H. Mitchell. Theory of donor and acceptor states in silicon and germanium. *Physical Review*, 96(6):1488–1493, 1954.
- [25] G. H. Wannier. The structure of electronic excitation levels in insulating crystals. *Physical Review*, 52(3):191–197, 1937.
- [26] L. Patrick and W. J. Choyke. Static dielectric constant of SiC. *Physical Review B*, 2(6):2255–2256, 1970.
- [27] W. J. Choyke and L. Patrick. Exciton recombination radiation and phonon spectrum of 6H SiC. *Physical Review*, 127(6):1868–1877, 1962.
- [28] W. J. Choyke, R. P. Devaty, L. L. Clemen, M. F. MacMillan, M. Yoganathan, and G. Pensl. Optical properties and characterization of SiC and III-V nitrides. *Institute of Physics Conference Series*, 142:257–262, 1996.
- [29] G. E. Pikus. A new method of calculating the energy spectrum of carriers in semiconductors. I. Neglecting spin-orbit interaction. *Soviet Physics JETP*, 14(4):898–907, 1962.
- [30] G. E. Pikus. A new method of calculating the energy spectrum of carriers in semiconductors. II. Account of spin-orbit interaction. *Soviet Physics JETP*, 14(5):1075–1085, 1962.
- [31] G. L. Bir and G. E. Pikus. *Symmetry and strain-induced effects in semiconductors*, chapter 15, pages 187–202. Wiley New York, 1974.
- [32] E. I. Rashba. Symmetry of energy bands in crystals of wurtzite type. I. Symmetry of bands disregarding spin-orbit interaction. *Soviet Physics Solid State*, 1(3):368–380, 1959.
- [33] E. I. Rashba and V. Sheka. Symmetry of energy bands in crystals of wurtzite type II. Symmetry of bands with spin-orbit interaction included. *Fizika Tverdogo Tela*, 2:62–76, 1959. [English translation appears as supplementary material to G. Bihlmayer, O. Rader, and R. Winkler, Focus on the Rashba Effect, *New Journal of Physics* 17:050202, 2015].
- [34] N. T. Son, W. M. Chen, O. Kordina, A. O. Konstantinov, B. Monemar, E. Janzén, D. M. Hofman, D. Volm, M. Drechsler, and B. K. Meyer. Electron effective masses in 4H SiC. *Applied Physics Letters*, 66(9):1074–1076, 1995.
- [35] D. Volm, B. K. Meyer, D. M. Hofmann, W. M. Chen, N. T. Son, C. Persson, U. Lindelfelt, O. Kordina, E. Sörman, A. O. Konstantinov, B. Monemar, and E. Janzén. Determination of the electron effective-mass tensor in 4H SiC. *Physical Review B*, 53(23):15409–15412, 1996.
- [36] N. T. Son, P. N. Hai, W. M. Chen, C. Hallin, B. Monemar, and E. Janzén. Hole effective masses in 4H SiC. *Physical Review B*, 61(16):R10544, 2000.

- [37] A. Taylor and D. S. Laidler. The formation and crystal structure of silicon carbide. *British Journal of Applied Physics*, 1(7):174–181, 1950.
- [38] B. Batz. Thermal and wavelength modulation spectroscopy. In R. K. Willardson and A. C. Beer, editors, *Semiconductors and Semimetals*, volume 9, pages 326–333. Academic, New York, 1972.
- [39] K. L. Shaklee and R. E. Nahory. Valley-orbit splitting of free excitons? The absorption edge of Si. *Physical Review Letters*, 24(17):942–945, 1970.
- [40] T. Nishino, M. Takeda, and Y. Hamakawa. Direct observation of split-off exciton and phonon structures in absorption spectrum of silicon. *Solid State Communications*, 14(7):627–630, 1974.
- [41] T. Nishino, M. Takeda, and Y. Hamakawa. Indirect exciton absorption in germanium. *Journal of the Physical Society of Japan*, 37(4):1016–1023, 1974.
- [42] J. -C. Merle, M. Capizzi, P. Fiorini, and A. Fropa. Uniaxially stressed silicon: Fine structure of the exciton and deformation potentials. *Physical Review B*, 17(12):4821–4834, 1978.
- [43] P. J. Dean, G. Kaminsky, and R. B. Zetterstrom. Intrinsic optical absorption of gallium phosphide between 2.33 and 3.12 eV. *Journal of Applied Physics*, 38(9):3551–3556, 1967.
- [44] G. F. Koster, J. O. Dimmock, R. G. Wheeler, and H. Statz. *Properties of the 32 Point Groups*. MIT Press, Cambridge, 1963.
- [45] Y. Hazama, N. Naka, and H. Stolz. Mass-anisotropy splitting of indirect excitons in diamond. *Physical Review B*, 90(4):045209, 2014.
- [46] W. Heitler. *The quantum theory of radiation*, chapter 5. Clarendon Press, Oxford, third edition, 1954.
- [47] S. Zollner, S. Gopalan, and M. Cardona. Microscopic theory of intervalley scattering in GaAs: k dependence of deformation potentials and scattering rates. *Journal of Applied Physics*, 68(4):1682–1693, 1990.
- [48] N. W. Ashcroft and N. D. Mermin. *Solid State Physics*, pages 780–783. Brooks Cole, Belmont, CA, 1976.
- [49] I. G. Ivanov, U. Lindefelt, A. Henry, O. Kordina, C. Hallin, M. Aroyo, T. Egilsson, and E. Janzén. Phonon replicas at the M point in 4H-SiC: A theoretical and experimental study. *Physical Review B*, 58(20):13634–13647, 1998.
- [50] R. S. Knox. Theory of excitons. volume 3, pages 37–59. Academic, New York, 1963.

- [51] T. P. McLean and R. Loudon. Exciton energy levels in germanium and silicon. *Journal of Physics and Chemistry of Solids*, 13(1-2):1–9, 1960.
- [52] R. J. Elliott. Spin-orbit coupling in band theory—character tables for some double space groups. *Physical Review*, 96(2):280–287, 1954.
- [53] E. O. Kane. The influence of exchange on the effective mass formalism. *Journal of Physics and Chemistry of Solids*, 6(2):236–241, 1958.
- [54] E. O. Kane. The semi-empirical approach to band structure. *Journal of Physics and Chemistry of Solids*, 8:38–44, 1959.
- [55] D. Labrie, M. L. W. Thewalt, I. J. Booth, and G. Kirczenow. Detailed ground- and excited-state spectroscopy of indirect free excitons. *Physical Review Letters*, 61(16):1882–1884, 1988.
- [56] G. L. Zhao and D. Bagayoko. Electronic structure and charge transfer in 3C- and 4H-SiC. *New Journal of Physics*, 2(1):16, 2000.
- [57] H. N. Russell and F. A. Saunders. New regularities in the spectra of the alkaline earths. *Astrophysical Journal*, 61:38, 1925.
- [58] E. U. Condon and G. H. Shortley. *The theory of atomic spectra*, chapter 7. Cambridge University Press, 1951.
- [59] Neil W. Ashcroft and N. D. Mermin. *Solid State Physics*, pages 143–145. Brooks Cole, Belmont, CA, 1976.
- [60] G. Davies. Inhomogeneous broadening of edge recombination radiation. *Journal of Physics and Chemistry of Solids*, 31(4):883 – 886, 1970.
- [61] I. G. Ivanov, C. Hallin, A. Henry, O. Kordina, and E. Janzén. Nitrogen doping concentration as determined by photoluminescence in 4H- and 6H-SiC. *Journal of Applied Physics*, 80(6):3504–3508, 1996.
- [62] L. Patrick. Inequivalent sites and multiple donor and acceptor levels in SiC polytypes. *Physical Review*, 127(6):1878, 1962.
- [63] L. Patrick, W. J. Choyke, and D. R. Hamilton. Luminescence of 4H SiC, and location of conduction-band minima in SiC polytypes. *Physical Review*, 137(5A):A1515–A1520, 1965.
- [64] J. R. Haynes. Experimental proof of the existence of a new electronic complex in silicon. *Physical Review Letters*, 4(7):361–363, 1960.
- [65] M. Ikeda and H. Matsunami. Free exciton luminescence in 3C, 4H, 6H, and 15R SiC. *Physica Status Solidi (a)*, 58(2):657–663, 1980.

- [66] M. L. W. Thewalt, G. Kirczenow, R. R. Parsons, and R. Barrie. Phonon broadening of bound exciton luminescence in silicon. *Canadian Journal of Physics*, 54(16):1728–1740, 1976.
- [67] M. Cardona. Modulation Spectroscopy. In *Solid State Physics, Supplement 11*, pages 105–115. Academic, New York, 1969.
- [68] K. L. Shaklee and J. E. Rowe. Wavelength modulation spectrometer for studying the optical properties of solids. *Applied Optics*, 9(3):627–632, 1970.
- [69] F. A. Jenkins and H. E. White. *Fundamentals of Optics*, page 19. McGraw-Hill, New York, third edition, 1957.
- [70] F. G. Brickwedde et al. The 1958 He4 scale of temperatures. *Journal of Research of the National Bureau of Standards A. Physics and Chemistry*, 64A, 1960.
- [71] G. Bonfiglioli, P. Brovotto, G. Busca, S. Leviardi, G. Palmieri, and E. Wanke. Self modulating, derivative optical spectroscopy. Part II: Experimental. *Applied Optics*, 6(3):447–455, 1967.
- [72] P. T. B. Shaffer. Refractive index, dispersion, and birefringence of silicon carbide polytypes. *Applied Optics*, 10(5):1034–1036, 1971.
- [73] J. L. Amorós, M. J. Buerger, and M. Canut de Amorós. *The Laue Method*. Academic, New York, 1975.
- [74] M. Yoganathan, W. Suttrop, R. P. Devaty, and W. J. Choyke. Identification of $\{2\bar{1}\bar{1}0\}$ and $\{10\bar{1}0\}$ Laue patterns of hexagonal and rhombohedral silicon carbide polytypes. *Journal of Applied Crystallography*, 27:497–503, 1994.
- [75] M. Cardona. Modulation Spectroscopy. In *Solid State Physics, Supplement 11*, pages 52–58. Academic, New York, 1969.
- [76] SciPy Project Page. <https://scipy.org>.
- [77] M. A. Branch, T. F. Coleman, and Y. Li. A subspace, interior, and conjugate gradient method for large-scale bound-constrained minimization problems. *SIAM Journal on Scientific Computing*, 21(1):1–23, 1999.
- [78] W. H. Press, S. A. Teukolsky, W. T. Vetterling, and B. P. Flannery. *Numerical Recipes in C*, pages 689–698. Cambridge University Press, Cambridge, second edition, 1992.
- [79] J. Serrano, J. Stremper, M. Cardona, M. Schwoerer-Böhning, H. Requardt, M. Lorenzen, B. Stojetz, P. Pavone, and W. J. Choyke. Lattice dynamics of 4H-SiC by inelastic x-ray scattering. In *Silicon Carbide and Related Materials - 2002*, volume 433–436 of *Materials Science Forum*, pages 257–260. Trans Tech Publications, 2003.

- [80] D. Strauch, B. Dorner, A. Ivanov, M. Krisch, J. Serrano, A. Bosak, W. J. Choyke, B. Stojetz, and M. Malorny. Phonons in SiC from INS, IXS, and ab-initio calculations. In *Materials Science Forum*, volume 527–529, pages 689–694. Trans Tech Publications, 2006.
- [81] M. Hofmann, A. Zywietz, K. Karch, and F. Bechstedt. Lattice dynamics of SiC polytypes within the bond-charge model. *Physical Review B*, 50(18):13401–13411, 1994.
- [82] N. H. Protik, A. Katre, L. Lindsay, J. Carrete, N. Mingo, and D. Broido. Phonon thermal transport in 2H, 4H and 6H silicon carbide from first principles. *Materials Today Physics*, 1:31–38, 2017.
- [83] I. Balslev. Influence of uniaxial stress on the indirect absorption edge in silicon and germanium. *Physical Review*, 143(2):636–647, 1966.
- [84] E. Adler and E. Erlbach. Polarization dependence of the indirect piezoabsorption coefficient in Ge and Si. *Physical Review Letters*, 16(3):87–89, 1966.
- [85] S. Zwerdling, B. Lax, L. M. Roth, and K. J. Button. Exciton and magneto-absorption of the direct and indirect transitions in germanium. *Physical Review*, 114(1):80–89, 1959.
- [86] K. J. Button, L. M. Roth, W. H. Kleiner, S. Zwerdling, and B. Lax. Fine structure in the zeeman effect of excitons in germanium. *Physical Review Letters*, 2(4):161–162, 1959.
- [87] J. Donecker and J. Kluge. Excitonic absorption in silicon in the presence of low magnetic fields. *Physica Status Solidi (b)*, 137(2):591–595, 1986.
- [88] A. Frova, G. A. Thomas, R. E. Miller, and E. O. Kane. Mass reversal effect in the split indirect exciton of ge. *Physical Review Letters*, 34(25):1572–1575, 1975.
- [89] M. Altarelli and N. O. Lipari. Indirect exciton dispersion and line shape in Ge. *Physical Review Letters*, 36(11):619–622, 1976.
- [90] G. Lehmann and M. Taut. On the numerical calculation of the density of states and related properties. *Physica Status Solidi (b)*, 54(2):469–477, 1972.
- [91] M. V. Hobden. Direct optical transitions from the split-off valence band to the conduction band in germanium. *Journal of Physics and Chemistry of Solids*, 23(6):821–822, 1962.
- [92] T. P. McLean and E. G. S. Paige. Optical absorption edge broadening in germanium. *Journal of Physics and Chemistry of Solids*, 23(6):822–825, 1962.
- [93] D. G. Thomas. The exciton spectrum of zinc oxide. *Journal of Physics and Chemistry of Solids*, 15(1–2):86–96, 1960.

- [94] D. G. Thomas and J. J. Hopfield. Exciton spectrum of cadmium sulfide. *Physical Review*, 116(3):573–582, 1959.
- [95] R. S. Knox. Theory of excitons. volume 3, pages 13–20. Academic, New York, 1963.
- [96] E. Jahne and E. Gutsche. Valence band structure of wurtzite type crystals. *Physica Status Solidi (b)*, 21(1):57–68, 1967.
- [97] G. B. Dubrovskii and V. I. Sankin. Exciton electroabsorption in 6H-SiC. *Soviet Physics Solid State*, 14:1024, 1972.
- [98] R. G. Humphreys, D. Bimberg, and W. J. Choyke. Wavelength modulated absorption in SiC polytypes. In *Proceedings of the 15th International Conference of the Physics of Semiconductors, Kyoto*, 1980.
- [99] A. Doi and A. Koide. An efficient method of triangulating equi-valued surfaces by using tetrahedral cells. *IEICE Transactions on Information and Systems*, E74–D(1):214–224, 1991.
- [100] Eigen C++ Libraries. <https://eigen.tuxfamily.org/dox/GettingStarted.html>.
- [101] Thorlabs Product Catalog. <https://www.thorlabs.com>.
- [102] R. McCluney. *Introduction to Radiometry and Photometry*, chapter 1, pages 7–20. Artech House, Boston, 1994.
- [103] J. F. James and R. S. Sternberg. *The Design of Optical Spectrometers*, chapter 11, pages 191–193. Chapman and Hall, London, 1969.
- [104] B. T. Cooper, G. D. Chumanov, and T. M. Cotton. Modification and calibration of a cosecant-drive spectrometer for use in the UV. *Applied Spectroscopy*, 51(9):1431–1434, 1997.
- [105] D. E. Gray. *American Institute of Physics Handbook*, chapter 7, pages 42–122. McGraw-Hill, 1957.
- [106] NIST Atomic Spectra Database Lines Form. https://physics.nist.gov/PhysRefData/ASD/lines_form.html.
- [107] D. L. Dimock. Temperature compensation of sine-drive monochromators. *Journal of the Optical Society of America*, 50(8):819–820, 1960.